


Winter 12-14-2018

# The Investigation of the Chlorine Initiated Oxidation of 2-Phenylethanol and Stability of Superalkali Lithium Substituted Silyls.

Adam Otten  
amotten@usfca.edu

Follow this and additional works at: <https://repository.usfca.edu/thes>

 Part of the [Analytical Chemistry Commons](#), [Environmental Chemistry Commons](#), and the [Physical Chemistry Commons](#)

---

## Recommended Citation

Otten, Adam, "The Investigation of the Chlorine Initiated Oxidation of 2-Phenylethanol and Stability of Superalkali Lithium Substituted Silyls." (2018). *Master's Theses*. 1159.  
<https://repository.usfca.edu/thes/1159>

This Thesis is brought to you for free and open access by the Theses, Dissertations, Capstones and Projects at USF Scholarship: a digital repository @ Gleeson Library | Geschke Center. It has been accepted for inclusion in Master's Theses by an authorized administrator of USF Scholarship: a digital repository @ Gleeson Library | Geschke Center. For more information, please contact [repository@usfca.edu](mailto:repository@usfca.edu).

**The Investigation of the Chlorine Initiated Oxidation of 2-Phenylethanol and  
Stability of Superalkali Lithium Substituted Silyls.**

A Thesis presented to the Faculty of the  
Department of Chemistry at the  
University of San Francisco  
in partial fulfillment of the requirements for the  
Degree of Master of Science in Chemistry

Written by  
Adam Otten  
Bachelor of Science in Chemistry  
Drew University  
12/7/18

# **The Investigation of the Chlorine Initiated Oxidation of 2-Phenylethanol and Stability of Superalkali Lithium Substituted Silyls.**

Thesis written by Adam Otten

This thesis is written under the guidance of the Faculty Advisory Committee, and approved by all its members, has been accepted in partial fulfillment of the requirements for the degree of

**Master of Science in Chemistry  
at  
the University of San Francisco**

## Thesis Committee

Giovanni Meloni Ph.D.

Research Advisor

Janet Yang Ph.D.

Assistant Professor

William Melaugh Ph.D.

Professor

Marcelo Camperi Ph.D.

Dean, College of Arts and Sciences

## **Table of Contents**

### **Abstract**

### **Chapter 1 – Introduction**

1.1 Atmospheric Pollution and the Need for Alternative Energy	1
1.2 Combustion and Engine Technology	2
1.3 Biofuels and Alternative Energy Sources	4
1.4 References	6

### **Chapter 2 – Experimental**

2.1 The Advanced Light Source(ALS)	8
2.2 Components of the ALS	8
2.2.1 The Linear Accelerator (linac)	9
2.2.2 The Booster Synchrotron	10
2.2.3 The Storage Ring and Undulators	10
2.2.4 The ALS beamline	11
2.3 The Experimental Apparatus	13
2.3.1 Excimer Laser	13
2.3.2 Vacuum System	14
2.3.3 Time of Flight Mass Spectrometer (TOF-MS)	17
2.3.4 Microchannel Plate (MCP) detector	18
2.3.5 Data Analysis	20

2.4 References	22
<b>Chapter 3 – Theory</b>	
3.1 Photoionization	23
3.2 Franck-Condon Principle	24
3.3 Photoionization Spectra, Photoionization Cross Sections	27
3.4 Electronic Structure Calculations	30
3.5 References	32
<b>Chapter 4 - Investigation of Oxidation Reaction Products of 2-Phenylethanol Using Synchrotron Photoionization</b>	
4.1 Introduction	35
4.2 Experimental	37
4.3 Results and Discussion	41
4.4 Proposed Mechanism	48
4.5 Branching Fractions	52
4.6 Conclusions	53
4.7 References	55
4.8 Supporting Material	58
<b>Chapter 5 - Stability of Lithium Substituted Silyls Superalkali Species</b>	
5.1 Introduction	79
5.2 Methods	80

5.3 Results and Discussion	81
5.4 Conclusions	94
5.5 References	96

**Acknowledgements:**

I would like to thank my research advisor Dr Giovanni Meloni for all of his teachings, guidance, and support. I am grateful to Dr Meloni for fostering my talents as a scientist, and helping me grow as a physical chemist and published author. I am thankful for the opportunity I was given to study with Dr Chia Wang at National Sun Yat-Sen University in Kaosiung Taiwan, and learn about aqueous nano-aerosols. I could not have finished this masters program without the help of my research group here at USF, so thank you to: Ben Park, Erica Carrasco, Yasmin Fathi, Chelsea Price, and Matthew Winfough.

Thank you to all of the amazing faculty and staff at USF who have helped me throughout my journey here. Thank you to Dr William Melaugh and Dr Janet Yang for their input on my thesis, and for always giving me encouragement and support. Thank you Dr William Karney for always helping me better understand my computational research. Thank you to Dr Lawrence Margerum and Dr Ryan West for helping me hone my skills as a TA and tutor. Also a special thank you to Deidre Shymanski for always being there to help with everything behind the scenes.

Lastly, thank you to my friends and family for all of their love and support. Love you all.

**Abstract:**

This thesis investigates the combustion potential of 2-phenylethanol and the superalkali properties of small lithium substituted silicon compounds. All combustion experiments were performed at the Advanced Light Source of Lawrence Berkeley National Laboratory at the Chemical Dynamics Beamline 9.0.2. The chlorine initiated oxidation of 2PE was investigated at 298 and 550 K using a multiplex photoionization mass spectrometer, coupled with the tunable vacuum ultraviolet radiation. Reaction products were identified using kinetic time traces and photoionization spectra.

Additionally, the stability of small superalkali silicon-lithium compounds has also been investigated. All structures and energetics were calculated using the CBS-QB3 composite method.

The first chapter of this thesis discusses atmospheric pollution, engine technology, biofuels and other alternative energy sources. The ALS, the experimental apparatus and their components are explained throughout Chapter 2. Chapter 3 explains the theory behind the computational methodology, as well as how to analyze the results obtained from the experimental apparatus. Chapter 4 evaluates the chlorine initiated oxidation of 2-phenylethanol. Chapter 5 investigates the superalkali properties of small silicon-lithium compounds.



## **Chapter 1 - Introduction:**

### **1.1 Atmospheric Pollution and the Need for Alternative Energy:**

Over the last century, fossil fuels have dominated as the world's energy market as our leading source of power. Every year, several billion tons of pollutants are emitted into the atmosphere through agriculture, fossil fuel combustion for power and transportation and the burning of forests.<sup>1</sup> The air pollution emitted from these anthropogenic sources are found to contribute to past climate change, and weather modification.<sup>2</sup> The major components of air pollution generated from these sources are: NO<sub>2</sub>, SO<sub>2</sub>, ozone, and particulate matter (PM).<sup>3</sup> Many studies have linked the products from fossil fuel combustion and pollutants from other anthropogenic sources to numerous respiratory and cardiovascular conditions, as well as an increased susceptibility to respiratory infections and cancers.<sup>4-6</sup> These adverse health effects are a major problem in China, Taiwan, and many other Asian countries where they have an excess of air pollution generated from industrial sources. Countries like Taiwan are working in conjunction with the EPA and other government agencies to help combat the severe atmospheric damage, but many are falling short due to lack of funding.

In the 21<sup>st</sup> century, the US is in a major energy crisis due to depletion of petroleum sources, which is driving up the cost of oil.<sup>7</sup> In the past decade, we have seen this world shift from fossil fuels to more renewable and sustainable sources. The company Tesla<sup>8</sup> has revolutionized the sustainable energy option for power and transportation with their affordable ion exchange batteries and solar panels. The company Bloom Energy has created a sustainable solid oxide fuel cell that runs on natural gas producing only CO<sub>2</sub> and water<sup>8</sup>. Biofuels offer a promising long-term option because of their fuel-source regenerability and reduced carbon

emissions.<sup>9</sup> While these biofuels appear to be a viable alternative over fossil fuel, their combustion properties are still unknown. The Meloni group is investigating the oxidation reactions of potential biofuels to test their reactivity and possible pollutants. The Meloni group is also researching “super-atoms,” clusters with unique charge transfer abilities, that could have potentials on ion exchange batteries and solar cells. This work evaluates the combustion potential of 2-phenylethanol and investigates the superalkali properties of small lithium substituted silicon compounds.

## **1.2 Combustion and Engine Technology:**

Fossil fuel combustion accounts for over 80 % of the worlds primary energy consumption.<sup>7</sup> Combustion is defined as the exothermic chemical reaction between fuel and an oxidant that produces energy in the form of light and heat.<sup>10</sup> A simple reaction for combustion can be seen in the equation:  $\text{Fuel} + \text{O}_2 \longrightarrow \text{H}_2\text{O} + \text{CO}_2 + \text{heat}$ . Since this process is not 100 % complete, byproducts such as polycyclic aromatic hydrocarbons and other pollutants are formed and released into the atmosphere.<sup>11</sup> This investigation focuses on low temperature (<14000 K) combustion characteristic of auto ignition chemistry. The oxidation of potential biofuels is examined, where the fuel is ignited similarly to how the reaction would occur in a homogeneous charged compression ignition (HCCI) engine. The ignition of these fuels in an HCCI engine is initiated by hydroxyl radicals generated from the decomposition of  $\text{H}_2\text{O}_2$ ,<sup>12</sup> which can be seen in Figure 1.

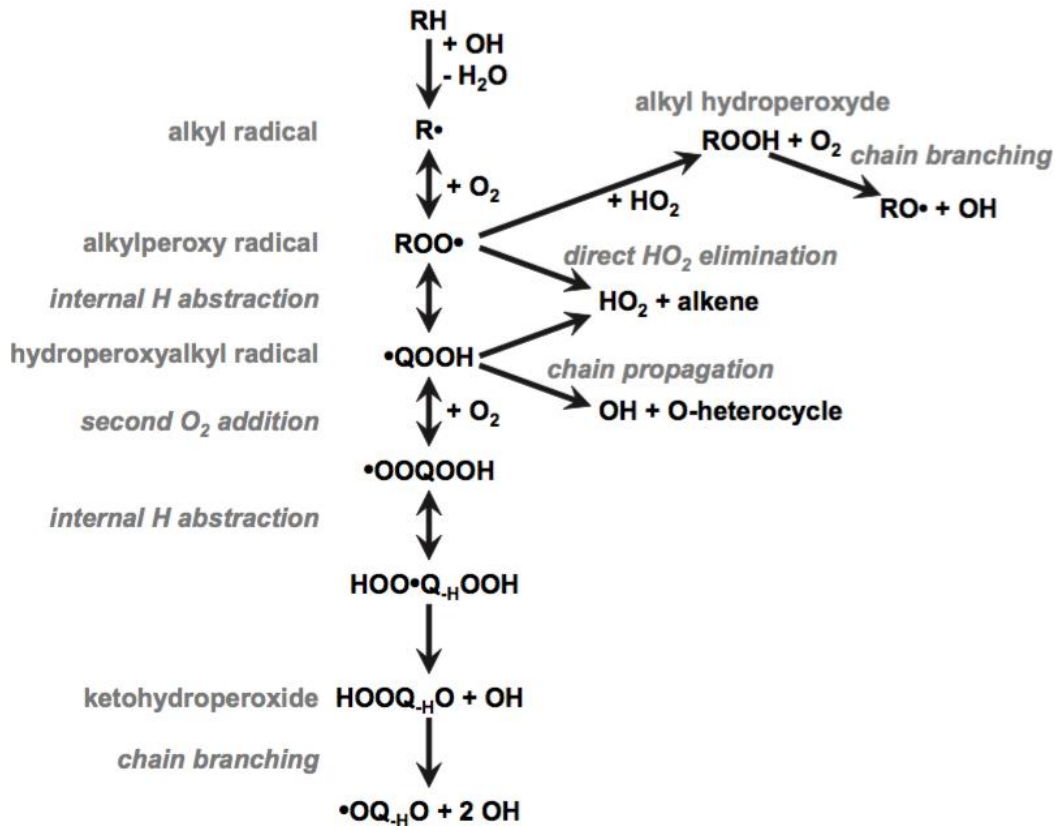


Figure 1. Mechanism for low temperature hydrocarbon oxidation and autoignition chemistry.<sup>13</sup>

This initiation produces the reactive alkyl radical, which is then oxidized to produce the peroxy radical ROO.<sup>14</sup> This radical can either then isomerize to QOOH or react through several different pathways such as chain propagation, chain branching and direct elimination.

The homogeneous charged compression ignition (HCCI) engine is a combination between the compressed ignition and spark ignition engines, and can be run on a wide variety of fuels.<sup>15</sup> The combustion process in an HCCI engine occurs at much lower temperature than that of an SI or CI engine, which greatly reduces particulate matter and NO<sub>x</sub> emissions.<sup>16</sup> The main differences between these three engines are the ignition regions in the combustion chamber where the fuel mixes with air, which can be seen in Figure 2.

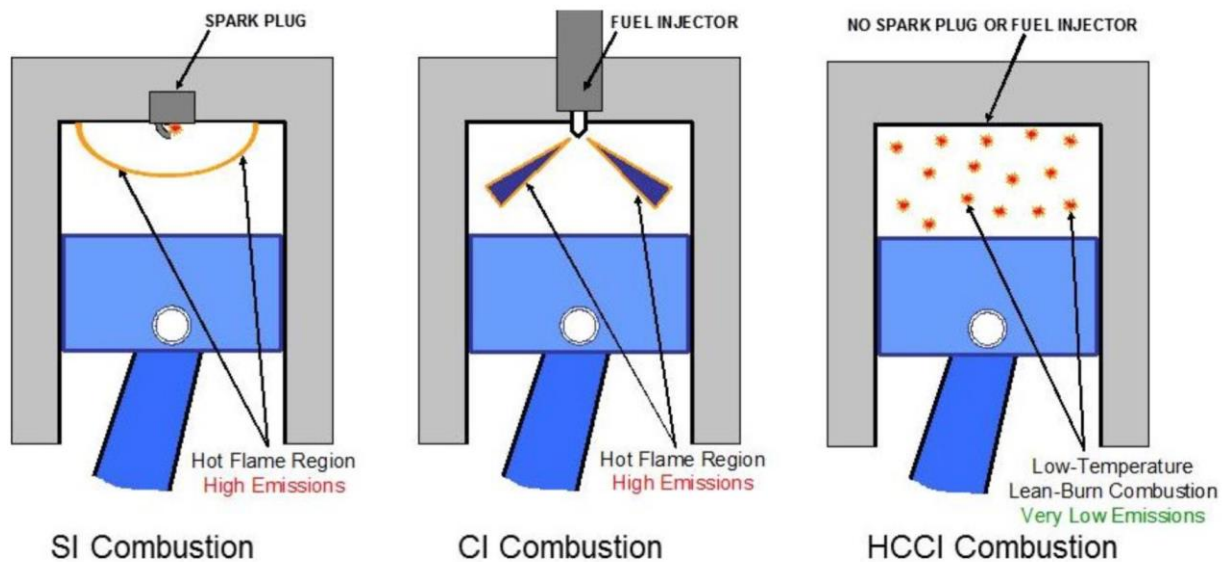


Figure 2. Illustration of the differences between SI, CI, and HCCI engines.<sup>15</sup>

Combustion in the HCCI engine does not rely on the use of a spark plug or direct injection for ignition to occur, and relies on the auto-ignition properties of the fuel-air mixture.<sup>17</sup> High fuel economy can be achieved with the use of lean fuel mixtures, but incomplete combustion can occur if the mixture is too lean, resulting in high CO and hydrocarbon emissions.<sup>15</sup> Consequently, if the fuel is too rich, the increase in pressure will lead to engine damage or high NO<sub>x</sub> emissions from high temperature combustion.

### 1.3 Biofuels and Alternative Energy Sources:

Limited resources of fossil fuels and the growing global demand for energy have increased the world's investment in finding alternative fuels, which would be both efficient and environmentally friendly.<sup>18-19</sup> One of such alternatives are biofuels, which are defined as liquid or gas fuels that are predominately produced by biomass.<sup>9</sup> Biofuels are an attractive alternative over fossil fuels since they are renewable and easily produced from common biomass sources,

and are biodegradable. Biofuels are also an environmentally friendly solution, since their combustion can recycle carbon dioxide through photosynthetic pathways.<sup>7</sup> A variety of liquid and gaseous fuels such as ethanol, methanol, biodiesel, hydrogen and methane can be produced from biomass resources.<sup>20</sup> Liquid biofuels such as bioethanol can be produced from any organic matter containing sugars or starches like wheat, barley, corn, and sugar.<sup>21</sup> Biodiesel can be produced from any plant based oils such as rapeseed, palm, soybean, sunflower, and also used vegetable oils discarded from restaurants. Biofuel production poses a challenge since generation of these fuels is very costly due to the high energy requirements for growing crops and their conversion to biofuels. Corn based biofuels would also increase the prices of meat and dairy, since over 50% of the corn produced in the US is used for livestock feed.<sup>19</sup>

A renewable and cost-effective option over biodiesel or bioethanol for biofuel production is using lignocellulosic biomass in the form of plant material like grass, wood, or crop residue.<sup>22</sup> The production of lignocellulosic biofuels involves the deconstruction of cell wall polymers cellulose, hemicellulose, and lignin into sugars, then conversion of those sugars into biofuels.<sup>23</sup> Lignocellulosic biomass offers a viable solution for the production of costly biofuels such as ethanol, and could be used in the generation of new biofuels.<sup>24</sup>

Since the combustion of fossil fuels and biofuels are known to produce harmful byproducts that contribute to atmospheric pollution, other alternative energy sources are currently under investigation. With the population increasing and a growing need for alternative fuel sources, hydrogen energy has become a possible solution because of its planetary abundance, its ability to burn clean, and its high energy density per unit mass<sup>25</sup>. Recent studies have focused on metal hydrides as hydrogen storage carriers since they rely on stronger chemical interactions, resulting in materials that store hydrogen at higher temperatures<sup>26</sup>. Superalkali metal hydrides

and electrolytes have also gained much attention as potential hydrogen storage compounds due to their light weight and high energy density<sup>27</sup>. Due to their low ionization energies, these species could have potential applications for electrochemical storage as in lithium ion batteries<sup>28</sup>.

#### 1.4 References:

1. Ramanathan, V.; Feng, Y., Air pollution, greenhouse gases and climate change: Global and regional perspectives. *Atmos. Environ.* **2008**, *43* (1), 37-50.
2. Hoffert, M. I.; Caldeira, K.; Benford, G.; Criswell, D. R.; Green, C.; Herzog, H.; Jain, A. K.; Kheshgi, H. S.; Lackner, K. S.; Lewis, J. S.; Lightfoot, H. D.; Manheimer, W.; Mankins, J. C.; Mauer, M. E.; Perkins, L. J.; Schlesinger, M. E.; Volk, T.; Wigley, T. M. L., Advanced Technology Paths to Global Climate Stability: Energy for a Greenhouse Planet. *Science (Washington, DC, U. S.)* **2002**, *298* (5595), 981-987.
3. D'Amato, G.; Cecchi, L.; D'Amato, M.; Liccardi, G., Urban air pollution and climate change as environmental risk factors of respiratory allergy: an update. *J Investig Allergol Clin Immunol* **2010**, *20* (2), 95-102; quiz following 102.
4. Kan, H.; Chen, R.; Tong, S., Ambient air pollution, climate change, and population health in China. *Environ. Int.* **2012**, *42*, 10-19.
5. Ackermann-Liebrich, U.; Leuenberger, P.; Schwartz, J.; Schindler, C.; Monn, C.; Bolognini, G.; Bongard, J. P.; Brandli, O.; Domenighetti, G.; Elsasser, S.; Grize, L.; Karrer, W.; Keller, R.; Keller-Wossidlo, H.; Kunzli, N.; Martin, B. W.; Medici, T. C.; Perruchoud, A. P.; Schoni, M. H.; Tschopp, J. M.; Villiger, B.; Wuthrich, B.; Zellweger, J. P.; Zemp, E., Lung function and long term exposure to air pollutants in Switzerland. Study on Air Pollution and Lung Diseases in Adults (SAPALDIA) Team. *Am J Respir Crit Care Med* **1997**, *155* (1), 122-9.
6. Silva, R. A.; West, J. J.; Zhang, Y.; Anenberg, S. C.; Lamarque, J.-F.; Shindell, D. T.; Collins, W. J.; Dalsoren, S.; Faluvegi, G.; Folberth, G.; Horowitz, L. W.; Nagashima, T.; Naik, V.; Rumbold, S.; Skeie, R.; Sudo, K.; Takemura, T.; Bergmann, D.; Smith, P. C.; Cionni, I.; Doherty, R. M.; Eyring, V.; Josse, B.; MacKenzie, I. A.; Plummer, D.; Righi, M.; Stevenson, D. S.; Strode, S.; Szopa, S.; Zeng, G., Global premature mortality due to anthropogenic outdoor air pollution and the contribution of past climate change. *Environ. Res. Lett.* **2013**, *8* (3), 034005/1-034005/11.
7. Escobar, J. C.; Lora, E. S.; Venturini, O. J.; Yanez, E. E.; Castillo, E. F.; Almazan, O., Biofuels: Environment, technology and food security. *Renewable Sustainable Energy Rev.* **2009**, *13* (6-7), 1275-1287.
8. <https://www.tesla.com/support/energy/learn/solar-panels/overview>.
9. Kohse-Hoeninghaus, K.; Osswald, P.; Cool, T. A.; Kasper, T.; Hansen, N.; Qi, F.; Westbrook, C. K.; Westmoreland, P. R., Biofuel Combustion Chemistry: from Ethanol to Biodiesel. *Angew. Chem., Int. Ed.* **2010**, *49* (21), 3572-3597.
10. Bartol, W. S. A. F., *Fossil Fuel Combustion: A Source Book*. John, Wiley, and Sons, Inc: New York, 1991.

11. McEnally, C. S.; Pfefferle, L. D.; Atakan, B.; Kohse-Hoeinghaus, K., Aromatic hydrocarbon formation mechanisms in flames: progress towards closing the fuel gap. *Prog. Energy Combust. Sci.* **2006**, *32* (3), 247-294.
12. Yao, M.; Zheng, Z.; Liu, H., Progress and recent trends in homogeneous charge compression ignition (HCCI) engines. *Prog. Energy Combust. Sci.* **2009**, *35* (5), 398-437.
13. Zador, J.; Taatjes, C. A.; Fernandes, R. X., Kinetics of elementary reactions in low-temperature autoignition chemistry. *Prog. Energy Combust. Sci.* **2011**, *37* (4), 371-421.
14. Grynova, G.; Hodgson, J. L.; Coote, M. L., Revising the mechanism of polymer autooxidation. *Org. Biomol. Chem.* **2011**, *9* (2), 480-490.
15. Charalambides, A. G. In *Homogenous Charge Compression Ignition (HCCI) engines*, InTech: 2013; pp 119-148.
16. Gan, S.-Y.; Ng, H.-K.; Pang, K.-M., Homogeneous Charge Compression Ignition (HCCI) combustion: Implementation and effects on pollutants in direct injection diesel engines. *Appl. Energy* **2011**, *88* (3), 559-567.
17. Starck, L.; Lecointe, B.; Forti, L.; Jeuland, N., Impact of fuel characteristics on HCCI combustion: Performances and emissions. *Fuel* **2010**, *89* (10), 3069-3077.
18. Atsumi, S.; Cann, A. F.; Connor, M. R.; Shen, C. R.; Smith, K. M.; Brynildsen, M. P.; Chou, K. J. Y.; Hanai, T.; Liao, J. C., Metabolic engineering of *Escherichia coli* for 1-butanol production. *Metab. Eng.* **2008**, *10* (6), 305-311.
19. Hill, J.; Nelson, E.; Tilman, D.; Polasky, S.; Tiffany, D., Environmental, economic, and energetic costs and benefits of biodiesel and ethanol biofuels. *Proc. Natl. Acad. Sci. U. S. A.* **2006**, *103* (30), 11206-11210.
20. Demirbas, A., Biofuels sources, biofuel policy, biofuel economy and global biofuel projections. *Energy Convers. Manage.* **2008**, *49* (8), 2106-2116.
21. Agarwal, A. K., Biofuels (alcohols and biodiesel) applications as fuels for internal combustion engines. *Progress in Energy and Combustion Science* **2007**, *33* (3), 233-271.
22. Vispute, T. P.; Huber, G. W., Breaking the chemical and engineering barriers to lignocellulosic biofuels. *Int. Sugar J.* **2008**, *110* (1311), 138, 140, 142, 146, 148-149.
23. Rubin, E. M., Genomics of cellulosic biofuels. *Nature (London, U. K.)* **2008**, *454* (7206), 841-845.
24. Sticklen, M. B., Plant genetic engineering for biofuel production: towards affordable cellulosic ethanol. *Nat. Rev. Genet.* **2008**, *9* (6), 433-443.
25. Jena, P., Materials for Hydrogen Storage: Past, Present, and Future. *J. Phys. Chem. Lett.* **2011**, *2* (3), 206-211.
26. Mohtadi, R.; Remhof, A.; Jena, P., Complex metal borohydrides: multifunctional materials for energy storage and conversion. *Journal of physics. Condensed matter : an Institute of Physics journal* **2016**, *28* (35), 353001.
27. Giri, S.; Behera, S.; Jena, P., Superhalogens as building blocks of halogen-free electrolytes in lithium-ion batteries. *Angewandte Chemie* **2014**, *53* (50), 13916-9.
28. Giri, S.; Behera, S.; Jena, P., Superalkalis and superhalogens as building blocks of supersalts. *The journal of physical chemistry. A* **2014**, *118* (3), 638-45.

## **Chapter 2 - Experimental**

### **2.1 The Advanced Light Sources(ALS):**

The ALS is a third generation synchrotron facility, a particle accelerator that generates bright beams of light used for scientific research. Synchrotron radiation is the electromagnetic radiation emitted by electrons moving at relativistic velocities along a curved trajectory<sup>1</sup>. ALS is one of the brightest photoionization sources in the US, generating light that is  $10^5$  times brighter than the sun. The light at the ALS is produced by accelerating a beam of electrons, which generates synchrotron radiation when the beam reaches the speed of light<sup>2</sup>.

### **2.2 Components of the ALS:**

The synchrotron at the ALS is comprised of 5 major components: the electron gun, linear accelerator, booster ring, storage ring, undulators (insertion devices) and beamlines, which can be seen in Figure 2.1.



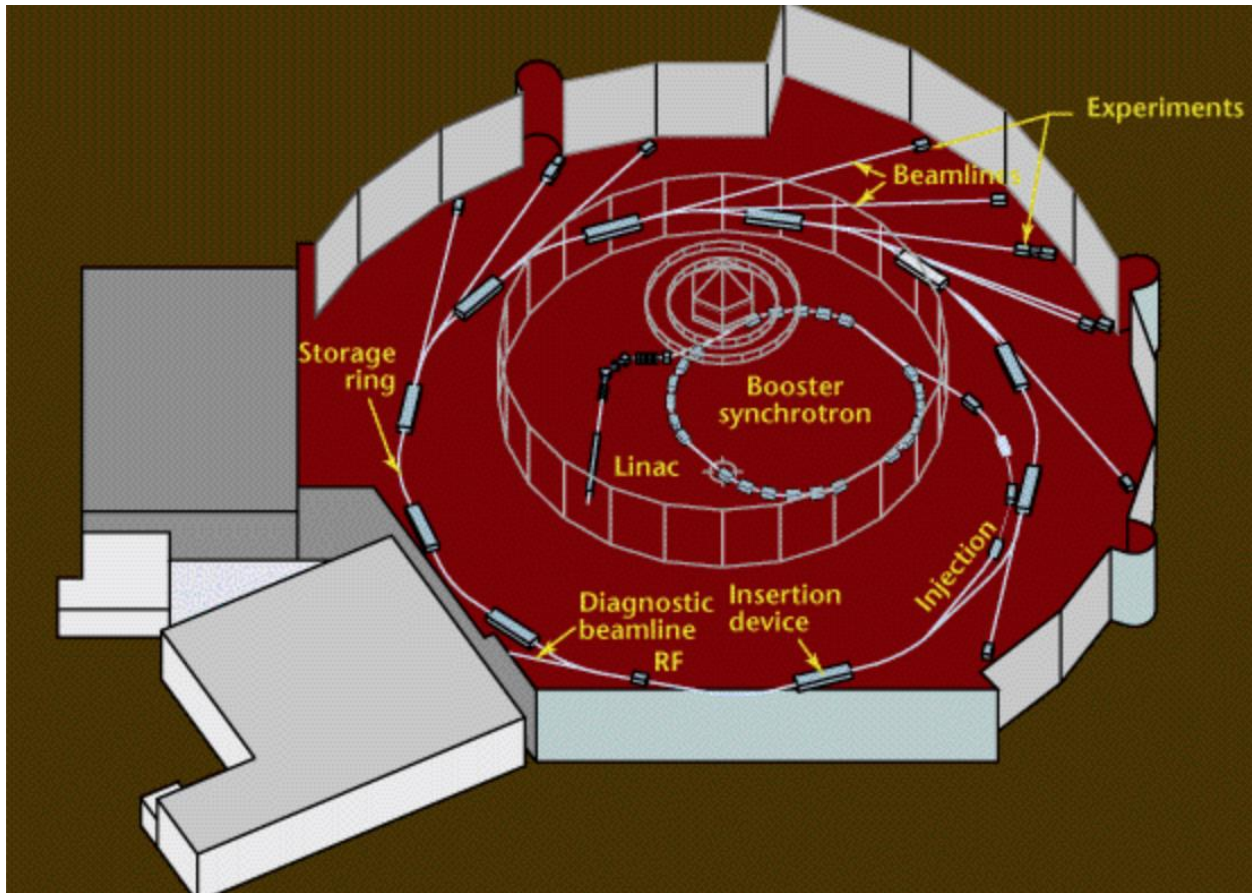


Figure 2.1: Schematic of the ALS components at Lawrence Berkeley National Laboratory<sup>3</sup>

### 2.2.1 The linear accelerator (linac):

The linear accelerator is an electromagnetic catapult that accelerates electrons to a relativistic velocity. The linac is 4 meters long and consists of 3 components, the electron gun, the buncher, and the linac itself. Acceleration begins in the cathode of the electron gun, where electrons are generated from the heating of the thermionic material barium aluminate<sup>4</sup>. The electrons are then drawn to the gate by a strong positive pulse at a frequency of 500 MHz. Once through the gate, the electrons are guided to the anode then led into the buncher. The buncher accelerates the

electrons and packs them into bunches with help of microwave radiation generated by a klystron. As the electron beam enters the linac, it gains 60% of the speed of light<sup>3</sup>. The linac then further accelerates the electron beam to almost the speed of light by applying radio-frequency (RF) waves.

### 2.2.2 Booster Synchrotron:

The booster synchrotron speeds the electron beam up to 99.999994% of the speed of light with help from the RF waves. The electrons are hit with 500 MHz RF pulse with each revolution around the booster, which bunches the electron beam and replaces the energy that was lost in rotation<sup>1</sup>. Once the electrons reach an energy of 1.5 GeV, they are injected into the storage ring.

### 2.2.3 The Storage Ring, and Undulators:

The electrons then enter the storage ring, where they circulate for hours. The storage ring consists of hundreds of electromagnets placed in 12 arc-shaped sections joined by 12 straight sections (undulators/wigglers)<sup>3</sup>. These electromagnets focus and bend the electrons as they circle the ring at more than one million times a second. When the electrons enter the straight section, the undulators wiggle the electrons back and forth illustrated in figure 2.2, which produces synchrotron light<sup>5</sup>. Synchrotron radiation is emitted by these electrons, and is directed to beamlines to be used in experiments.

# ALS Radiation is Produced by Bend Magnets and Undulators

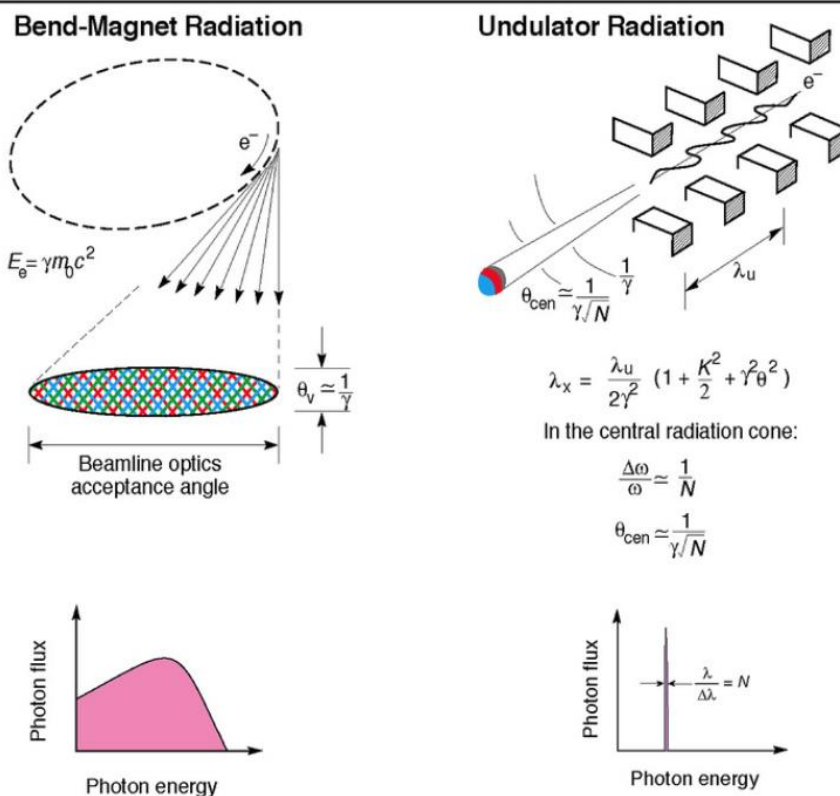


Figure 2.2: Illustration of Synchrotron radiation generated from the bending of magnets and undulators<sup>5</sup>.

## 2.2.4 The ALS beamline:

The beamline used to conduct our experiments is beamline 9.0.2.3, a multiplexed photoionization mass spectrometer (figure 2.3) coupled to tunable synchrotron radiation. The instrument consists of a chemical reactor, a time of flight mass spectrometer, and an ion detector<sup>6</sup>. After the synchrotron radiation leaves the storage ring it then passes through a gas

filter, which is an absorption cell filled with 30 torr of either Kr or Ar gas. The radiation is then focused by a 3 mm Eagle monochromator, and tuned to an energy range of 7-25 eV to be used at various beamlines.

All samples are prepared in gas cylinders, and are prepared and vaporized into the gas phase using a glass bubbler and thermostat bath. Samples are kept under a vacuum, and are frozen and thawed using the freeze-pump-thaw technique to remove unwanted impurities. The sample is prepared using helium as a carrier gas

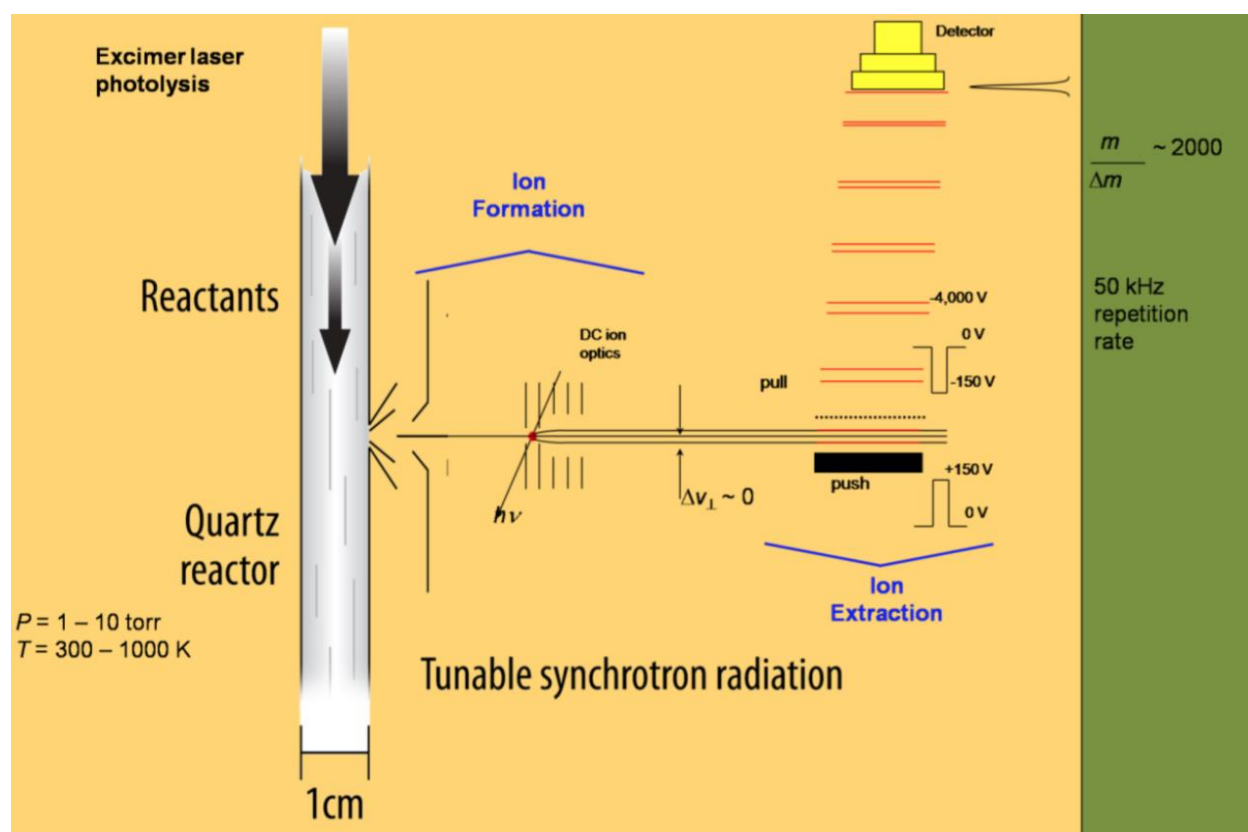


Figure 2.3: Schematic of the TOF-MS at beamline 9.0.2.3<sup>6</sup>.

## 2.3 The Experimental Apparatus

### 2.3.1 Excimer Laser:

The oxidation reactions in this investigation are initiated by chlorine radicals, generated from the photolysis of  $\text{Cl}_2$  using an excimer laser. An excimer laser generates ultra-violet light by running an electrical current through a mixture of noble and halogen gases<sup>7</sup>, specifically Xe and F for this investigation. The general schematic for an excimer laser can be seen in Figure 2.4. When the current is passed through these gases, they are stimulated to an excited electronic state, and form an excited dimer or “excimer”. These excited dimers quickly decay to the ground state, which releases a photon in the form of UV light<sup>8</sup>. This investigation uses the excitation and relaxation of xenon and fluorine molecules, which produces a photon at a wavelength of 351 nm.

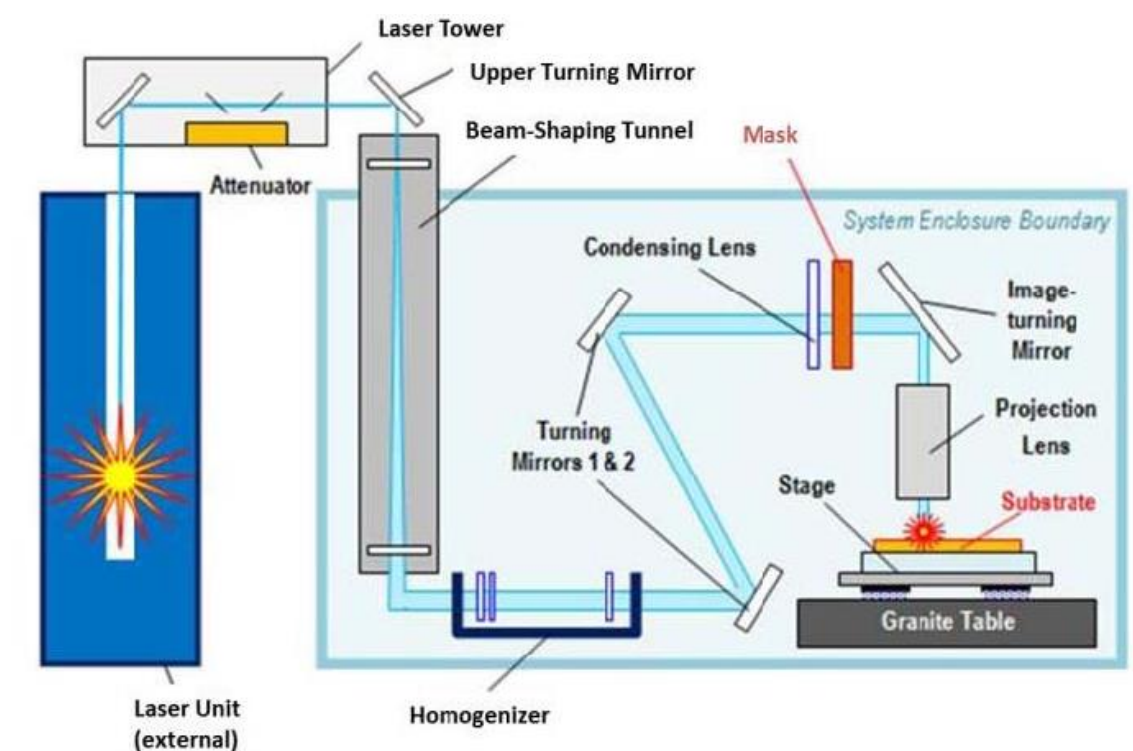


Figure 2.4: Schematic of an excimer laser<sup>8</sup>.

### 2.3.2 Vacuum System:

Vacuum pumps are used during experiments to prevent potential photon absorption from extraneous sources. The vacuum system for the beamline consists of three types of vacuum pumps, that are used to ensure the instrument remains free of contaminants: turbomolecular pumps, root pumps, and backing scroll pumps<sup>9</sup>. The largest of these pumps is the turbomolecular pump, which is a system of moving and stationary blades arranged in levels seen in Figure 2.5. The turbomolecular pump is involved in the evacuation of the source chamber, where the gas mixture is compressed and forms a molecular beam. Two turbomolecular pumps are used in the apparatus, one for the ionization region operating at 1600 L/s, and one used in the detector region at 600 L/s<sup>10</sup>. These pumps work by using the collision between the gas molecules and the solid surface of the rotors, where the rotors and stator blades push the gas molecules from inlet to outlet before flowing to the exhaust, and maintains a vacuum of  $10^{-8}$  torr<sup>11</sup>.



Figure 2.5: Cross section of a turbo molecular pump<sup>11</sup>



The turbomolecular pumps are assisted by backing scroll pumps, which consist of two scrolls, one stationary and one moving illustrated by figure 2.6. These pumps have a pumping speed of 20 – 50 m<sup>3</sup>/h and operate at a pressure range of 1000 to 10<sup>-2</sup> mbar<sup>12</sup>. These pumps work by oscillating one of the scrolls in a circular motion, which compresses the gas until it reaches a high pressure<sup>13</sup>. The backing scroll pump provides a contamination free environment since the system is oil free.

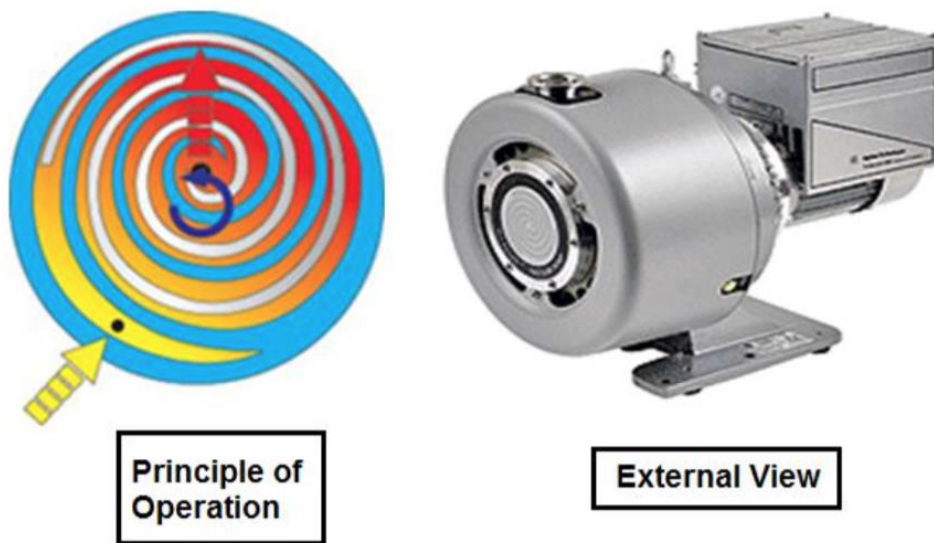


Figure 2.6: Schematic of the backing scroll pump mechanism<sup>12</sup>.

The evacuation of the apparatus is controlled by root pumps, which are used in a series with both the turbomolecular and backing scroll pumps. The root pumps also control the pressure of the reactor using two symmetrically shaped rotors that rotate in opposite directions which can be seen in Figure 2.7<sup>9</sup>. These rotors can expel large volumes of gas when rotating at high velocities, but lower rotation speeds are required for higher pressures to prevent overheating. The

root pump system has an operational capacity of 75 – 30,000 m<sup>3</sup>/h, and an operational range of 10 – 10<sup>-3</sup> mbar total pressure<sup>13</sup>.

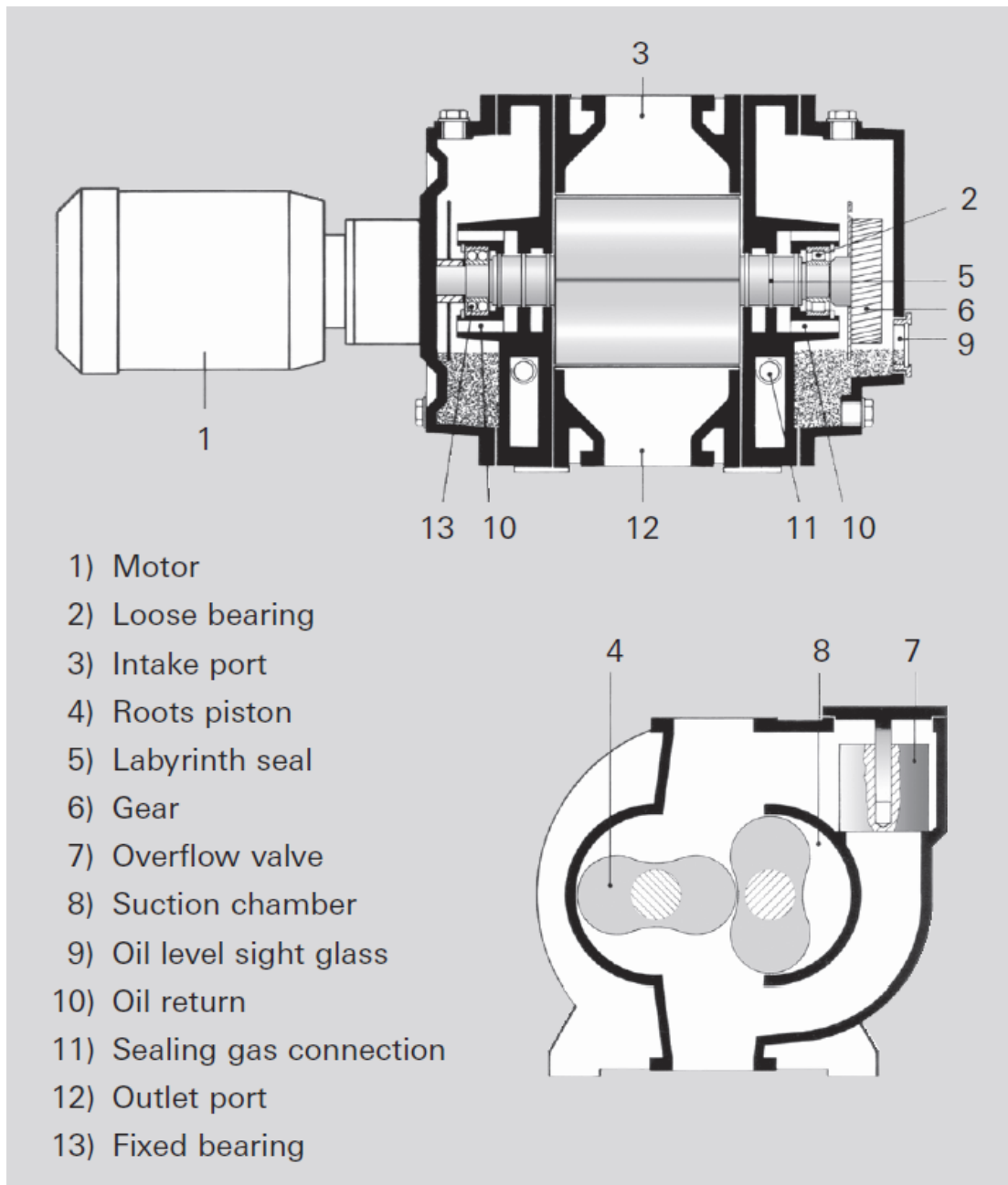


Figure 2.7: Schematic of root pump mechanism<sup>13</sup>.



### 2.3.3 Time of Flight Mass Spectrometer(TOF-MS):

The apparatus uses a McLaren time of flight mass spectrometer, which consists of an orthogonal acceleration TOF. This spectrometer is able to continuously detect both products and reactants over a specific range of masses. After the reaction occurs in the quartz slow flow reactor tube, products and reactants effuse through a pinhole and form a molecular beam, which is then ionized by VUV radiation<sup>14</sup>. Once the species enter the ionization region, the ions are extracted at a rate of 50 kHz and are accelerated to the detector. All ions acquire the same kinetic energy (KE), so smaller masses ( $m$ ) will reach detector first since they will have a greater velocity( $v$ )<sup>15</sup>. The kinetic energy of each ion can be found using Equation 2.1,

$$KE = \frac{1}{2} mv^2 = zV \quad (2.1)$$

Where  $v$  is the velocity of an ion,  $m$  is the mass of the ion,  $z$  is the charge of the ion, and  $V$  is the voltage applied for the electric field. The time of flight ( $T_f$ ) needed for an ion to travel the length of the flight tube ( $L$ ) is expressed in Equation 2.2 :

$$T_f = L/v \quad (2.2)$$

The relationship between the time of flight and mass-to-charge ratio can be determined experimentally using a calibration equation to solve for the slope and intercept, by measuring the time of flight(TOF) of a specific product and plotting the spectra vs a measure TOF of a known  $m/z$ . The calibration equation is generated by combining Equations 2.1 and 2.2 together:

$$T_f = \alpha + \beta\sqrt{m/z} \quad (2.3)$$

In the equation above  $\alpha$  represents the y intercept and  $\beta$  represents the slope. After the calibration equation is generated, it becomes possible to determine  $m/z$  of these unknown ions.

#### 2.3.4 MCP Detector:

Ions are detected by a time and position sensitive microchannel plate detector (MCP), which consists of a plate that amplifies the signal of the detected particles. MCPs work by transferring and intensifying the ion signal, and are composed of several channel electron multipliers (CEM). CEM tubes are about a micrometer in diameter and are packed within close proximity to one another. These tubes are oriented at an angle with respect to the incoming ion beam, which creates a high probability that the incoming ions will hit one of the surfaces of the CEM. The surfaces of the CEM are comprised of a semiconductor material, which generates secondary electrons when ions collide with the CEM<sup>16</sup>. These electrons are accelerated by an electric field which can be seen in Figure 2.8.

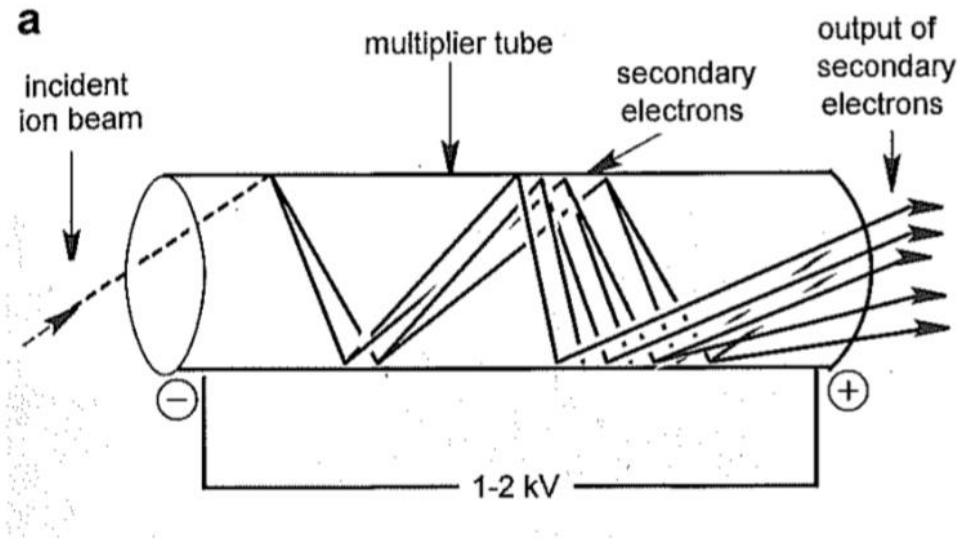


Figure 2.8: Schematic of a single linear channel electron multiplier(CEM)<sup>15</sup>.

Our apparatus contains a Chevron configuration which consists of two MCP's stacked on top of each other at opposing angles in order to amplify the signal (figure 2.9). Stacking 2 MCP like the Chevron configuration can allow for a gain of  $10^6 - 10^7$ , while stacking 3 plates like the z-stack will yield a gain up to  $10^{817}$ .

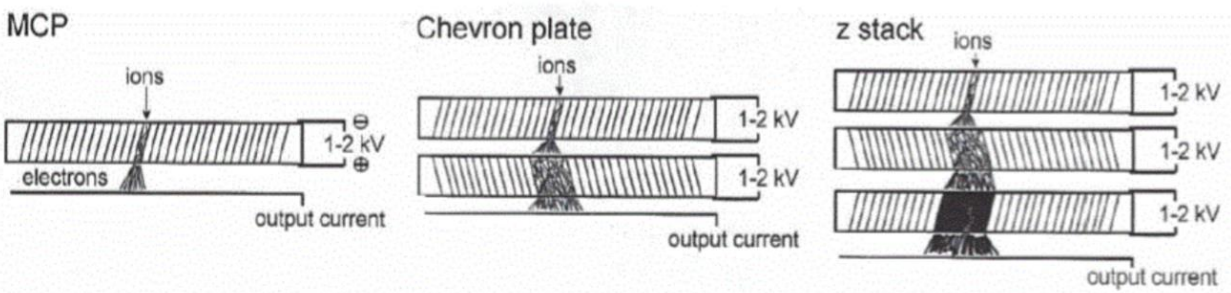


Figure 2.9: Schematic of multichannel plate displaying single, Chevron, and z-stack configurations<sup>15</sup>.

### 2.3.5 Data Analysis:

After the raw data is collected by the time-digital converter from the MCP output, a three-dimensional data set of time (ms), photon energy, and mass ( $m/z$ ) is obtained, which is illustrated by Figure 2.10. Since the three dimensional data is difficult to interpret, the data is then further broken down into two dimensional slices of photon energy vs  $m/z$  and time vs  $m/z$  using the software IGOR Pro by Wavemetrics<sup>18</sup>. The 2D data can be broken down further by taking 1D vertical slices of the individual masses. The vertical slices of the energy vs  $m/z$  are defined as photoionization (PI) curves, and the slices of the time vs  $m/z$  are defined as time traces.

PI curves are plotted as a function of ion signal versus photon energy and might represent the isomeric species at a specific  $m/z$ . These curves are used to identify the product species at each  $m/z$  using the adiabatic ionization energy obtained from the spectra onset. Reaction products are also identified by matching the experimental PI curves with known photoionization cross sections from the literature, or using FC simulations if the literature spectra are unknown. Kinetic time traces are used to monitor the formation or depletion of reaction species over time. Time traces are also used to determine the formation primary and secondary products by matching the slope of the product species to the reverse depletion of the reactant (the signal is multiplied by -1).

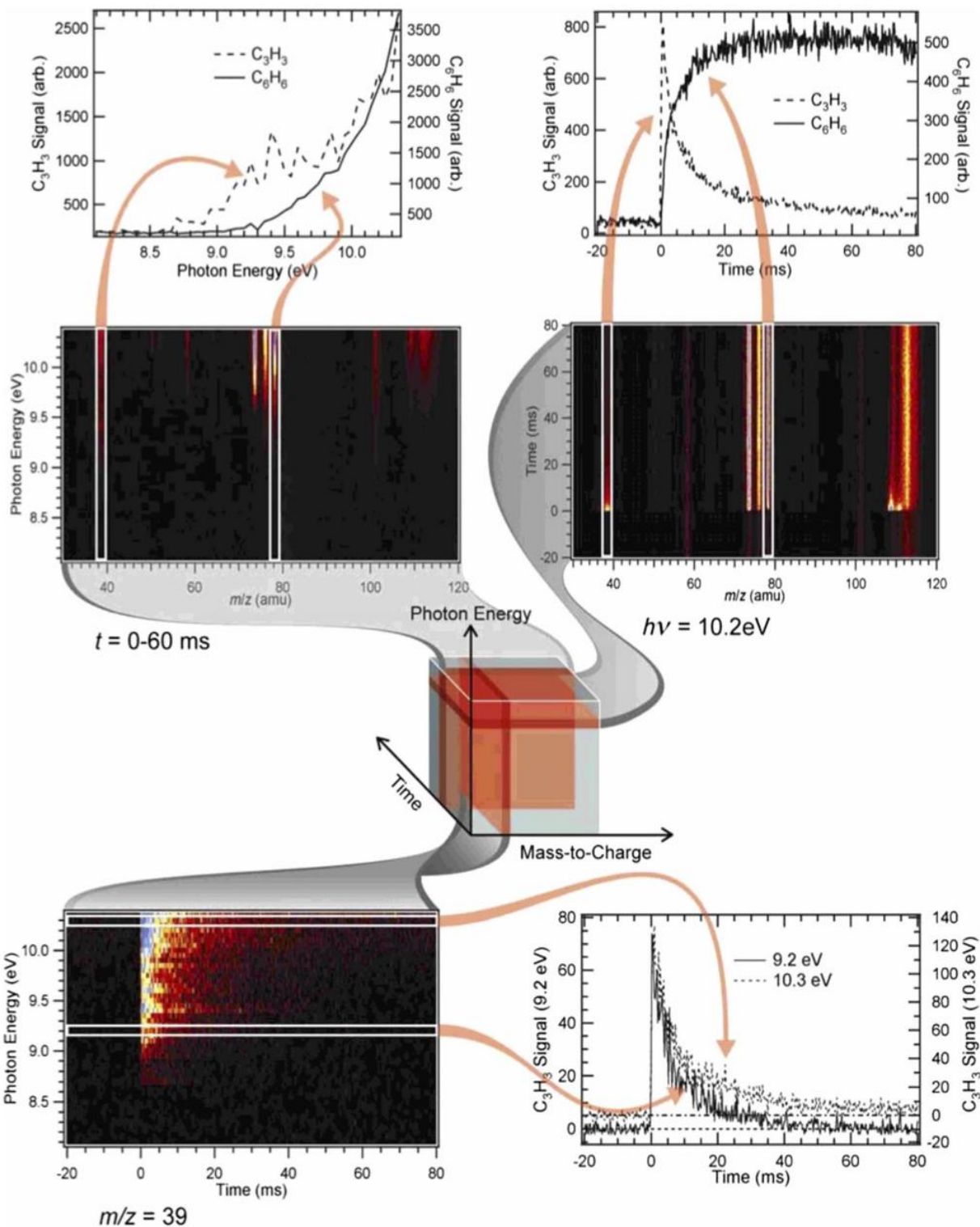


Figure 2.10: Diagram of the three dimensional dataset with 2D and 1D slices. PIE curve (top left), Time trace (top right)<sup>6</sup>.

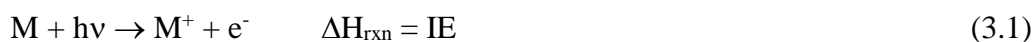
## 2.4 References:

1. Margaritondo, G., *Introduction to Synchrotron Radiation*. Oxford University Press: New York, NY, 1988.
2. ALS Facts. <http://als.lbl.gov/about/about-the-als/>.
3. ALS Tools. <http://www2.lbl.gov/MicroWorlds/ALSTool/>.
4. Rittner, E. S.; Rutledge, W. C.; Ahlert, R. H., The mechanism of operation of the barium aluminate-impregnated cathode. *J. Appl. Phys.* **1957**, *28*, 1468-73.
5. Attwood, D., Undulator Equation and Radiated Power. **2007**.
6. Osborn, D. L.; Zou, P.; Johnsen, H.; Hayden, C. C.; Taatjes, C. A.; Knyazev, V. D.; North, S. W.; Peterka, D. S.; Ahmed, M.; Leone, S. R., The multiplexed chemical kinetic photoionization mass spectrometer: a new approach to isomer-resolved chemical kinetics. *Rev Sci Instrum* **2008**, *79* (10), 104103.
7. Basting, D. M., G., *Excimer Laser Technology*. Springer: 2005.
8. Basting, D.; Stamm, U., The development of excimer laser technology - history and future prospects. *Z. Phys. Chem. (Muenchen, Ger.)* **2001**, *215* (12), 1575-1599.
9. Lafferty, J. M., *Foundation of Vacuum Science and Technology*. Wiley: New York, 1998.
10. Antoniou, A. G.; Valamontes, S. E.; Panos, C. N.; Valamontes, E. S., The turbomolecular pump in molecular state. *Vacuum* **1995**, *46* (7), 709-15.
11. Hsieh, F.-C.; Lin, P.-H.; Liu, D.-R.; Chen, F.-Z., Pumping performance analysis on turbomolecular pump. *Vacuum* **2012**, *86* (7), 830-832.
12. Li, Z.; Li, L.; Zhao, Y.; Bu, G.; Shu, P., Theoretical and experimental study of dry scroll vacuum pump. *Vacuum* **2009**, *84* (3), 415-421.
13. Vacuum, P. Design / Operating Principle. <https://www.pfeiffer-vacuum.com/en/know-how/vacuum-generation/roots-vacuum-pumps/>.
14. Margaritondo, G., A Primer in Synchrotron Radiation: Everything You Wanted to Know about SEX (Synchrotron Emission of X-rays) but Were Afraid to Ask. *J Synchrotron Radiat* **1995**, *2* (Pt 3), 148-54.
15. Gross, J. E., *Mass Spectrometry: A Textbook*. Springer: Berlin, 2004.
16. Westman, A.; Brinkmalm, G.; Barofsky, D. F., MALDI induced saturation effects in chevron microchannel plate detectors. *Int. J. Mass Spectrom. Ion Processes* **1997**, *169/170*, 79-87.
17. Elam, J. W.; Mane, A. U.; Peng, Q. Microchannel plate detector and methods for their fabrication. WO2012099658A2, 2012.
18. Wavemetrics, I. *IGOR Pro*, Portland, OR, 2013.

## Chapter 3: Theory

### 3.1 Photoionization:

The process of photoionization involves the removal of an electron by the absorption of electromagnetic radiation. Most conventional mass spectroscopic instruments employ the technique of electron bombardment with 70 eV of energy<sup>1</sup>. Electron bombardment ionization (EI) uses high energy electrons to bombard a gaseous neutral species. This transfers energy from the electron to the neutral molecule and this energy transfer is what ionizes the neutral compound. EI is not an ideal method for our combustion experiments since EI is obtained at an energy range between 60-80 eV, and would provide too much energy for our reactions. In addition, the energy resolution provided by EI is poor. Most molecules have ionization energies between 7.5 – 15 eV, so synchrotron radiation is utilized as the ionization source since the energy range can be tuned from 7.4 to 24.6 eV. The photoionization process can be represented by the equation below, where M is the neutral gaseous species, M<sup>+</sup> is cationic radical, h is Planck's constant,  $\nu$  is the frequency of light, and e<sup>-</sup> is the electron produced:



Ionization energy is defined as the minimum energy required to remove the first electron from an atom or molecule. The Planck equation relates the energy (E) used in ionization to the frequency of light, shown in the equation below:

$$E = h\nu \quad (3.2)$$

Ionization will occur if the energy of the photon is greater than the ionization threshold of the molecule. At energies close to or less than the ionization threshold of the molecule, the probability of ionization is very low.

### 3.2 Franck-Condon Principle:

Three types of electron transitions can occur during photoionization, and are discussed in this section, i.e., vertical, adiabatic, and dissociative, which are illustrated by Figure 3-1. These transitions occur when the molecule is excited by a photon. The molecule undergoes a vertical transition to its cationic state based on the Born-Oppenheimer approximation and Franck-Condon principle. An adiabatic transition is defined as the electronic transition from the neutral vibronic ground state to the cation vibronic ground state, with the energy difference of these two states being the adiabatic ionization energy (AIE). The AIE of the species of interest can be calculated and compared with its observed experimental value to help with the identification of the species. A molecule will undergo dissociative ionization when receiving energy equivalent to the AIE plus the dissociation/fragmentation energy for the specific cation (in case there is no barrier for dissociation).

The Born-Oppenheimer approximation states that electronic and nuclear motions can be treated separately, and the bond lengths and position of the atoms of the ionized molecule do not change upon ionization<sup>2</sup>. This approximation is due to the fact that the thermal velocity of a molecule is insignificant compared to the velocity of an electron. These wavefunctions can be factored individually based on their electronic and nuclear components, which is shown by equations 3.3.

$$\Psi_{molecule} = \Psi_{electron} \times \Psi_{nuclei} \quad (3.3)$$

Electronic transitions are also explained by the Franck-Condon principle, which states that the highest probability of an electron transition occurs when the electronic wave functions of the initial and final states are at their maxima<sup>3</sup>. This principle makes the assumption that nucleus remains stationary, so electronic transitions occur faster than nuclear movement<sup>4</sup>. The probability



that this transition will occur is based on the overlap of the wave functions of the cation and neutral species. The probability of a specific vertical transition from the vibrational ground state to the vibrational cationic state is proportional to its Franck-Condon factor ( $f_{FC}$ ). A greater overlap of the wavefunctions ( $M$  in Equation 3.4) will yield a larger Franck-Condon factor, which makes the transition very likely to occur, which is expressed in Equation 3.4.

$$M = \int \Psi_{gm}^*(r) \Psi_{xn}^*(r) dr \quad (3.4)$$

In Equation 3.4,  $\Psi_{gm}$  represents the  $m^{\text{th}}$  vibrational wavefunction of the neutral molecule, while  $\Psi_{xn}$  represents the cation, and  $r$  is the coordinate motion of the potential energy surface. The Franck-Condon factor is equal to the square of the matrix ( $M$ ) of the overlap integrals between the vibrational wavefunctions of the neutral and cationic state<sup>5</sup>. When the overlap of the two integrals is large, molecular rearrangement is minimal upon photoionization meaning that bond distances and angles remain unchanged.

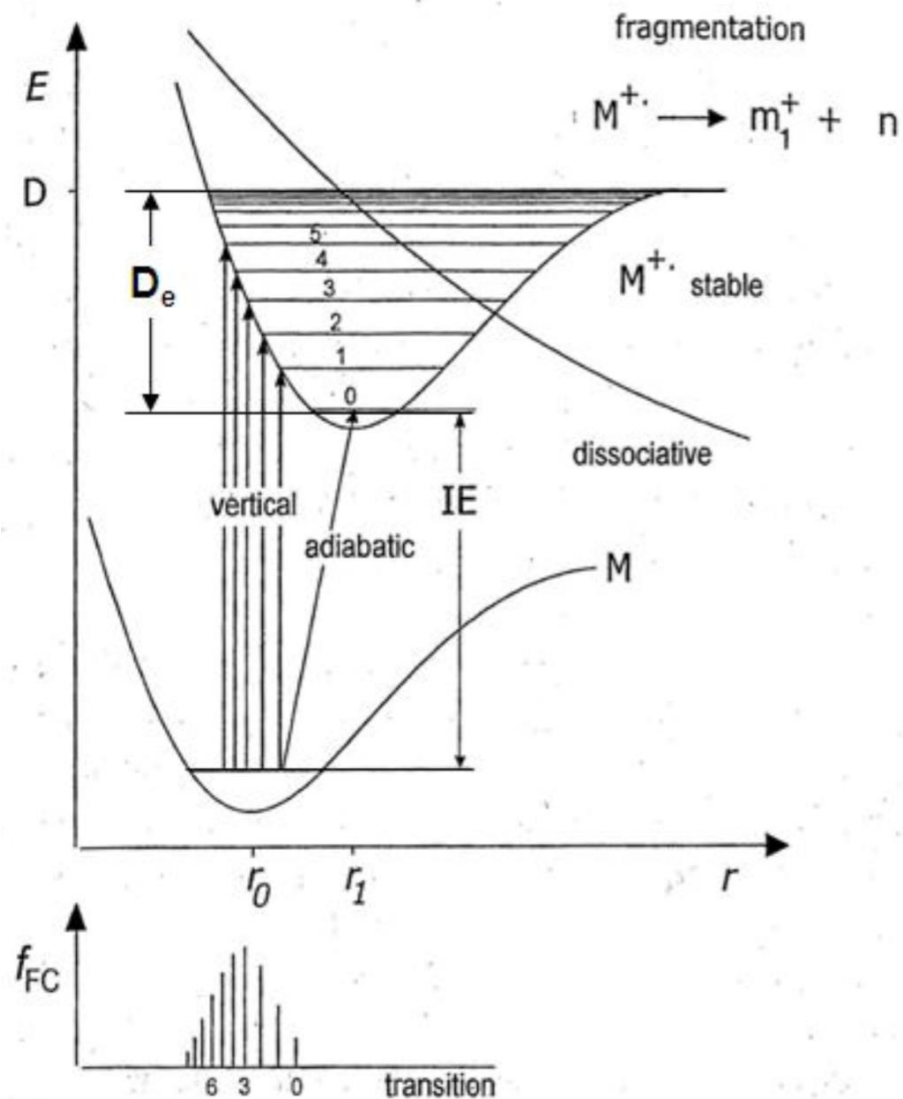


Figure 1: Diagram of the three types of electronic transitions for the neutral and cationic states, where the vertical lines represent  $0 \rightarrow n$  vibronic transitions. The letter D, the dissociation energy of the cation, represents where fragmentation occurs. An illustration of the Franck-Condon factor ( $f_{FC}$ ) is shown below the potential energy curves<sup>6</sup>.

### 3.3 Photoionization Spectra, Photoionization Cross Sections:

The photoionization spectrum is a graphical representation of the ion intensity versus photon energy of a given species. The shape of the overall spectra is determined by the Franck Condon principle. A larger Franck-Condon factor will have better overlap between the wavefunctions, which will cause a steep onset slope of the PI spectrum due to a higher intensity of the first electronic transition. Photoionization spectra have a unique shape for each molecule, which depends on the species ionization energy and wavefunction overlap. The identity of a particular ion signal of a specific mass can be identified by spectra shape agreement with a literature spectrum and mass-to-charge ratio.

Photoionization cross sections are defined as the effective area over which a gaseous atom or molecule is ionized by radiation<sup>7</sup>. If the incident photon has more energy than the AIE, the absorption of light by the bound quantum state causes the ejection of the outermost electron into a free state of positive energy in the continuum. The relationship between kinetic energy ( $k^2$ ) and the energy of the photon absorbed is expressed in the relationship below:

$$hv = (eV_i + k^2) \quad (3.5)$$

where  $e$  is the charge on the electron and  $V_i$  is the ionization threshold.

The newest approach for an approximation of the absolute photoionization cross section uses the initial and final states of a system, and condenses this information into a Dyson orbital<sup>8</sup>. The photoelectron matrix element  $D_k^{\text{IF}}$  is encoded with information about the initial and final electronic states, which is seen in the equation below:

$$D_k^{IF} = u(\phi_{IF}^d | r | \Psi_k^{el}) \quad (3.6)$$

where  $r$  is the dipole,  $u$  is the unit vector in the direction of the polarization of light,  $\phi_{IF}^d$  is the Dyson orbital connecting the initial and final electron states, and  $\Psi_k^{el}$  is the wavefunction of the ejected electron. The Dyson orbital connecting the initial N-electron and final N-1 electrons states is expressed below:

$$\phi_{IF}^d(1) = \sqrt{N} \int \Psi_i^N(1, \dots, n) \Psi_f^{N-1}(2, \dots, n) d2 \dots dn. \quad (3.7)$$

A strong orthogonality between  $\phi_{IF}^d$ ,  $\Psi_k^{el}$ , and the N-initial and N-1-final electron states is assumed based on Koopmans' theorem, which states that for closed-shell Hartree-Fock theory, the first ionization energy of a molecular system is equal to the negative of the orbital energy of the highest occupied molecular orbital (HOMO) of the ground state<sup>9</sup>. This assumption from Koopmans' theorem allows for the correlation between the total cross section and  $D_k^{IF}$ , expressed below:

$$\sigma_k = \frac{4\pi k E}{c} |D_k^{IF}|^2 \quad (3.8)$$

Where  $c$  is the speed of light in a vacuum,  $E$  is the energy of the ionizing radiation,  $k$  is the magnitude of the photoelectron wave vector in relevance to its kinetic energy,  $E_k$ , by  $k = \sqrt{2E_k}$ .

The relationship between photoionization cross section and ion signal can be seen in equation 3.9:

$$S_{(E)} = k \sigma_{(E)} \delta C \quad (3.9)$$

where (C) is the concentration of the molecule, k is the instrument constant, and  $\delta$  is the mass discrimination factor, which is equal to the mass (m) to the power of 0.67<sup>10</sup>. The mass discrimination factor represents the detector's efficiency in detecting the reaction species. The photoionization cross sections are measured in Megabarn (Mb) that is a unit equal to 10<sup>-18</sup> cm<sup>2</sup>. The ion signal in the photoionization spectrum is calibrated against a known concentration and cross section, specifically propene in our experiments<sup>11</sup>. Photoionization cross sections of products can be calculated using a known calibrant as a reference. The following equation was taken from Cool et al<sup>12</sup> and Welz et al<sup>13</sup>, and shows the relationship between these two quantities:

$$\sigma_{T(E)} = \frac{\sigma_{R(E)} S_{P(E)} m_r^{0.67} C_R}{S_{R(E)} m_p^{0.67} C_P} \quad (3.10)$$

where  $\sigma_{R(E)}$  is the photoionization cross section of the calibrant (reference), C<sub>P</sub> and C<sub>R</sub> are the concentrations of the product and reference, S<sub>R(E)</sub> is the signal of the calibrant reference, and m<sub>r</sub> and m<sub>p</sub> are the masses of the reference and product. The ion signals and photoionization cross sections are all taken at the same energy (E). Branching fractions are obtained by taking the ratio of C<sub>P</sub>/C<sub>R</sub>, when using C<sub>R</sub> as the concentration of the reactant. Branching fractions are used for the quantification of products and can only be obtained if the photoionization cross section is known, which will be explained further in Chapter 4.

### 3.4 Electronic Structure Calculations:

The investigations in this thesis employ computational software in the identification of photoionization products and reaction intermediates. This software is also utilized in calculating the energetics of superatom clusters. All structures and molecular parameters were optimized using the CBS-QB3<sup>14-15</sup> composite method and Gaussian 09<sup>16</sup> software coupled to GaussView 5.0<sup>17</sup> for visualization. The CBS-QB3 method is the only method used throughout this entire work because it is the most accurate in predicting adiabatic ionization energies of superalkali clusters and reaction species.

The CBS-QB3 method or complete basis set method (QB3 model) is a composite model that uses both ab initio and density function theory to deliver a highly accurate calculation, with an estimated energy error of only 1-1.5 kcal/mol<sup>18</sup>. CBS methods use different levels of theory, a wide variety of basis sets, and a linear combinations of atomic orbitals approximation to obtain the most accurate energies and molecular geometries. Computational basis sets are mathematical representations of molecular orbitals used to calculate the geometry of a molecule. Each basis set confines a particular electron to a specific region of the molecule. Larger basis sets have fewer constraints, which allows for a more accurate approximation of the electron's location. Molecular geometry optimizations and zero-point energy calculations in the CBS-QB3 method are performed at the B3LYP level of theory, which includes the CBSB7 basis set. The CBSB7 basis set also includes the basis set 6-311G(2d,d,p), which is the smallest basis set to obtain accurate B3LYP frequencies<sup>14, 19</sup>.

Vibrational frequencies, bond distances, and PES scans are optimized using the Becke three parameter exchange functional with the Lee, Yang, and Parr (B3LYP)<sup>20-21</sup> correlation

functional level of theory. The basis set used during the B3LYP calculations is 6-311+G\*\*, which is an all electron triple zeta valance basis set. The method of density functional theory uses the Hohenberg-Kohn and Kohn-Sham<sup>22</sup> theorems to calculate properties of molecules, and is based on electron probability density<sup>23</sup>. Transition states and intrinsic reaction coordinate (IRC)<sup>24</sup> calculations are also optimized at the B3LYP level of theory, which will be further explained in Chapter 4.

Calculations performed at the CBS-QB3 level of theory are helpful in the analysis of our experimental products when literature values such as ionization energies, and photoionization cross sections are unknown. Equation 3.11 shows how the enthalpy of reaction is related to the ionization energy, and the adiabatic ionization energy can be calculated by taking the difference of the CBS-QB3 zero point corrected (ZPE) total electronic energies between the neutral species and its corresponding cation. Reaction enthalpies are also calculated using the ZPE of the products and reactants, and is expressed in the relationship below:

$$\Delta H_{rxn} = \sum ZPE_{products}^{CBS-QB3} - \sum ZPE_{reactants}^{CBS-QB3} \quad (3.11)$$

Properties of superatom clusters such as atomization enthalpies, enthalpies of formation, fragmentation energies, and binding energies, are all calculated using ZPE at the CBS-QB3 level of theory. These quantities are all explained more extensively in the experimental sections of Chapters 4 and 5.

### 3.5 References:

1. Gross, J. H., *Mass Spectrometry, 2nd edition*. Berlin Heidelberg: Springer: 2011.
2. Born, M.; Oppenheimer, R., Quantum theory of the molecules. *Ann. Phys. (Berlin, Ger.)* **1927**, *84*, 457-84.
3. Franck, J., Elementary processes of photochemical reactions. *Trans. Faraday Soc.* **1925**, (advance proof).
4. Condon, E., Theory of intensity distribution in band systems. *Phys. Rev.* **1926**, *28*, 1182-1201.
5. Dunbrack, R. L., Jr., Calculation of Franck-Condon factors for undergraduate quantum chemistry. *J. Chem. Educ.* **1986**, *63* (11), 953-5.
6. Gross, J. E., *Mass Spectrometry: A Textbook*. Springer: Berlin, 2004.
7. Lee, P.; Weissler, G. L., The photoionization cross-section of neon. *Proc. R. Soc. London, Ser. A* **1953**, *220*, 71-6.
8. Gozem, S.; Gunina, A. O.; Ichino, T.; Osborn, D. L.; Stanton, J. F.; Krylov, A. I., Photoelectron Wave Function in Photoionization: Plane Wave or Coulomb Wave? *J. Phys. Chem. Lett.* **2015**, *6* (22), 4532-4540.
9. Koopmans, T., The distribution of wave function and characteristic value among the individual electrons of an atom. *Physica (The Hague)* **1933**, *1*, 104-13.
10. Welz, O.; Savee, J. D.; Eskola, A. J.; Sheps, L.; Osborn, D. L.; Taatjes, C. A., Low-temperature combustion chemistry of biofuels: Pathways in the low-temperature (550-700 K) oxidation chemistry of isobutanol and tert-butanol. *Proc. Combust. Inst.* **2013**, *34* (1), 493-500.
11. Cool, T. A.; Nakajima, K.; Mostefaoui, T. A.; Qi, F.; McLlroy, A.; Westmoreland, P. R.; Law, M. E.; Poisson, L.; Peterka, D. S.; Ahmed, M., Selective detection of isomers with photoionization mass spectrometry for studies of hydrocarbon flame chemistry. *J. Chem. Phys.* **2003**, *119* (16), 8356-8365.
12. Cool, T. A.; Wang, J.; Nakajima, K.; Taatjes, C. A.; McLlroy, A., Photoionization cross sections for reaction intermediates in hydrocarbon combustion. *Int. J. Mass Spectrom.* **2005**, *247* (1-3), 18-27.
13. Welz, O.; Klippenstein, S. J.; Harding, L. B.; Taatjes, C. A.; Zador, J., Unconventional Peroxy Chemistry in Alcohol Oxidation: The Water Elimination Pathway. *J. Phys. Chem. Lett.* **2013**, *4* (3), 350-354.
14. Montgomery, J. A., Jr.; Frisch, M. J.; Ochterski, J. W.; Petersson, G. A., A complete basis set model chemistry. VI. Use of density functional geometries and frequencies. *J. Chem. Phys.* **1999**, *110* (6), 2822-2827.
15. Montgomery, J. A., Jr.; Frisch, M. J.; Ochterski, J. W.; Petersson, G. A., A complete basis set model chemistry. VII. Use of the minimum population localization method. *J. Chem. Phys.* **2000**, *112* (15), 6532-6542.
16. Frisch, M. J. T., G. W.; Schlegel, H. B.; Scuseria, G. E.; Robb, M. A.; Cheeseman, J. R.; Scalmani, G.; Barone, V.; Mennucci, B.; Petersson, G. A.; Nakatsuji, H.; Caricato, M.; Li, X.; Hratchian, H. P.; Izmaylov, A. F.; Bloino, J.; Zheng, G.; Sonnenberg, J. L.; Hada, M.; Ehara, M.; Toyota, K.; Fukuda, R.; Hasegawa, J.; Ishida, M.; Nakajima, T.; Honda, Y.; Kitao, O.; Nakai, H.; Vreven, T.; Montgomery, J. A., Jr.; Peralta, J. E.; Ogliaro, F.; Bearpark, M.; Heyd, J. J.; Brothers, E.; Kudin, K. N.; Staroverov, V. N.; Kobayashi, R.; Normand, J.; Raghavachari, K.; Rendell, A.; Burant, J. C.; Iyengar, S. S.; Tomasi, J.; Cossi, M.; Rega, N.; Millam, N. J.; Klene, M.; Knox, J. E.; Cross, J. B.; Bakken, V.; Adamo, C.; Jaramillo, J.; Gomperts, R.; Stratmann, R.



- E.; Yazyev, O.; Austin, A. J.; Cammi, R.; Pomelli, C.; Ochterski, J. W.; Martin, R. L.; Morokuma, K.; Zakrzewski, V. G.; Voth, G. A.; Salvador, P.; Dannenberg, J. J.; Dapprich, S.; Daniels, A. D.; Farkas, Ö.; Foresman, J. B.; Ortiz, J. V.; Cioslowski, J.; Fox, D. J. *Gaussian 09, Revision A.1*, Gaussian, Inc.: Wallingford, CT, 2009.
17. Dennington, R. K., T.; Millam, J *GaussView*, 5, SemiChem Inc: Shawnee Mission KS, 2009.
  18. Sirjean, B.; Fournet, R.; Glaude, P.-A.; Ruiz-Lopez, M. F., Extension of the composite CBS-QB3 method to singlet diradical calculations. *Chem. Phys. Lett.* **2007**, *435* (1-3), 152-156.
  19. Lee, C.; Yang, W.; Parr, R. G., Development of the Colle-Salvetti correlation-energy formula into a functional of the electron density. *Phys. Rev. B: Condens. Matter* **1988**, *37* (2), 785-9.
  20. Becke, A. D., A new mixing of Hartree-Fock and local-density-functional theories. *J. Chem. Phys.* **1993**, *98* (2), 1372-7.
  21. Becke, A. D., Density-functional thermochemistry. III. The role of exact exchange. *J. Chem. Phys.* **1993**, *98* (7), 5648-52.
  22. Kohn, W.; Sham, L. J., Quantum density oscillations in an inhomogeneous electron gas. *Phys. Rev.* **1965**, *137* (6A), 1697-705.
  23. Kohn, W.; Sham, L. J. *Self-consistent equations including exchange and correlation effects*; Univ. of California: 1965; p 21 pp.
  24. Tirado-Rives, J.; Jorgensen, W. L., Performance of B3LYP Density Functional Methods for a Large Set of Organic Molecules. *J. Chem. Theory Comput.* **2008**, *4* (2), 297-306.

## Chapter 4 - Investigation of Oxidation Reaction Products of 2-Phenylethanol Using Synchrotron Photoionization

[This chapter was adopted from an article with the same title published in the Journal of Physical Chemistry A (J.Phys.Chem.A. 2018, 122(33), 6789-6798). Authors include Adam Otten, Magaly Wooten, Anthony Medrano, Yasmin Fathi, and Giovanni Meloni]

### Abstract

Photolytically Cl-initiated oxidation reaction of 2-phenylethanol (2PE) was carried out at the Advanced Light Source (ALS) in the Lawrence Berkeley National Laboratory. Using the multiplex photoionization mass spectrometer, coupled with the tunable vacuum ultraviolet radiation of the ALS, data were collected at low pressure (4 - 6 Torr) and temperature (298 – 550 K) regimes. Data analysis was performed via characterization of the reaction species photoionization spectra and kinetic traces. Products and reaction pathways are also computed using the CBS-QB3 composite method. The present results suggest as the primary products  $m/z = 30$  (formaldehyde), 106 (benzaldehyde), and 120 (phenylacetaldehyde) at 298 K, and  $m/z = 120$  (phenylacetaldehyde) at 550 K. Branching fractions at room temperature are  $27 \pm 6.5 \%$  for formaldehyde,  $24 \pm 4.5 \%$  for benzaldehyde,  $25 \pm 5.8 \%$  for phenylacetaldehyde, and for phenylacetaldehyde at 550 K are  $60 \pm 14 \%$ .

#### **4.1 Introduction:**

Limited resource of fossil fuels and the growing global demand for energy has increased the world's investment in finding alternative fuels, which would be both efficient and environmentally friendly.<sup>1-4</sup> One of such alternatives is biofuels. The implementation of biofuels could significantly decrease carbon emissions and offer a long-term renewable solution to petroleum based fuels.<sup>3, 5</sup> The United States plans to increase the amount of biofuel used from 9 billion gallons in 2008 to 36 billion gallons in 2022.<sup>6-7</sup> Even though the biofuels currently used have proven to provide visible benefits over fossil fuels, new technology and further research are required to perfect, advance, and increase their impact in the world.<sup>1, 8-9</sup> Furthermore, there is a need for multiple alternative fuels to supplant both gasoline and petroleum diesel, as they have chemically different requirements, such as branching and saturation that must be considered.

Ethanol currently dominates the biofuel market. However, ethanol tends to absorb water, is corrosive, and has a low conversion efficiency from feedstock to fuel.<sup>2</sup> Because of its predisposition to absorb water, ethanol cannot be distributed using the existing fuel system and would require its retrofitting. Moreover, controversy surrounds ethanol's energy per liter capability; there is some reservation on whether the energy contained in ethanol itself is significantly greater than the energy used to grow and process it from crops.<sup>10-11</sup> Although much improvement to ethanol production has been made over the past few years, other potential biofuels are now stealing the focus. One such alternative is 2-phenylethanol (2PE). As a higher alcohol than ethanol, 8 carbon atoms versus 2 carbon atoms, 2-phenylethanol has a higher energy density, and lower hygroscopicity and volatility. Further studies of 2PE combustion products will determine if indeed this alcohol could be used as biofuel.

The oxidation of aromatic compounds has been investigated extensively through a wide variety of techniques and holds relevance in both fossil fuel combustion and atmospheric pollution formation.<sup>12-14</sup> This investigation differs from other aromatic oxidation studies since we are observing reactions only with the ethanol side chain of 2PE and not the aromatic ring, so the oxidation of ethanol must be considered. Ethanol oxidation has been studied through various methods because of its role in fuel combustion.<sup>15-17</sup> While the chlorine initiated oxidation of ethanol has not been investigated, its OH initiated oxidation has been examined.<sup>18-20</sup> These studies have found acetaldehyde and formaldehyde as products,<sup>15-17</sup> which are seen in this investigation of 2PE at room temperature. An example of a higher alcohol OH initiated oxidation is isobutanol investigated by Welz and coworkers<sup>21</sup> at 550 and 700 K using multiplexed synchrotron photoionization mass spectrometry and again it was found that both formaldehyde and acetaldehyde are reaction products.

2-Phenylethanol is an organic compound with the formula  $C_6H_5CH_2CH_2OH$ . Its increased stability and higher energy density than ethanol places 2PE closer to the properties of gasoline, consequently making it an attractive alternative. Ethanol's high vapor pressure (44.6 mmHg at 20 °C) is also detrimental to air quality; while 2-PE has a very low vapor pressure (0.126 mmHg at 20 °C).<sup>22</sup> Another desirable quality of 2PE is its branched chain. Branched-chain alcohols have higher octane numbers than those with straight-chains.<sup>2</sup> Octane numbers are a standard measure of fuel performance; the higher the octane number, the more compression the fuel can withstand. Fuels with higher octane number make a good fit for high-compression engines, which in turn generally provide higher performance.

Higher alcohols such as 2PE, however, tend to face the complication of not being economically produced in large enough quantities for fuel application. One exception to this is n-

butanol.<sup>23-24</sup> The newly found ability to efficiently produce 2PE in large quantities from glucose,<sup>25</sup> which is widely available in nature, adds to its attraction as a possible biofuel. In addition, 2PE occurs naturally in the essential oils of various plants and flowers.<sup>26</sup> It is traditionally synthesized from benzene and ethylene oxide through Friedel–Crafts alkylation reaction.<sup>27</sup>

The study of the elementary reactions of 2PE provides valuable insight on its combustion potential as a biofuel and allows for the investigation of its products and potential pollutants. This work investigates the products characterization from the reaction of 2PE + Cl + O<sub>2</sub> at 298 and 550 K. Reaction mechanisms are postulated using electronic structure calculations of the potential energy surface from the initial H abstraction radical plus O<sub>2</sub>.

## **4.2 Experimental:**

### *Apparatus*

Reactions are carried out using a multiplexed time-resolved mass spectrometer at the Advanced Light Source (ALS) of Lawrence Berkeley National Laboratory. The apparatus is described in further detail elsewhere.<sup>28-30</sup> The instrument consists of a chemical reactor with a vacuum system, a photoionization source, a mass spectrometer, and an ion detector. The reaction species are ionized by continuously tunable vacuum ultraviolet synchrotron radiation with energies ranging from 8.0 to 11.0 eV with 0.025 eV increments. 2PE ( $\geq 98\%$  Sigma Aldrich) is transported into the gas phase by bubbling helium through the liquid placed in a glass bubbler inside a thermostated glycol bath.<sup>28</sup> The sample, radical precursor (Cl<sub>2</sub>), and inert gas (He), flow through individual calibrated mass flow controllers into a 62 cm quartz slow flow reactor tube

held at a constant pressure (4 or 6 torr) and temperature (298 or 550 K). The chlorine radical required here is formed from the radical precursor  $\text{Cl}_2$  through photolysis *in situ* using 351 nm excimer laser pulses at a rate of 4 Hz. The number densities (at 298 and 550 K, respectively) are  $9.7 \times 10^{12}$  and  $8.8 \times 10^{12}$  molecules  $\text{cm}^{-3}$  for 2PE,  $2.3 \times 10^{13}$  and  $1.5 \times 10^{13}$  molecules  $\text{cm}^{-3}$  for  $\text{Cl}_2$ , and  $5.4 \times 10^{16}$  and  $2.5 \times 10^{16}$  molecules  $\text{cm}^{-3}$  for  $\text{O}_2$ .

The IUPAC Subcommittee for Gas Kinetic Data Evaluation recommended 1.00 to be used as the quantum yield of the  $\text{Cl}_2$  photolysis,<sup>31</sup> with the absorption cross section of its photolysis at 351 nm reported as  $1.82 \times 10^{-19}$   $\text{cm}^2$  according to Maric et al.<sup>32</sup> Based on these values, the number density of Cl in our experiments are  $1.1 \times 10^{12}$  to  $2.4 \times 10^{12}$  molecules  $\text{cm}^{-3}$  at 298 and 550 K, respectively, which makes the concentration of 2PE about 4 - 10 times the concentration of Cl used to initiate H abstraction in the oxidation reactions. The absolute photoionization spectra of possible products styrene ( $\geq 99.9\%$  Sigma Aldrich), benzaldehyde ( $\geq 99\%$  Sigma Aldrich), and phenylacetaldehyde ( $\geq 90\%$  Sigma Aldrich) are taken for data analysis purposes.

Reaction products effuse from the reactor tube through a 650  $\mu\text{m}$  pinhole into the source chamber that has been evacuated by a 3200  $\text{L s}^{-1}$  turbomolecular pump. The molecular beam then enters the ionizing chamber through a 0.15 cm diameter skimmer, where it is perpendicularly intersected by the tunable vacuum ultraviolet synchrotron radiation from the Chemical Dynamics Beamline of the ALS, using a 10 cm period undulator and selected by a 3-m monochromator. Higher undulator harmonic frequencies generated by the undulator are removed through a windowless absorption gas cell filled with 30 Torr of Ar or Kr. The resulting ions are accelerated according to their mass-to-charge ratio ( $m/z$ ) by an orthogonal-acceleration time-of-flight mass spectrometer pulsed at 50 kHz<sup>33</sup> and detected with a microchannel plate (MCP) detector.

The raw data consists of a three-dimensional data block (mass to charge ( $m/z$ ), reaction time ( $t$ ), and photon energy ( $E$ ) vs. the ion intensity ( $I$ )). Photon energy in this experiment is varied between 8.0 and 11.0 eV in increments of 0.025 eV. The ion signal at each photon energy is background-subtracted and normalized for the photon current, which is measured by a calibrated VUV-sensitive photodiode present in the ionization region. Data obtained can be further integrated over a photon energy or temporal range, to obtain time-resolved mass or photoionization spectra, respectively. This is achieved by fixing one observable,  $t$  or  $E$ , and integrating over the other one. The reaction begins at 0 ms when the photolysis laser is fired and it is followed up to 60 ms for 298 K and up to 40 ms for 550 K in order to minimize the integration of signal containing possible secondary chemistry. The photoionization spectrum of each  $m/z$  is corrected for possible dissociative fragmentation and isotopic contribution. Spectra at each  $m/z$  differ because of different Franck-Condon factors, thus allowing for identification of the species responsible for the signal. Isomers are distinguished based on their differing onset ionization energies and spectrum shape. Species are identified, by comparing the measured spectra with computed Franck-Condon envelopes, or literature spectra and absolute photoionization cross sections when available.

### *Computation*

Structural parameters of the reaction species are computed using the CBS-QB3 (Complete Basis Set) composite method.<sup>34-35</sup> Optimized geometries and energetics are completed for neutral and cationic species utilizing the Gaussian 09<sup>36</sup> program suite coupled with Gaussview 5.0<sup>37</sup> for visualization.

Adiabatic ionization energies (AIE) are obtained by performing CBS-QB3 calculations on the ground state neutral and cation (+1 charge) state of each species. The AIE is defined as

the difference of the zero point corrected (ZPE) total electronic energies ( $E_0$ ) between the neutral species and its corresponding cation. Uncertainties for such calculations are within 0.05 eV.<sup>34</sup> Enthalpies of reactions ( $\Delta_r H^\circ$ ) are calculated using the ZPE total corrected electronic energies, and are used to determine if our mechanisms are thermodynamically possible. Potential energy surface scans are used to locate transition states and products from hydrogen abstraction, oxygen addition, and hydrogen transfers. Transition states are optimized using the CBS-QB3 composite model, followed by an intrinsic reaction coordinate (IRC)<sup>38</sup> calculation to confirm both the forward and reverse reaction mechanisms of these species.

Photoionization spectra are also used to determine product concentration by the relationship between spectral intensity at a specific photon energy ( $S_E$ ), and concentration ( $C$ ), expressed in equation 1 below.

$$S_E = k\sigma_E\delta C \quad (1)$$

where  $\sigma_E$  is the photoionization cross section at a specific photon energy,  $k$  is the instrumental constant, and  $\delta$  is the mass discrimination factor, which is equal to the mass ( $m$ ) of the observed species to the power of 0.67.<sup>21</sup> Absolute PI spectra or curves are generated by plotting photon energy versus photoionization cross section, which if unknown, can be obtained by comparing the authentic PI spectrum of a sample of the pure species with the absolute photoionization cross section of a reference species. The reference absolute photoionization cross section used in this work is propene.<sup>39</sup>

Branching fractions, i.e., the ratio of product over reactant concentration ( $C_P$  and  $C_R$ ) in equation 2, are calculated using the absolute cross section values of the reactant species from the method above, the measured signals, and the mass discrimination factors (MDF):



$$\frac{C_P}{C_R} = \frac{\frac{S_P}{\sigma_P \delta_P}}{\frac{S_R}{\sigma_R \delta_R}} = \frac{S_P \sigma_R \delta_R}{S_R \sigma_P \delta_P} = \frac{S_P \sigma_R}{S_R \sigma_P} \left( \frac{m_R}{m_P} \right)^{0.67} = \frac{S_P \sigma_R}{S_R \sigma_P} \text{MDF} \quad (2)$$

### 4.3 Results and Discussion:

In the present work, the oxidation of 2PE is initiated by hydrogen abstraction from chlorine radicals. 2PE is a cyclic alcohol containing an unsaturated phenyl ring attached to an ethanol group. Chlorinated products are formed during secondary reactions with primary products, and from chlorine addition to our parent compound (addition to the ring). These chlorinated species are identified by the isotopic ratio  $^{35}\text{Cl}/^{37}\text{Cl}$  from the signal intensity of the photoionization spectra, which is about 1:3. Species  $m/z = 112/114$ ,  $126/128$ ,  $140/142$ , and  $156/158$  are identified as chlorinated products from their isotopic ratio. For example,  $m/z = 140/142$  has an ionization onset of 9.60 eV matching with the photoionization value of 9.69 eV<sup>40</sup> of benzoyl chloride generated from the secondary reaction of  $m/z = 106$  (benzaldehyde) with Cl. These products are not fully identified or characterized during this investigation since they are generated through secondary chemistry and is, therefore, beyond our scope.

The analysis of the reaction  $2\text{PE} + \text{Cl} + \text{O}_2$ , is divided into two sections based on experimental temperature. Activation enthalpies and enthalpies of reactions of products are calculated using the zero point corrected total electronic energies using the CBS-QB3 model, and are used to verify product identification and to postulate pathways. Figure 1 presents the mass spectra of the room temperature and 550 K data taken for a photon energy of 10.7 eV.

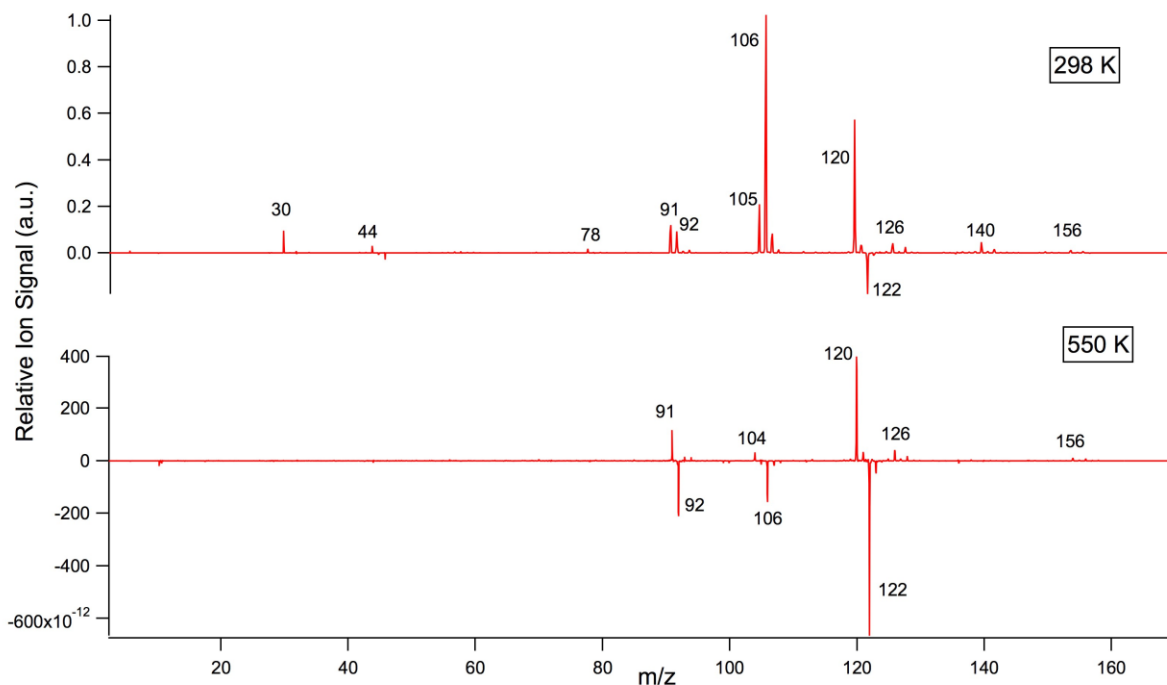


**Figure 1.** Mass spectra taken at 10.7 eV for the 298 and 550 K data.

### Product Identification 2PE + Cl + O<sub>2</sub> at 298 K:

Upon the addition of oxygen, the following masses are observed and characterized as primary products:  $m/z = 30$ , 106, and 120.  $m/z = 44$ , which has a fast formation comparable with the reactant depletion (see below), based on the computation of the potential energy surface is a secondary product (see Proposed Mechanism section). The experimental photoionization spectra for  $m/z = 30$  matches well with the literature photoionization spectra of formaldehyde,<sup>41</sup> shown in Figure 2 a). The experimental PI spectrum of  $m/z = 44$  with an onset of  $10.18 \pm 0.05$  eV is compared to the literature spectrum of acetaldehyde (Figure 2 b) by Cool et al.<sup>39</sup> and is in good agreement with the literature value of  $10.20 \pm 0.05$  eV.<sup>42</sup>

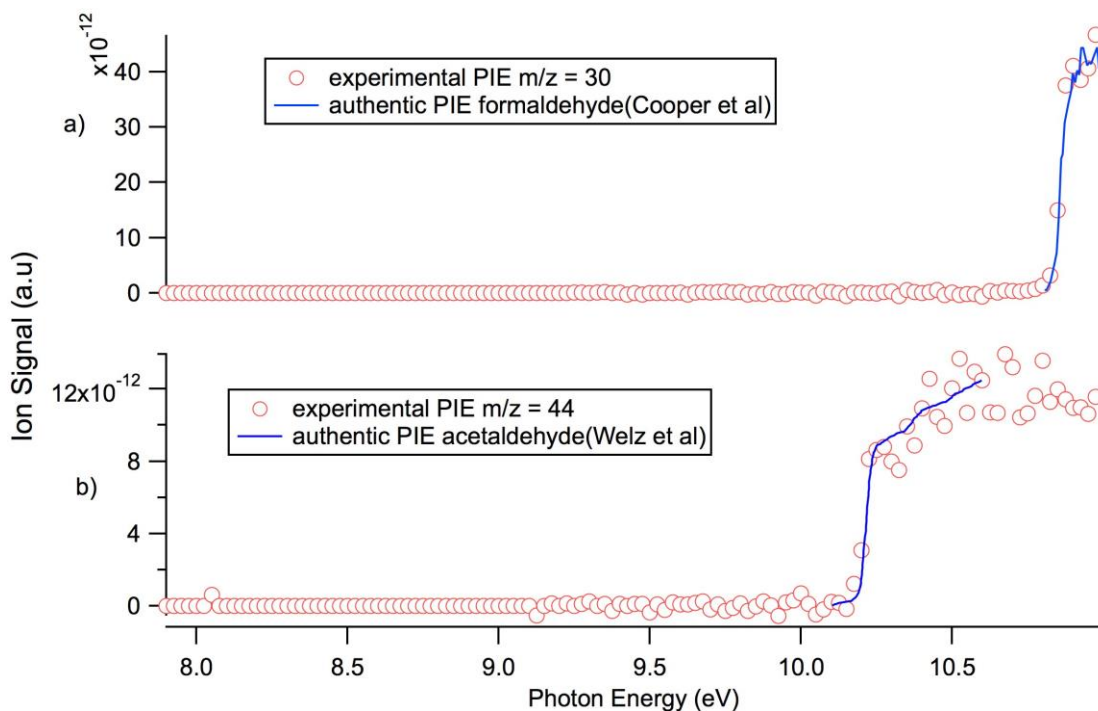


**Figure 2.** a) Authentic PI spectrum of formaldehyde (blue line) recorded by Cooper et al.<sup>41</sup> compared to the experimental  $m/z = 30$  spectrum (red open circles) at room temperature. b) Authentic PI spectrum of acetaldehyde (blue line) recorded by Welz et al.<sup>21</sup> compared to the experimental  $m/z = 44$  spectrum (red open circles) at room temperature.

Figure 3 a) shows the experimental  $m/z = 106$  spectrum compared to an absolute PI curve of benzaldehyde, with an experimental onset of  $9.48 \pm 0.05$  eV that is consistent with the literature value of  $9.49 \pm 0.01$  eV.<sup>40</sup> The experimental  $m/z = 120$  spectrum shown in Figure 3 b) is compared with the absolute PI curve of phenylacetaldehyde. The experimental onset for  $m/z = 120$  is found at  $8.82 \pm 0.05$  eV, which agrees very well with the literature ionization energy value of  $8.80 \pm 0.01$  eV<sup>43</sup> for phenylacetaldehyde.

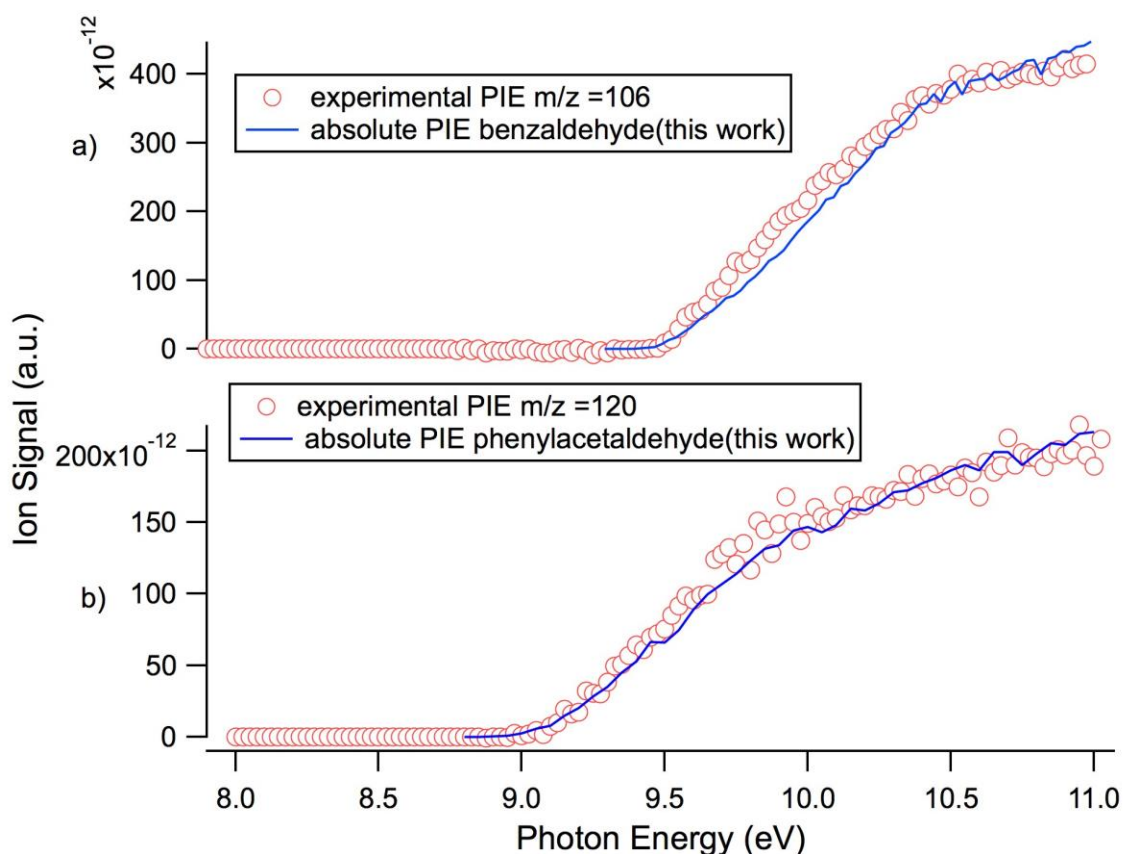


**Figure 3.** a) Absolute PI spectrum of benzaldehyde (blue line) taken in this experiment compared to the experimental  $m/z = 106$  spectrum (red open circles) at room temperature. b) Absolute PI spectrum of phenylacetaldehyde (blue line) taken in this experiment compared to the experimental  $m/z = 120$  spectrum (red open circles) at room temperature.

Products  $m/z = 30, 44, 106,$  and  $120$  are all forming at similar rates with an estimated pseudo first order rate constant of  $380\text{-}410\text{ s}^{-1}$  from the kinetic fitting presented in Figure 4 a). These species form fast and can be compared with the fitted rate constant for the parent  $m/z = 122$  depletion of  $970\text{ s}^{-1}$  and are characterized as primary chemistry with the exception of  $m/z = 44$  (see Proposed Mechanism section). Other secondary products identified in the oxidation reaction with 2PE based on their kinetic traces, Figure 4 b), are  $m/z = 78$  as benzene, and  $m/z = 92$  as a combination of toluene and 1,6 heptydne.  $m/z = 78$  time trace is fitted with a rate

constant of  $260 \text{ s}^{-1}$  and  $m/z = 92$  with a rate constant of  $160 \text{ s}^{-1}$ . Secondary products are not further investigated in this work since our focus is the characterization of primary chemistry species.

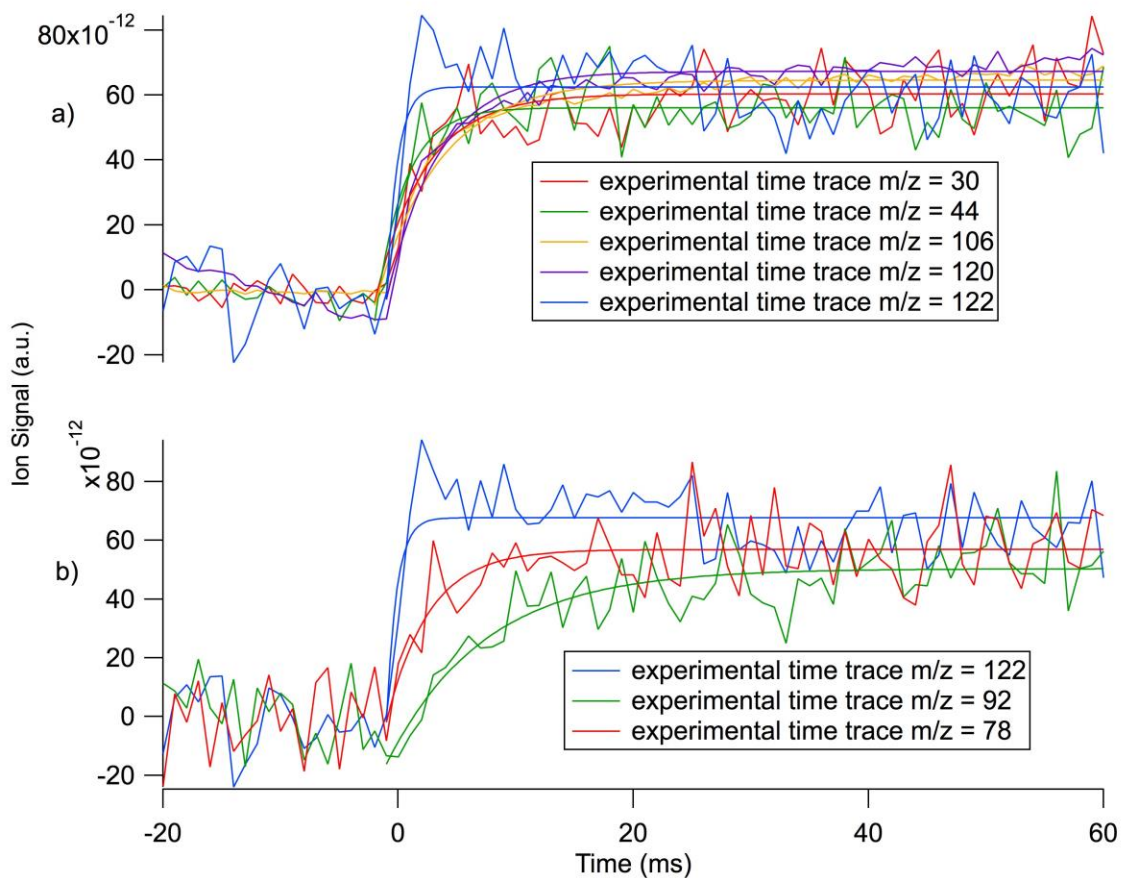


**Figure 4.** **a)** Comparison of experimental time traces  $m/z = 30, 44, 106, 120,$  and  $122$  during H abstraction by Cl and oxygen addition at room temperature. **b)** Comparison of experimental time traces  $m/z = 78, 92,$  and  $122$  during H abstraction by Cl and oxygen addition at room temperature. Signal for the reactant  $m/z = 122$  is inverted (multiplied by -1) for comparison against products.

## Product Identification 2PE + Cl + O<sub>2</sub> at 550 K

Several species seen in the room temperature reactions were not observed at a higher temperature. The following masses are observed and characterized during the oxidation reaction of 2PE at 550 K:  $m/z = 104$  and 120. Chlorinated species  $m/z = 140/142$  and  $156/158$  are generated at 550 K from chlorine addition to primary products, but are not characterized since they are formed through secondary chemistry. Figure 5 a) shows the experimental  $m/z = 104$  spectrum compared to the absolute PI curve of styrene with an observed photoionization onset of  $8.45 \pm 0.05$  eV, which matches well with the value of  $8.43 \pm 0.01$  eV<sup>44</sup> reported in the literature.

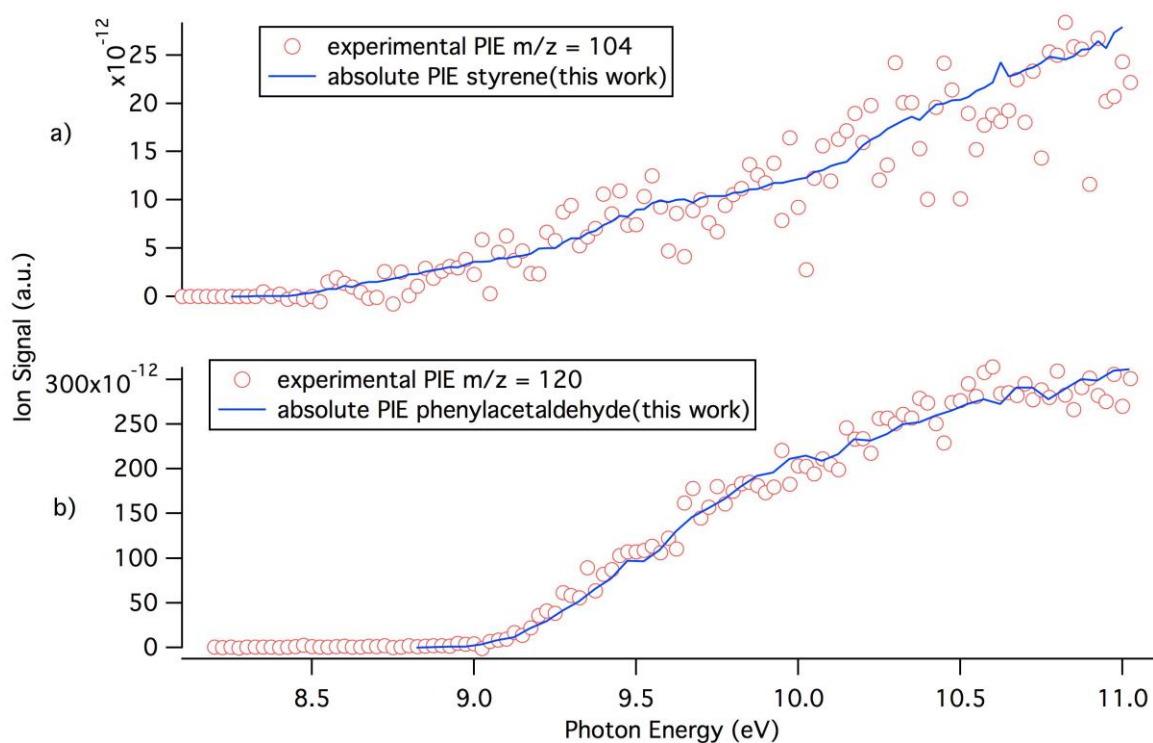


**Figure 5.** **a)** Absolute PI spectrum of styrene (blue line) taken in this experiment compared to the experimental  $m/z = 104$  spectrum (red open circles) at 550 K. **b)** Absolute PI spectrum of phenylacetaldehyde (blue line) taken in this experiment compared to the experimental  $m/z = 120$  spectrum (red open circles) at 550 K.

Figure 5 b) shows the experimental  $m/z = 120$  spectrum with an onset of  $8.83 \pm 0.05$  eV, which matches well with the literature onset of phenylacetaldehyde at  $8.80 \pm 0.01$  eV.<sup>43</sup>  $m/z = 120$  is characterized as primary chemistry product since its rate of formation with an estimated rate constant of  $670 \text{ s}^{-1}$  is the same as the depletion of the parent  $m/z = 122$  seen in Figure 6.  $m/z = 104$  time trace is fitted with a rate constant of  $290 \text{ s}^{-1}$  slower than the other product and the PES computation calculations show that the product cannot be formed via primary reactions (see Proposed Mechanism section).

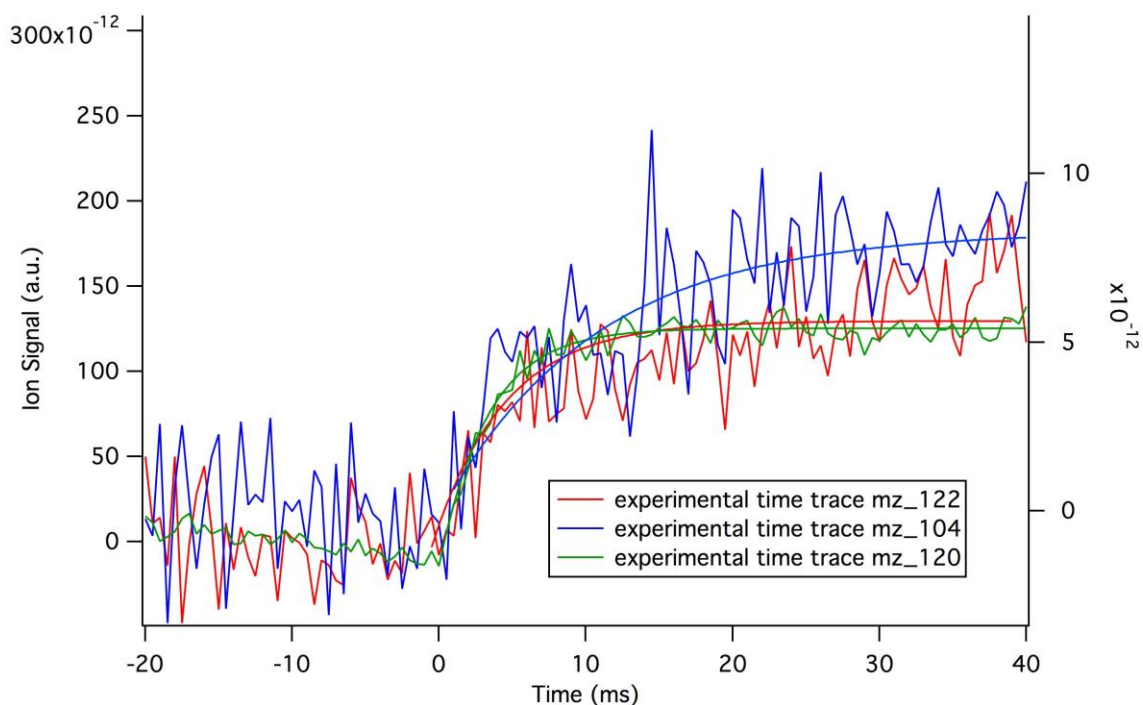


**Figure 6.** Comparison of experimental time traces  $m/z = 104, 120, 122$  during H abstraction by Cl and oxygen addition at 550 K. Signal for the reactant  $m/z = 122$  is inverted (multiplied by -1) for comparison against products.

#### 4.4 Proposed Mechanism:

On the ethanol group in 2PE, there are three potential sites for Cl to abstract a hydrogen and form three different radicals. These radicals  $\alpha$ -2-phenylethanyl ( $\alpha$ -2PE),  $\beta$ -2-phenylethanyl ( $\beta$ -2PE), and 2-phenylethoxy (2PEO) have calculated reaction enthalpies of -60.7, -37.4, and 1.4 kJ/mol, respectively, which are listed in Figure 7.

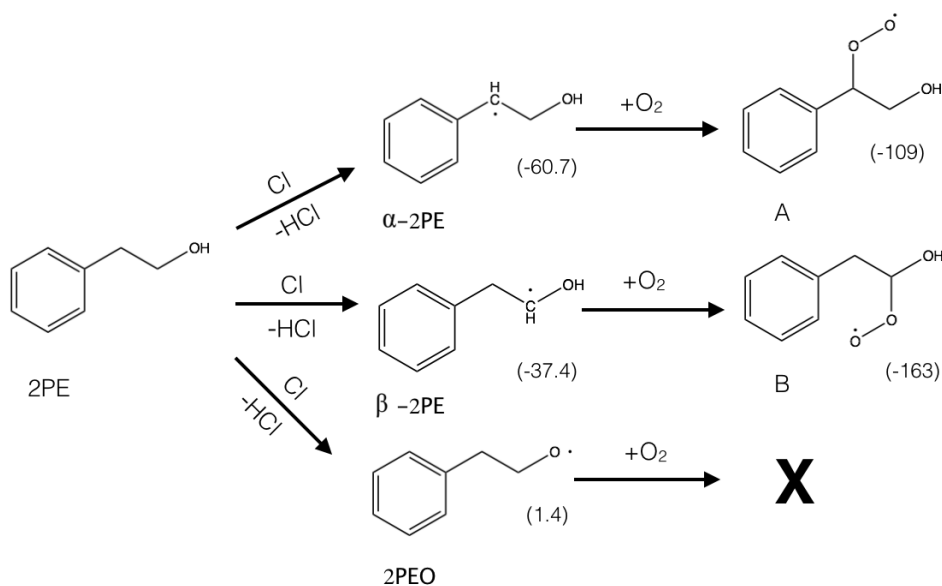


**Figure 7.** Reaction scheme for the initial steps of 2PE oxidation. Numbers in parentheses correspond to reaction enthalpies in kJ/mol.

After the addition of oxygen, only the  $\alpha$  and  $\beta$  radicals react to form the 2-phenylethanylperoxy species  $\alpha$ -ROO and  $\beta$ -ROO seen in Figure 10. The CBS-QB3 calculated reaction enthalpies of the  $\alpha$  and  $\beta$  peroxy species are -109 and -163 kJ/mol, respectively. Both phenylethanylperoxy radicals undergo intramolecular hydrogen abstraction, but the phenylethanylhydroperoxy radical (QOOH) is only formed during the  $\alpha$ -ROO pathway.



**$\beta$ -2PE reaction pathway:** When Cl abstracts a beta hydrogen from the ethanol group in 2PE,  $\beta$ -2PE is formed along with HCl.  $\beta$ -2PE then undergoes unimolecular decomposition seen in Figure 8, to form ethenol, a phenyl radical, and HCl with a calculated activation enthalpy of 77 kJ/mol and reaction enthalpy of 72 kJ/mol.

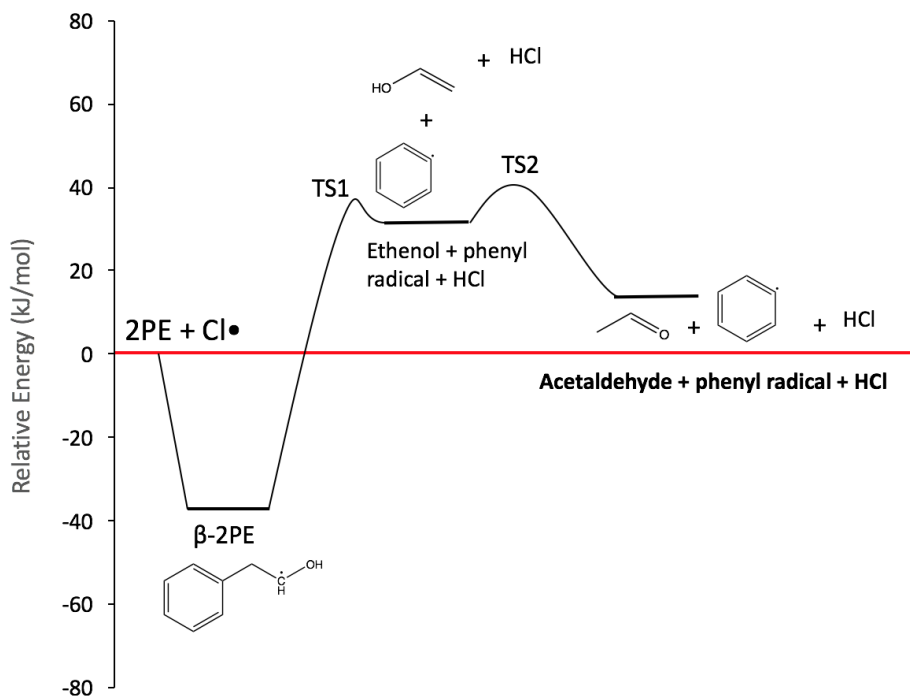


**Figure 8.** Diagram of potential energy surface scan of the 2PE reaction pathway for species  $\beta$ -2PE calculated using the CBS-QB3 composite model.

Ethenol then undergoes an intramolecular hydrogen transfer, and isomerizes to acetaldehyde with a calculated activation enthalpy of 11 kJ/mol and reaction enthalpy of -23 kJ/mol. This reaction pathway shows that acetaldehyde cannot be considered a primary chemistry product because its formation is thermodynamically and kinetically hindered by its endothermicity and high activation barrier above the zero-reference energy red line for energetics calculations (calculated from the optimized structures of our initial reactants  $\beta$ -2PE + O<sub>2</sub>).  $\beta$ -2PE then reacts

with O<sub>2</sub> to generate peroxy species B, which is formed exothermically with a calculated enthalpy of -163 kJ/mol. The reaction pathway for the β-ROO radical is illustrated by Figure 9.

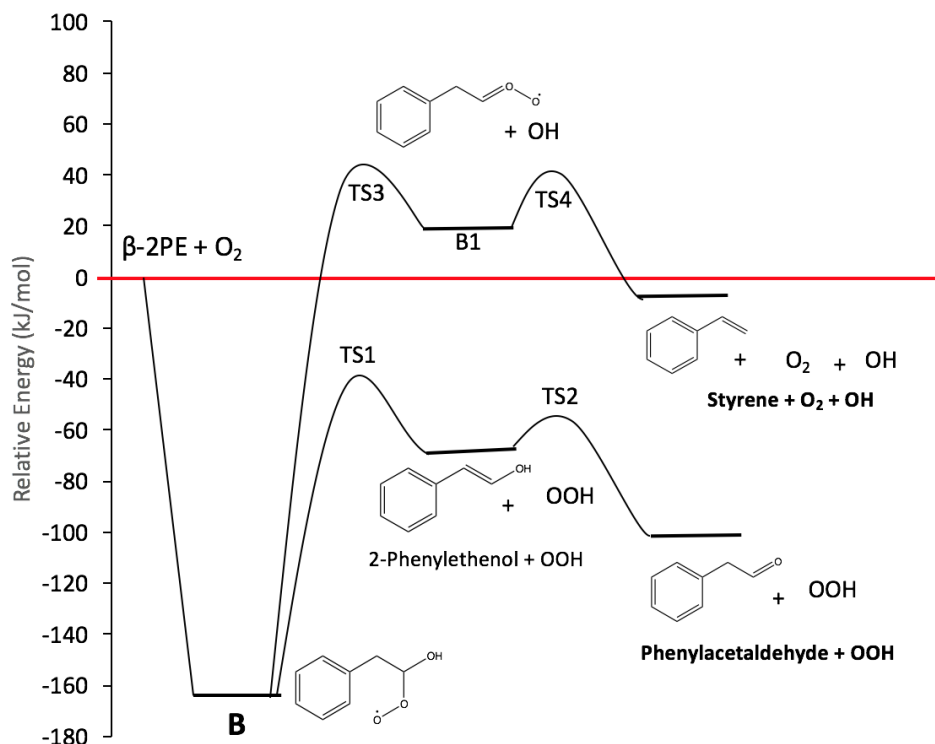


**Figure 9.** Diagram of potential energy surface scan of the 2PE oxidation pathway for species B calculated using the CBS-QB3 composite model.

This peroxy radical (B) then undergoes an intramolecular hydrogen abstraction, and isomerizes to 2-phenylethenol and OOH with a calculated activation enthalpy of 122 kJ/mol and reaction enthalpy of 91 kJ/mol. Phenylacetaldehyde is then formed through a hydrogen transfer to the beta carbon, which forms the C=O bond, and has a calculated activation enthalpy and reaction enthalpy of 19 and -31 kJ/mol, respectively. The species B also undergoes a unimolecular decomposition through the removal of a hydroxyl group to form the B1 and OH (Figure 9), and has a calculated activation enthalpy of 204 kJ/mol and reaction enthalpy of 179 kJ/mol, respectively. B1 is a Criegee intermediate, phenylacetaldehyde oxide, which undergoes a

decomposition to form styrene and O<sub>2</sub> with a calculated activation enthalpy of 22 kJ/mol and reaction enthalpy of -27 kJ/mol. According to the presented calculations, the products styrene and acetaldehyde are most likely generated through secondary chemistry since they have transition states and reaction products forming above the zero-reference energy level, making their pathways kinetically unfavorable. Of course, solely based on our computations we cannot rule out the possibility of lower energy pathways yielding the formation of these species.

**$\alpha$ -2PE reaction pathway:**  $\alpha$ -2PE is formed when Cl abstracts an alpha hydrogen from 2PE. After oxygen is added, peroxy species A is formed exothermically with a calculated enthalpy of -109 kJ/mol. The reaction pathway for species A is seen in Figure 10, where again the red line indicates the zero point reference energy for energetics calculations of the primary products, calculated from the optimized structures of our initial reactants  $\alpha$ -2PE + O<sub>2</sub>.

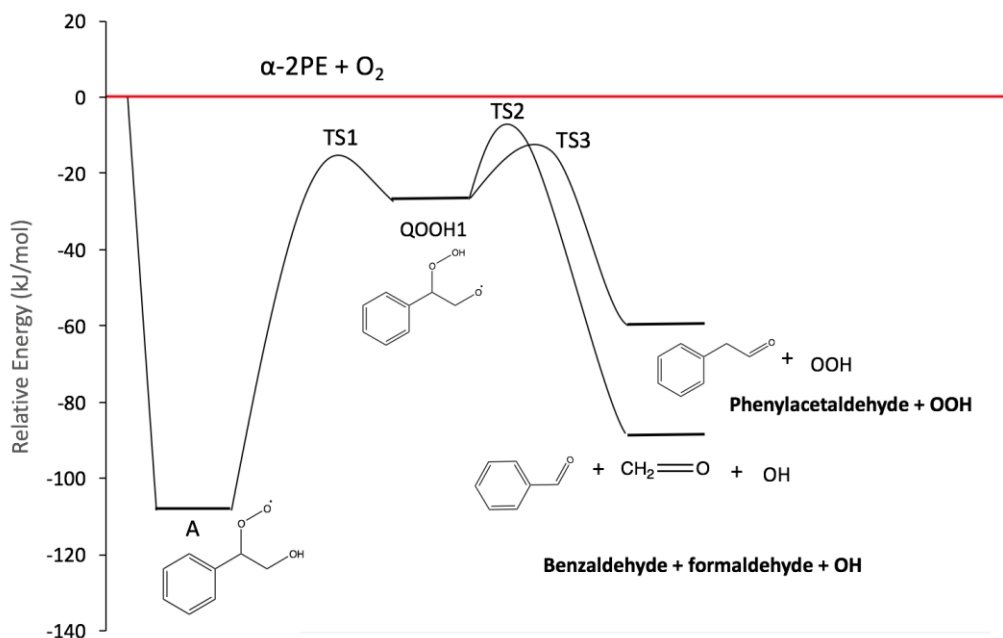


**Figure 10.** Diagram of potential energy surface scan of the 2PE oxidation pathway for species A calculated at the CBS-QB3 level of theory.

This  $\alpha$ -ROO radical undergoes an intramolecular hydrogen abstraction with the hydrogen on the hydroxyl group to form the  $\alpha$ -QOOH radical, and have a calculated activation enthalpy of 90 kJ/mol and reaction enthalpy of 79 kJ/mol. The  $\alpha$ -QOOH radical then undergoes unimolecular decomposition through the removal of a hydroxyl group, forming the products benzaldehyde, formaldehyde, and OH. This reaction has a calculated activation enthalpy of 25 kJ/mol and reaction enthalpy of -58 kJ/mol. The  $\alpha$ -QOOH radical also decomposes to phenylacetaldehyde and OOH through unimolecular decomposition via hydrogen transfer, which has a calculated activation enthalpy of 19 kJ/mol and reaction enthalpy of -36 kJ/mol.

#### 4.5 Branching fractions:

Branching fractions at 298 and 550 K are listed in Table 1.

**Table 1.** Branching fractions for products observed in the 2PE + Cl + O<sub>2</sub> reaction at 298 and 550 K.

Compound	m/z	298 K	550 K
Formaldehyde	30	27 ± 7.2	-
Benzaldehyde	106	24 ± 7.0	-
Phenylacetaldehyde	120	25 ± 6.4	60 ± 19

Absolute photoionization cross sections for formaldehyde ( $m/z = 30$ )<sup>41</sup> of  $9.2 \pm 1.4$  Mb and benzaldehyde ( $m/z = 106$ )<sup>45</sup> of  $45.6 \pm 6.84$  Mb are obtained from the literature. The absolute photoionization cross section for phenylacetaldehyde is obtained from this experiment and

calculated using the cross section of the calibrant propene<sup>39</sup> as a reference. Branching fraction uncertainties are calculated using the propagation of errors of the quantities from equation 2. Uncertainties for ion signal intensities are estimated by taking the difference between the measured upper signal value at 11 eV of that observed species and its literature reference. This method is also applied to the lower ion signal at 11 eV, then the average of these two values is used. Uncertainties of the mass discrimination factors are 13% as described in Savee et al<sup>46</sup>. The formation of benzaldehyde and formaldehyde are observed through unimolecular decomposition of the  $\alpha$ -QOOH radical, and have branching fractions of  $24 \pm 4.5 \%$  and  $27 \pm 6.5 \%$ , respectively. The main product phenylacetaldehyde ( $m/z = 120$ ) comes from the decomposition of the  $\beta$ -ROO radical and has a branching fraction of  $25 \pm 5.8 \%$  at room temperature and  $60 \pm 14 \%$  at 550 K. Branching fractions in this investigation only total to about 60 – 75 % due to chlorination of products from secondary reactions. Chlorinated products at  $m/z = 126/128$ ,  $140/142$ , and  $156/158$  have reaction rates similar to that of primary products since their time traces match well with the depletion of the reactant, and are being formed from Cl addition to product species  $m/z = 104$ ,  $106$ ,  $120$ , and parent  $m/z = 122$ .

## 4.6 Conclusions

In this study, the chlorine initiated oxidation of 2PE is investigated at 298 and 550 K. The  $2PE + Cl + O_2$  reaction was carried out at Lawrence Berkeley National Laboratory using synchrotron radiation coupled with a multiplexed photoionization mass spectrometer. Reaction products are identified based on photoionization spectra, kinetic time traces, ionization energies, and mass-to-charge ratios. Reaction mechanisms are calculated from potential energy surface

scans, using the CBS-QB3 composite method. Relative quantification of products was performed using absolute photoionization spectra via the determination of their branching fractions for both temperatures (298 and 550 K). Total branching fractions as the fraction of the total of what is detected for 2PE + Cl + O<sub>2</sub> at room temperature are  $76 \pm 21$  % and  $60 \pm 19$  % at 550 K. At both temperatures, the most abundant product is phenylacetaldehyde. We are not seeing total branching fractions reach 100 % due to chlorination from secondary reactions with primary products.

### **Acknowledgments**

This work is supported by American Chemical Society – Petroleum Research Fund Grant # 56067-UR6 and the University of San Francisco via the Faculty Development Fund. The authors would also like to acknowledge Drs. Taatjes and Osborn from Sandia National Laboratories for the use of the experimental apparatus. The Advanced Light Source is supported by the Director, Office of Science, Office of Basic Energy Sciences, of the U.S. Department of Energy under Contract No. DE-AC02-05CH11231.

## 4.7 References:

1. Atsumi, S.; Hanai, T.; Liao, J. C., Non-fermentative pathways for synthesis of branched-chain higher alcohols as biofuels. *Nature (London, U. K.)* **2008**, *451* (7174), 86-89.
2. Hill, J.; Nelson, E.; Tilman, D.; Polasky, S.; Tiffany, D., Environmental, economic, and energetic costs and benefits of biodiesel and ethanol biofuels. *Proc. Natl. Acad. Sci. U. S. A.* **2006**, *103* (30), 11206-11210.
3. Kohse-Hoeinghaus, K.; Osswald, P.; Cool, T. A.; Kasper, T.; Hansen, N.; Qi, F.; Westbrook, C. K.; Westmoreland, P. R., Biofuel Combustion Chemistry: from Ethanol to Biodiesel. *Angew. Chem., Int. Ed.* **2010**, *49* (21), 3572-3597.
4. Vispute, T. P.; Huber, G. W., Breaking the chemical and engineering barriers to lignocellulosic biofuels. *Int. Sugar J.* **2008**, *110* (1311), 138, 140, 142, 146, 148-149.
5. Escobar, J. C.; Lora, E. S.; Venturini, O. J.; Yanez, E. E.; Castillo, E. F.; Almazan, O., Biofuels: Environment, technology and food security. *Renewable Sustainable Energy Rev.* **2009**, *13* (6-7), 1275-1287.
6. Alternative Energy: Why Biofuels?  
<http://www.bp.com/sectiongenericarticle.do?categoryId=9030039&contentId=7055156>.
7. Renewable Fuel Standard (RFS). <http://www.epa.gov/otaq/fuels/renewablefuels/>.
8. Agarwal, A. K., Biofuels (alcohols and biodiesel) applications as fuels for internal combustion engines. *Progress in Energy and Combustion Science* **2007**, *33* (3), 233-271.
9. Rodriguez, G. M.; Atsumi, S., Synthetic Biology Approaches to Produce C3-C6 Alcohols from Microorganisms. *Current Chemical Biology* **2012**, *6* (1), 10.
10. Fortman, J. L.; Chhabra, S.; Mukhopadhyay, A.; Chou, H.; Lee, T. S.; Steen, E.; Keasling, J. D., Biofuel alternatives to ethanol: pumping the microbial well. *Trends Biotechnol.* **2008**, *26* (7), 375-381.
11. Kikuchi, R.; Gerardo, R.; Santos, S. M., Energy lifecycle assessment and environmental impacts of ethanol biofuel. *International Journal of Energy Research* **2009**, *33* (2), 186-193.
12. Ma, P.; Zhang, P.; Shu, J.; Yang, B.; Zhang, H., Characterization of secondary organic aerosol from photo-oxidation of gasoline exhaust and specific sources of major components. *Environ. Pollut. (Oxford, U. K.)* **2018**, *232*, 65-72.
13. Gibilisco, R. G.; Barnes, I.; Wiesen, P., Gas-phase oxidation of aromatic hydrocarbons: A kinetic study of the OH reaction with methoxybenzenes at atmospheric conditions. *Chem. Phys. Lett.* **2018**, *705*, 38-43.
14. Monod, A.; Poulain, L.; Grubert, S.; Voisin, D.; Wortham, H., Kinetics of OH-initiated oxidation of oxygenated organic compounds in the aqueous phase: new rate constants, structure-activity relationships and atmospheric implications. *Atmos. Environ.* **2005**, *39* (40), 7667-7688.
15. Nimlos, M. R.; Wolfrum, E. J.; Brewer, M. L.; Fennell, J. A.; Bintner, G., Gas-Phase Heterogeneous Photocatalytic Oxidation of Ethanol: Pathways and Kinetic Modeling. *Environ. Sci. Technol.* **1996**, *30* (10), 3102-3110.
16. Marinov, N. M., A detailed chemical kinetic model for high temperature ethanol oxidation. *Int. J. Chem. Kinet.* **1999**, *31* (3), 183-220.
17. Lyulyukin, M. N.; Besov, A. S.; Vorontsov, A. V., Oxidation of Ethanol Vapors in Negative Atmospheric Corona Discharge. *Ind. Eng. Chem. Res.* **2013**, *52* (17), 5842-5848.
18. Bott, J. F.; Cohen, N., A shock tube study of the reactions of the hydroxyl radical with several combustion species. *Int. J. Chem. Kinet.* **1991**, *23* (12), 1075-94.
19. Jimenez, E.; Gilles, M. K.; Ravishankara, A. R., Kinetics of the reactions of the hydroxyl radical with CH<sub>3</sub>OH and C<sub>2</sub>H<sub>5</sub>OH between 235 and 360 K. *J. Photochem. Photobiol., A* **2003**, *157* (2-3), 237-245.

20. Meier, U.; Grotheer, H. H.; Riekert, G.; Just, T., Study of hydroxyl reactions with methanol and ethanol by laser-induced fluorescence. *Ber. Bunsen-Ges. Phys. Chem.* **1985**, *89* (3), 325-7.
21. Welz, O.; Savee, J. D.; Eskola, A. J.; Sheps, L.; Osborn, D. L.; Taatjes, C. A., Low-temperature combustion chemistry of biofuels: Pathways in the low-temperature (550-700 K) oxidation chemistry of isobutanol and tert-butanol. *Proc. Combust. Inst.* **2013**, *34* (1), 493-500.
22. Emel'yanenko, V. N.; Dabrowska, A.; Hertel, M. O.; Scheuren, H.; Sommer, K., Vapor Pressures, Enthalpies of Vaporization, and Limiting Activity Coefficients in Water at 100 °C of 2-Furaldehyde, Benzaldehyde, Phenylethanal, and 2-Phenylethanol. *Journal of Chemical & Engineering Data* **2007**, *52* (2), 468-471.
23. Lin, Y. L.; Blaschek, H. P., Butanol production by a butanol-tolerant strain of *Clostridium acetobutylicum* in extruded corn broth. *Appl. Environ. Microbiol.* **1983**, *45* (3), 966-73.
24. Atsumi, S.; Cann, A. F.; Connor, M. R.; Shen, C. R.; Smith, K. M.; Brynildsen, M. P.; Chou, K. J. Y.; Hanai, T.; Liao, J. C., Metabolic engineering of *Escherichia coli* for 1-butanol production. *Metab. Eng.* **2008**, *10* (6), 305-311.
25. Keasling, J. D.; Chou, H., Metabolic engineering delivers next-generation biofuels. *Nat. Biotechnol.* **2008**, *26* (3), 298-299.
26. Fahlbusch, K.-G. H., Franz-Josef; Panten, Johannes; Pickenhagen, Wilhelm; Schatkowski, Dietmar; Bauer, Kurt; Garbe, Dorothea; Surburg, Horst, *Flavors and Fragrances*. 2003.
27. Etschmann, M. M. W.; Bluemke, W.; Sell, D.; Schrader, J., Biotechnological production of 2-phenylethanol. *Appl. Microbiol. Biotechnol.* **2002**, *59* (1), 1-8.
28. Czekner, J.; Taatjes, C. A.; Osborn, D. L.; Meloni, G., Absolute photoionization cross-sections of selected furanic and lactonic potential biofuels. *Int. J. Mass Spectrom.* **2013**, *348*, 39-46.
29. Winfough, M.; Yao, R.; Ng, M.; Catani, K.; Meloni, G., Synchrotron Photoionization Investigation of the Oxidation of Ethyl tert-Butyl Ether. *J. Phys. Chem. A* **2017**, *121* (7), 1460-1469.
30. Fathi, Y.; Meloni, G., Study of the Synchrotron Photoionization Oxidation of 2-Methylfuran Initiated by O(3P) under Low-Temperature Conditions at 550 and 650 K. *J. Phys. Chem. A* **2017**, *121* (37), 6966-6980.
31. IUPAC Subcommittee on Gas Kinetic Data Evaluation – Data Sheet PCI11. [http://www.iupac-kinetic.ch.cam.ac.uk/datasheets/xhtml/PCI11\\_cl2+hv.xhtml\\_mathml.xml](http://www.iupac-kinetic.ch.cam.ac.uk/datasheets/xhtml/PCI11_cl2+hv.xhtml_mathml.xml).
32. Maric, D.; Burrows, J. P.; Meller, R.; Moortgat, G. K., A study of the UV-visible absorption spectrum of molecular chlorine. *J. Photochem. Photobiol., A* **1993**, *70* (3), 205-14.
33. Taatjes, C. A.; Osborn, D. L.; Selby, T. M.; Meloni, G.; Trevitt, A. J.; Epifanovsky, E.; Krylov, A. I.; Sirjean, B.; Dames, E.; Wang, H., Products of the Benzene + O(3P) Reaction. *J. Phys. Chem. A* **2010**, *114* (9), 3355-3370.
34. Montgomery, J. A., Jr.; Frisch, M. J.; Ochterski, J. W.; Petersson, G. A., A complete basis set model chemistry. VI. Use of density functional geometries and frequencies. *J. Chem. Phys.* **1999**, *110* (6), 2822-2827.
35. Montgomery, J. A., Jr.; Frisch, M. J.; Ochterski, J. W.; Petersson, G. A., A complete basis set model chemistry. VII. Use of the minimum population localization method. *J. Chem. Phys.* **2000**, *112* (15), 6532-6542.
36. Frisch, M. J. T., G. W.; Schlegel, H. B.; Scuseria, G. E.; Robb, M. A.; Cheeseman, J. R.; Scalmani, G.; Barone, V.; Mennucci, B.; Petersson, G. A.; Nakatsuji, H.; Caricato, M.; Li, X.; Hratchian, H. P.; Izmaylov, A. F.; Bloino, J.; Zheng, G.; Sonnenberg, J. L.; Hada, M.; Ehara, M.; Toyota, K.; Fukuda, R.; Hasegawa, J.; Ishida, M.; Nakajima, T.; Honda, Y.; Kitao, O.; Nakai, H.; Vreven, T.; Montgomery, J. A., Jr.; Peralta, J. E.; Ogliaro, F.; Bearpark, M.; Heyd, J. J.; Brothers, E.; Kudin, K. N.; Staroverov, V. N.; Kobayashi, R.; Normand, J.; Raghavachari, K.; Rendell, A.; Burant, J. C.; Iyengar, S. S.; Tomasi, J.; Cossi, M.; Rega, N.; Millam, N. J.; Klene, M.; Knox, J. E.; Cross, J. B.; Bakken, V.; Adamo, C.; Jaramillo, J.; Gomperts, R.; Stratmann, R. E.; Yazyev, O.; Austin, A. J.; Cammi, R.; Pomelli, C.; Ochterski, J. W.; Martin, R. L.;



- Morokuma, K.; Zakrzewski, V. G.; Voth, G. A.; Salvador, P.; Dannenberg, J. J.; Dapprich, S.; Daniels, A. D.; Farkas, Ö.; Foresman, J. B.; Ortiz, J. V.; Cioslowski, J.; Fox, D. J. *Gaussian 09, Revision A.1*, Gaussian, Inc.: Wallingford, CT, 2009.
37. Dennington, R. K., T.; Millam, J *GaussView, 5*, SemiChem Inc: Shawnee Mission KS, 2009.
  38. Tirado-Rives, J.; Jorgensen, W. L., Performance of B3LYP Density Functional Methods for a Large Set of Organic Molecules. *J. Chem. Theory Comput.* **2008**, *4* (2), 297-306.
  39. Cool, T. A.; Nakajima, K.; Mostefaoui, T. A.; Qi, F.; McIlroy, A.; Westmoreland, P. R.; Law, M. E.; Poisson, L.; Peterka, D. S.; Ahmed, M., Selective detection of isomers with photoionization mass spectrometry for studies of hydrocarbon flame chemistry. *J. Chem. Phys.* **2003**, *119* (16), 8356-8365.
  40. McLoughlin, R. G.; Traeger, J. C., A photoionization study of some benzoyl compounds. Thermochemistry of [C<sub>7</sub>H<sub>5</sub>O]<sup>+</sup> formation. *Org. Mass Spectrom.* **1979**, *14* (8), 434-8.
  41. Cooper, G.; Anderson, J. E.; Brion, C. E., Absolute photoabsorption and photoionization of formaldehyde in the VUV and soft x-ray regions (3-200 eV). *Chem. Phys.* **1996**, *209* (1), 61-77.
  42. Jochims, H. W.; Lohr, W.; Baumgaertel, H., Photoionization mass spectrometry studies of deuterated acetaldehydes CH<sub>3</sub>CDO and CD<sub>3</sub>CHO. *Chem. Phys. Lett.* **1978**, *54* (3), 594-6.
  43. Rabalais, J. W.; Colton, R. I., Electronic interaction between the phenyl group and its unsaturated substituents. *J. Electron Spectrosc. Relat. Phenomena* **1972**, *1* (1), 83-99.
  44. Fu, E. W.; Dunbar, R. C., Photodissociation spectroscopy and structural rearrangements in ions of cyclooctatetraene, styrene, and related molecules. *J. Am. Chem. Soc.* **1978**, *100* (8), 2283-8.
  45. Zhou, Z.; Xie, M.; Wang, Z.; Qi, F., Determination of absolute photoionization cross-sections of aromatics and aromatic derivatives. *Rapid Commun. Mass Spectrom.* **2009**, *23* (24), 3994-4002.
  46. Savee, J. D.; Soorkia, S.; Welz, O.; Selby, T. M.; Taatjes, C. A.; Osborn, D. L., Absolute photoionization cross-section of the propargyl radical. *J. Chem. Phys.* **2012**, *136* (13), 134307/1-134307/10.

## 4.8 Supporting Information for Publication:

Contents of the supporting information includes the Cartesian coordinates of all structures calculated in the potential energy surface.

PES optimized structures (Cartesian coordinates) using the CBS-QB3 composite model:

### 1) beta 2PE

C	2.77865100	-0.22684100	-0.25784900
C	1.94348700	-1.31538800	-0.00788700
C	0.59566900	-1.11268200	0.27359900
C	0.05733000	0.17887600	0.31377000
C	0.90364300	1.26048600	0.05989900
C	2.25470200	1.06225100	-0.22356700
H	3.82906700	-0.38392900	-0.47602700
H	2.34404600	-2.32305200	-0.03005100
H	-0.05162900	-1.96234700	0.46444000
H	0.50192000	2.26847900	0.08695900
H	2.89582000	1.91547800	-0.41630700
C	-1.41267900	0.38786400	0.61269900
H	-1.68531700	-0.11700900	1.54861200
H	-1.60301100	1.45938800	0.78806900
C	-2.29262600	-0.13261600	-0.47367500
H	-2.02255100	0.01588100	-1.51728600
O	-3.63068900	-0.13385100	-0.16206400

H -4.13189600 -0.41378400 -0.93382400

## 2) 2PE

C -2.82123900 -0.00028700 -0.30238500

C -2.14046100 1.20346200 -0.13336900

C -0.78816300 1.20092200 0.20077200

C -0.09070800 0.00029200 0.37321600

C -0.78779400 -1.20067700 0.20112600

C -2.14004500 -1.20379800 -0.13300100

H -3.87464100 -0.00049700 -0.55895800

H -2.66353500 2.14547000 -0.25676900

H -0.26690500 2.14331700 0.33799100

H -0.26612900 -2.14280500 0.33862800

H -2.66283100 -2.14600400 -0.25610500

C 1.38515800 0.00050600 0.69816600

H 1.64650600 0.88061300 1.29263000

H 1.64654900 -0.87891000 1.29362300

C 2.25868500 -0.00029100 -0.55588700

H 2.03007100 0.88697800 -1.16322600

H 2.03004200 -0.88837900 -1.16204800

O 3.61888000 0.00002600 -0.13055600

H 4.17722900 -0.00077100 -0.91314900

## 3) HCl

Cl	0.00000000	0.00000000	0.07125900
H	0.00000000	0.00000000	-1.21139900

#### 4) TS1

C	-2.82344400	0.55710000	-0.09566800
C	-1.75013600	1.43547600	0.05550800
C	-0.44581800	0.93808300	0.16414800
C	-0.27126100	-0.42982300	0.12181600
C	-1.30631200	-1.33005000	-0.02804600
C	-2.60642500	-0.81997000	-0.13793000
H	-3.83183700	0.94667000	-0.18055300
H	-1.92497500	2.50638300	0.08920300
H	0.39923900	1.60919200	0.27991900
H	-1.13432100	-2.40169300	-0.05798900
H	-3.44498600	-1.49930100	-0.25586000
C	2.07508100	-1.14075100	0.34831600
H	1.94170000	-0.95912500	1.40601600
H	1.83522200	-2.12031200	-0.03838700
C	2.77867300	-0.28466500	-0.41148500
H	2.99838700	-0.48372100	-1.45632900
O	3.18137100	0.92854000	0.07241700
H	3.62547300	1.41846500	-0.62464700

#### 5) ethenol

C	-1.22575200	-0.17904900	0.00018000
H	-1.31623300	-1.25799100	0.00011200
H	-2.12643600	0.41850700	0.00037100
C	-0.03606200	0.41128500	0.00003900
H	0.06410900	1.49437200	0.00010600
O	1.13440600	-0.29559300	-0.00020100
H	1.87419900	0.31643800	-0.00029500

#### 6) phenyl radical

C	-0.00012000	1.32192900	0.00014000
C	-1.21196200	0.63129000	0.00011800
C	-1.22366000	-0.77070700	-0.00003000
C	0.00018500	-1.39606100	-0.00014800
C	1.22379800	-0.77057100	-0.00013300
C	1.21178100	0.63159700	0.00001500
H	-0.00031800	2.40595900	0.00025400
H	-2.15039800	1.17599000	0.00021500
H	-2.15741700	-1.32190800	-0.00004900
H	2.15783900	-1.32129100	-0.00023100
H	2.15016200	1.17639000	0.00003300

### 7) TS2

C	-1.03636900	-0.18623000	-0.00004200
H	-1.02069100	-1.28226000	0.00037100
H	-2.05556800	0.18996200	-0.00019500
C	0.04642800	0.58930600	0.00009000
H	0.15456400	1.66659000	-0.00003900
O	1.08697000	-0.27167500	-0.00003100
H	0.16558000	-0.81935000	-0.00017400

### 8) acetaldehyde

C	1.16874500	-0.14760200	0.00009600
H	1.70800300	0.22235600	-0.87870500
H	1.70744800	0.22174700	0.87950000
C	-0.23564800	0.39721800	-0.00013300
H	-0.30501700	1.50883200	0.00028100
O	-1.23305000	-0.27660900	-0.00007500
H	1.15538300	-1.23775900	-0.00025900

**Figure 9** PES optimized structures (Cartesian coordinates) using the CBS-QB3 composite model:

**1) beta-2PE**

C	2.77865100	-0.22684100	-0.25784900
C	1.94348700	-1.31538800	-0.00788700
C	0.59566900	-1.11268200	0.27359900
C	0.05733000	0.17887600	0.31377000
C	0.90364300	1.26048600	0.05989900
C	2.25470200	1.06225100	-0.22356700
H	3.82906700	-0.38392900	-0.47602700
H	2.34404600	-2.32305200	-0.03005100
H	-0.05162900	-1.96234700	0.46444000
H	0.50192000	2.26847900	0.08695900
H	2.89582000	1.91547800	-0.41630700
C	-1.41267900	0.38786400	0.61269900
H	-1.68531700	-0.11700900	1.54861200
H	-1.60301100	1.45938800	0.78806900
C	-2.29262600	-0.13261600	-0.47367500
H	-2.02255100	0.01588100	-1.51728600
O	-3.63068900	-0.13385100	-0.16206400

H -4.13189600 -0.41378400 -0.93382400

## 2) O<sub>2</sub>

O 0.00000000 0.00000000 0.60283800

O 0.00000000 0.00000000 -0.60283800

## 3) Species B (beta2PE o2 addition)

C 3.26442900 0.43731500 0.35925700

C 2.43661000 1.28418300 -0.37508800

C 1.16669300 0.86262100 -0.75989400

C 0.70416200 -0.41245300 -0.41856600

C 1.54437100 -1.25407600 0.31714400

C 2.81478300 -0.83448200 0.70535700

H 4.25398200 0.76549200 0.65657800

H 2.78024500 2.27514600 -0.64992800

H 0.52511800 1.52952900 -1.32468300

H 1.20467200 -2.25081000 0.58154900

H 3.45391800 -1.50276700 1.27155500

C -0.67916300 -0.87458500 -0.82240900

H -0.96184700 -0.47673900 -1.80072700

H -0.70975400 -1.96424100 -0.89659400

C -1.77153900 -0.48416900 0.15758200

H -1.50182500 -0.68161400 1.20133500

O -2.96565600 -1.06437000 -0.20853600



H	-3.64034700	-0.73186600	0.39851100
O	-1.89692200	1.00323900	0.09228200
O	-2.92320100	1.39759900	0.81401800

#### 4) species B1

C	-3.01374300	0.62566800	-0.31810100
C	-2.00797300	1.46984400	0.15046400
C	-0.75748200	0.95328700	0.47595900
C	-0.49854700	-0.41508800	0.34212800
C	-1.50991900	-1.25311100	-0.13121400
C	-2.76235600	-0.73653500	-0.45841300
H	-3.98757800	1.02842000	-0.57172700
H	-2.19706300	2.53138200	0.26201400
H	0.02223900	1.61567300	0.83772700
H	-1.32097500	-2.31635700	-0.23866800
H	-3.54006900	-1.39911100	-0.82089600
C	0.87442600	-0.97011700	0.69897800
H	1.16633200	-0.68244000	1.71218500
H	0.84268000	-2.06521900	0.66196100
C	1.91984300	-0.48840200	-0.24466700
H	1.89922900	-0.66389400	-1.31849600
O	2.87922700	0.19655700	0.20425500
O	3.82698600	0.65822600	-0.65611800

#### 5) TS3 -(TS for B1)

C	-3.44210800	0.28923300	-0.37548000
C	-2.62257300	1.26222400	0.19419900
C	-1.32381000	0.94286300	0.57933600
C	-0.83187400	-0.35488800	0.40419400
C	-1.65734400	-1.32329500	-0.17094100
C	-2.95733000	-1.00359200	-0.55727700
H	-4.45368000	0.53788700	-0.67494100
H	-2.99430600	2.27004200	0.33912500
H	-0.69024700	1.70421400	1.02282000
H	-1.28569100	-2.33298600	-0.31089400
H	-3.59044800	-1.76537500	-0.99756900
C	0.59234700	-0.69135700	0.82353000
H	0.80232800	-0.36008500	1.84296500
H	0.74879400	-1.77439000	0.78233100
C	1.57812300	-0.06941600	-0.09739800
H	1.58692500	-0.24502000	-1.16731800
O	3.57773600	-1.48746700	-0.35839400
H	3.89584200	-0.55758400	-0.47306200
O	2.38413900	0.79214900	0.35963900
O	3.32560700	1.28231600	-0.53477700

## 6) OH

H	0.00000000	0.00000000	-0.86685200
O	0.00000000	0.00000000	0.10835700

## 7) TS4

C	-3.11373900	0.93587300	-0.21461500
C	-2.16071100	1.76343000	0.38316800
C	-0.87815700	1.29403900	0.61184000
C	-0.50152500	-0.02348200	0.24759200
C	-1.48892000	-0.84654400	-0.35114700
C	-2.76786300	-0.36892800	-0.57923500
H	-4.11756300	1.30243900	-0.39473800
H	-2.42336600	2.77604500	0.66701500
H	-0.13779000	1.93890500	1.07229500
H	-1.24363200	-1.86124000	-0.63914400
H	-3.50632400	-1.01270100	-1.04337900
C	0.83548700	-0.45401800	0.49895400
H	1.50600100	0.28087500	0.93343000
H	2.08259000	-2.11894000	0.90150500
C	1.40782200	-1.68937200	0.16169400
H	0.80888200	-2.43808400	-0.34425600
O	2.74138700	-1.53339900	-0.93879700
O	3.32053200	-0.39315200	-0.91084600

## 8) styrene

C	2.26141600	0.26117200	0.00001000
C	1.35978800	1.32693500	-0.00001400

C	-0.00854800	1.09037100	-0.00002500
C	-0.51405600	-0.22033300	-0.00001700
C	0.40608700	-1.27922000	0.00000700
C	1.77817500	-1.04408700	0.00002700
H	3.32900500	0.44951100	0.00001300
H	1.72800100	2.34697100	-0.00003200
H	-0.69101100	1.93221900	-0.00003000
H	0.03577400	-2.29942200	0.00001600
H	2.46838800	-1.88039300	0.00005400
C	-1.95325700	-0.52820100	-0.00004700
H	-2.18570700	-1.59103800	-0.00015400
C	-2.97217300	0.33479200	0.00004900
H	-3.99690700	-0.01639500	0.00001800
H	-2.83212300	1.40997200	0.00016600

**9) TS1**

C	-3.30949100	0.37019300	-0.21575900
C	-2.29364000	1.23301500	-0.62179800
C	-0.95862800	0.88839800	-0.42978100
C	-0.61447800	-0.33808100	0.15462600
C	-1.64302100	-1.19269600	0.56729400
C	-2.97810800	-0.84210000	0.38501600
H	-4.34859900	0.64331800	-0.35905600
H	-2.53975900	2.18558800	-1.07764800
H	-0.17858400	1.58404100	-0.71894600

H	-1.39532200	-2.14269100	1.02988600
H	-3.75991400	-1.51936700	0.71063500
C	0.81800600	-0.72246700	0.36078200
H	1.32429900	0.28174400	1.08177400
H	0.96846100	-1.59376700	1.00161500
C	1.71801900	-0.62654900	-0.71302600
H	1.48059600	-0.10890600	-1.63177400
O	2.84976000	-1.32663700	-0.81438300
H	3.02416800	-1.79766300	0.01070900
O	2.60292000	1.32480500	0.06927400
O	2.05587000	1.32968500	1.22982700

#### 10) 2-phenylethenol

C	-2.80370800	0.24889400	-0.04977400
C	-1.90984900	1.31759800	0.02268000
C	-0.54055800	1.09078700	0.08225600
C	-0.02047300	-0.21572700	0.05713700
C	-0.93559400	-1.27930100	-0.00540100
C	-2.30724100	-1.05186700	-0.05912100
H	-3.87168100	0.42950600	-0.09042300
H	-2.28368700	2.33552600	0.04396000
H	0.12944800	1.93894900	0.16559500
H	-0.56080900	-2.29781400	-0.01842500
H	-2.98890100	-1.89396700	-0.10872000
C	1.41553200	-0.51186700	0.10095100

H	1.67923300	-1.55142000	0.29177200
C	2.41072300	0.36197200	-0.09760500
H	2.24791100	1.40721300	-0.33069100
O	3.74097500	0.08891100	-0.05314300
H	3.86770000	-0.84222300	0.16534100

### 11) OOH

H	-0.88461600	-0.87070200	0.00000000
O	0.05528900	0.71855200	0.00000000
O	0.05528900	-0.60971400	0.00000000

### 12) TS2

C	2.82503800	0.24113500	-0.10595200
C	2.04215900	1.29136300	0.36836300
C	0.66924900	1.12158700	0.53327600
C	0.05351700	-0.09797600	0.22415200
C	0.85347600	-1.14582400	-0.24921700
C	2.22658200	-0.97839500	-0.41491000
H	3.89359000	0.37246400	-0.23491300
H	2.49960900	2.24494200	0.60842200
H	0.06138100	1.94072700	0.90134300
H	0.38930100	-2.09543800	-0.49159100
H	2.82828500	-1.80017500	-0.78750700
C	-1.41271500	-0.28329300	0.41591200

H	-1.75037000	-0.64582400	1.38731200
C	-2.31209200	-0.02821900	-0.53540300
H	-2.03092100	0.33366000	-1.51816000
O	-3.66252200	-0.17022500	-0.44189200
H	-3.88535900	-0.49230400	0.43955500

### 13) phenylacetaldehyde

C	-2.62655500	0.29036400	-0.31557100
C	-1.77238300	1.34736200	-0.00531200
C	-0.44842100	1.09738400	0.34370900
C	0.04175900	-0.21277100	0.39439400
C	-0.82295200	-1.26485700	0.07910600
C	-2.14814100	-1.01667200	-0.27330700
H	-3.65818600	0.48478600	-0.58588600
H	-2.13784800	2.36775200	-0.03412500
H	0.21241000	1.92444700	0.58211000
H	-0.46013100	-2.28700100	0.11876800
H	-2.80676700	-1.84495000	-0.50956000
C	1.49446000	-0.46619300	0.74200300
H	1.62360400	-1.50914400	1.05414200
C	2.39509400	-0.23257100	-0.46177300
H	2.12224000	-0.82646400	-1.36208700
O	3.32349700	0.53226500	-0.47929500
H	1.83952900	0.18018700	1.55149400

**Figure 10** PES optimized structures (Cartesian coordinates) using the CBS-QB3 composite model:

**1) alpha 2PE**

C	2.83993700	-0.27600100	0.01817200
C	1.92246000	-1.33100200	0.01345400
C	0.56001100	-1.08270100	-0.00166900
C	0.05566100	0.24950100	-0.01342000
C	1.01318200	1.30417600	-0.00850700
C	2.37066200	1.04309200	0.00709100
H	3.90466200	-0.47751600	0.03034100
H	2.27970300	-2.35514700	0.02201800
H	-0.13093000	-1.91782300	-0.00497900
H	0.65699100	2.32891400	-0.01705500
H	3.07620700	1.86679900	0.01074900
C	-1.32306400	0.54380000	-0.02950600
H	-1.64698300	1.57865600	-0.04950400
C	-2.41608700	-0.46892500	-0.05582500
H	-2.38522300	-1.03865400	-1.00214600
O	-3.65592000	0.21920200	0.08131600
H	-4.36447600	-0.42757200	0.02467500
H	-2.27916800	-1.20291400	0.75662000

**2) O<sub>2</sub>**

O	0.00000000	0.00000000	0.60283800
---	------------	------------	------------



O	0.00000000	0.00000000	-0.60283800
---	------------	------------	-------------

### 3) Species A-(O2 addition)

C	-3.30033200	0.08203400	0.16806000
C	-2.45989200	1.00687900	0.78483400
C	-1.08037300	0.91630800	0.62344000
C	-0.52748200	-0.09859200	-0.16530700
C	-1.37701900	-1.01554900	-0.78963000
C	-2.75637400	-0.93019600	-0.61922800
H	-4.37438800	0.15353000	0.29599100
H	-2.87892700	1.80120200	1.39192300
H	-0.43245700	1.64606300	1.09431000
H	-0.95750400	-1.79851300	-1.41273100
H	-3.40496200	-1.64802800	-1.10817200
C	0.96257600	-0.23615200	-0.31115000
H	1.22757500	-0.88909200	-1.14565400
C	1.67185000	-0.73371000	0.95628100
H	1.62000000	0.05710500	1.71964100
O	2.99288300	-1.16678300	0.72196300

H	3.44295100	-0.44705700	0.26020100
H	1.11584800	-1.59537400	1.33232600
O	1.46650000	1.11410600	-0.66744000
O	2.77113400	1.14943100	-0.84347600

#### 4) TS1

C	-3.30957800	0.13972200	0.14615600
C	-2.46063500	1.15572200	0.58300700
C	-1.08337100	1.03185800	0.43062000
C	-0.54425500	-0.10826600	-0.17613400
C	-1.40040600	-1.12198400	-0.61639900
C	-2.77730500	-1.00007100	-0.45269600
H	-4.38196600	0.23716100	0.27054700
H	-2.87207000	2.04564600	1.04517600
H	-0.42467400	1.82399800	0.76535800
H	-0.98827900	-2.00495700	-1.09358900
H	-3.43322600	-1.79040300	-0.79895400
C	0.93450100	-0.27344600	-0.33145300
H	1.21131900	-1.03681900	-1.06161000
C	1.64875100	-0.71533100	1.07198100
H	1.28583800	-0.00733800	1.83242100
O	2.98242000	-0.71760900	0.89583600
H	3.18175100	0.12139600	-0.11719900
H	1.23883900	-1.72181300	1.25207200
O	1.52994900	0.95140000	-0.67540200

O 2.87951700 0.72810700 -0.97161500

### 5) QOOH1

C 3.30036500 -0.12014200 0.16398500

C 2.44901300 -1.08620300 0.69689000

C 1.07126000 -0.97705800 0.52912200

C 0.53101800 0.10214300 -0.17859300

C 1.39127100 1.06084500 -0.72040700

C 2.76867400 0.95432700 -0.54577500

H 4.37290600 -0.20769500 0.29541700

H 2.85847800 -1.92910500 1.24210600

H 0.41102700 -1.73766400 0.92678200

H 0.98158800 1.89301300 -1.28374300

H 3.42561000 1.70455700 -0.97112400

C -0.96269300 0.25905700 -0.32114600

H -1.20234800 0.99447600 -1.10111500

C -1.65754600 0.73029300 0.97727300

H -1.57182200 -0.04141400 1.75948700

O -2.93333000 1.16155200 0.77441200

H -1.09726200 1.61803300 1.33007500

O -1.46135600 -1.03231200 -0.70594600

O -2.90056400 -1.03345600 -0.61413700

H -3.16434800 -0.60003000 -1.44062000

### 6) TS2

C	3.27270800	-0.08113200	0.15764300
C	2.44178300	-0.93203600	0.86966300
C	1.07143700	-0.87296300	0.69820600
C	0.51852900	0.03727100	-0.19943600
C	1.35829200	0.88549500	-0.91468500
C	2.72788400	0.82853000	-0.73451900
H	4.34614300	-0.12807200	0.29697800
H	2.86498800	-1.64634100	1.56570900
H	0.42241800	-1.54155000	1.24888300
H	0.93424800	1.59300200	-1.61867100
H	3.37300400	1.49262300	-1.29714600
C	-0.96130200	0.13569600	-0.38015400
H	-1.25790900	0.69690600	-1.26859600
C	-1.61747800	1.06903000	0.94180800
H	-1.34417100	0.47645300	1.83140500
O	-2.89945400	1.25812000	0.72123000
H	-0.99943500	1.98017600	0.84962600
O	-1.48864700	-1.15871900	-0.37928500
O	-2.90078300	-1.10330200	-0.67013500
H	-2.89932500	-1.31133200	-1.61382400

### 7) benzaldehyde

C	-2.21384100	-0.24842800	0.00011300
C	-1.32592400	-1.32774400	0.00008300

C	0.04301100	-1.09967100	-0.00013600
C	0.53281000	0.21268500	-0.00019700
C	-0.35950100	1.28892000	0.00007900
C	-1.73235900	1.05946300	-0.00012000
H	-3.28296400	-0.42941100	0.00045700
H	-1.70788100	-2.34224600	-0.00035300
H	0.75451300	-1.91698100	0.00001000
H	0.02618300	2.30391000	-0.00071900
H	-2.42448900	1.89357300	0.00026100
C	1.99246400	0.46543600	0.00008200
H	2.27265500	1.54160700	0.00053000
O	2.84275300	-0.39430200	0.00004900

### 8) formaldehyde

C	-0.52594400	0.00000600	0.00006300
H	-1.11812200	0.93871700	-0.00012700
O	0.67402200	-0.00001900	-0.00001600
H	-1.11839000	-0.93860200	-0.00012700

### 9) OH

H	0.00000000	0.00000000	-0.86685200
O	0.00000000	0.00000000	0.10835700

## Chapter 5 - Stability of Lithium Substituted Silyls Superalkali Species

[This chapter was adopted from an article with the same title published in Chemical Physics Letters (Chem.Phys.Lett. (2018), 692, 214-223). Authors include Adam Otten and Giovanni Meloni]

### Abstract

In this computational study we investigated superalkali species with the formula  $\text{SiLi}_n$  ( $n = 1 - 6$ ) and the mixed silyl species containing both H and Li,  $\text{SiHLi}$ ,  $\text{SiHLi}_2$ ,  $\text{SiH}_2\text{Li}$ ,  $\text{SiHLi}_3$ ,  $\text{SiH}_2\text{Li}_2$ ,  $\text{SiH}_3\text{Li}$ ,  $\text{SiHLi}_4$ ,  $\text{SiH}_2\text{Li}_3$ ,  $\text{SiH}_3\text{Li}_2$ ,  $\text{SiH}_4\text{Li}$ ,  $\text{SiHLi}_5$ ,  $\text{SiH}_2\text{Li}_4$ ,  $\text{SiH}_3\text{Li}_3$ ,  $\text{SiH}_4\text{Li}_2$ , and  $\text{SiH}_5\text{Li}$ . The CBS-QB3 composite model was employed to obtain optimized geometries and energetics. We found that these clusters increase in stability from  $\text{SiLi}$  to  $\text{SiLi}_4$ , but decrease in stability from  $\text{SiLi}_4$  to  $\text{SiLi}_6$ . Our findings also show that these clusters exhibit stronger superalkali properties when increasing the amount of substituted lithium.

## 5.1 Introduction:

With the growing need for alternative fuel sources, hydrogen energy has become a possible solution because of its planetary abundance, its ability to burn clean, and contains the highest energy density per unit mass [1]. Currently, conventional methods to store hydrogen in its pure form are either as a compressed gas or cryogenic liquid [2]. These processes are not ideal for mobile applications since they are highly energy intensive and have inherent safety risks [3]. Recent investigations have focused on metal hydrides as hydrogen storage carriers since they rely on stronger chemical interactions, resulting in materials that store hydrogen at higher temperatures [4]. Superalkali metal hydrides and electrolytes have also gained much attention as potential hydrogen storage compounds due to their light weight and high energy density [5].

Superalkali species are defined as compounds whose first ionization energy is lower than that of alkali metals [6, 7]. This low ionization energy suggests that these species are highly reactive, which makes them ideal for synthesizing charge transfer salts [8, 9]. Superalkali species also have potential applications for electrochemical storage as in lithium ion batteries because of their charge transfer ability [8]. This theoretical study aims to develop a new class of compounds that exhibits these superalkali characteristics.

Silicon is the second most abundant element in the earth's crust and works as an ideal semiconductor due to its narrow band gap of 1.1 eV [10]. This property renders silicon a promising material for photoelectrodes in solar fuel cells and for composite membranes in proton-exchange membrane fuel cells [10, 11].

Previous theoretical studies conducted by Gutsev and coworkers [7] were successful in optimizing superalkali species such as  $\text{Li}_2\text{F}$ ,  $\text{Li}_3\text{O}$ ,  $\text{Li}_4\text{N}$ ,  $\text{Li}_3\text{S}$ , and  $\text{Li}_4\text{P}$ , by doping non-metals and halogens with lithium. Meloni and coworkers [12, 13] investigated compounds, oxides and phosphides, of the  $\text{Li}_3\text{F}_2$  superalkali using the CBS-QB3 composite model, finding that these clusters increase in stability upon the addition of oxygen and phosphorus atoms. Castleman and coworkers [14] calculated new superalkali clusters by combining the superhalogen  $\text{Al}_{13}$  species with small superalkalis showing ionization energies as low as 2.49 eV, which they named as "ultra alkali motifs." Recently, Jena and coworkers [15] were successful in calculating a variety of superalkali zintl phase phosphorous clusters, showing that these species exhibit superalkali characteristics when complexed with methyl substituents. Calculations on lithium substituted group 14 elements have been achieved by Patrick and coworkers, where they calculated small

carbon-lithium clusters at the B3LYP level of theory [16]. He and coworkers [17] were successful in calculating  $\text{SiLi}_n$  clusters for  $n = 4-16$ , but energetics results for clusters smaller than  $n = 4$  have not been achieved. Pure silicon clusters were previously studied by Meloni and Gingerich [18], where they investigated the thermodynamic properties of  $\text{Si}_7$  and  $\text{Si}_8$  by Knudsen cell mass spectrometry, finding that these species have a higher stability when containing an even number of atoms. Meloni et al. [19] also investigated the structural transitions of  $\text{Si}_n$  clusters where  $n = 4-35$  by VUV negative ion photoelectron spectroscopy, and determined that these clusters decrease in band gap energy and form a continuum when increasing in cluster size. A recent theoretical study by Zhao and coworkers [20] investigated the structural motifs of  $\text{Si}_n$  clusters where  $n = 2-33$  by optical absorption spectroscopy, and found that these species can modulate light absorption by controlling the structural design and building pattern. In this study, we investigated the stability of lithium substituted silicon compounds with the formulas  $\text{SiLi}_x$  ( $x = 1 - 6$ ) and  $\text{SiH}_n\text{Li}_x$  ( $x = 1 - 6$ ,  $n = 0 - 5$ , and  $n + x = 1 - 6$ ) using the CBS-QB3 composite model. Adiabatic ionization energies, together with atomization enthalpies, fragmentation energies, binding energies, and enthalpy of formation are provided. These results help in understanding the general bonding and stability of these clusters.

## 5.2 Methods:

All electronic energies and molecular structure parameters are optimized using the CBS-QB3 composite method [21] with Gaussian09 [22] and Gaussview 5.0 [23] for visualization purposes. The CBS-QB3 method is widely used because it provides accurate energy values, with an absolute error less than 1.0 kcal/mol, and reliable structural optimized parameters [12]. To maximize efficiency, this method combines CBS-Q energy computations with B3LYP density functional theory (DFT) optimized geometries and frequencies [24]. Adiabatic ionization energies (AIE) are obtained by performing CBS-QB3 calculations on the ground state neutral and cation (+1 charge) species of each cluster. The AIE is defined as the difference of the zero point corrected (ZPE) total electronic energies ( $E_0$ ) between the neutral species and its corresponding cation. Atomization enthalpies ( $\Delta_{\text{at}}H_0^\circ$ ), which are directly related to the stability of each species, are taken from the difference between the zero point corrected total electronic energies of neutral clusters and the sum of the calculated ground state electronic energies of its constituent atoms [12]. Larger atomization energy values correspond to larger energy needed to keep the species integer,



in other words it can be considered as the cohesive energy of a gaseous species. To determine thermodynamic stability, enthalpies of formation ( $\Delta_f H_0^\circ$ ) are calculated by taking the difference between calculated atomization enthalpies and the sum of the literature enthalpies of formation for the constituent atoms in the gas phase [13]. Binding energies for pure clusters are calculated using the equation  $BE = \Delta_{at} H_0^\circ(\text{SiLi}_n)/n$ , where  $n \geq 2$  [17]. Fragmentation energies for the pure compounds are used to determine relative thermodynamic stability, and are calculated using the equation  $\Delta_{frag} H_0^\circ = \Delta_{at} H_0^\circ(\text{SiLi}_x) - \Delta_{at} H_0^\circ(\text{SiLi}_{x-1})$ , where  $x \geq 2$ . Higher fragmentation energies correspond to a greater stability than the neighboring clusters containing one more or one less atom, and are defined as the minimum energy to remove an atom from the cluster [18]. Highest Occupied Molecular Orbital – Lowest Unoccupied Molecular Orbital (HOMO-LUMO) gap energies are determined by taking the difference between molecular orbital (MO) energies, calculated using the restricted open shell method, ROB3LYP, when appropriate. The energetics results are listed in Table 1.

### 5.3 Results and Discussion

To prove the accuracy of the applied computational methodology, calculations were performed on the silicon hydride compounds  $\text{SiH}_n$  ( $n = 1-6$ ) for which literature data are available. Calculations were also performed at different spin multiplicities to establish the correct ground electronic state. The calculated AIE of the doublet ground electronic state of silyllidyne ( $\text{SiH}$ ) using the CBS-QB3 composite method is 7.83 eV, which is in good agreement with the photoionization mass spectroscopic value of 7.91 eV [25]. Our calculated  $\text{SiH}$  bond length of 1.530 Å and vibrational frequency of 2018.5  $\text{cm}^{-1}$  agree well with the experimental values of 1.520 Å and 2042.0  $\text{cm}^{-1}$  [26]. The computed AIE of  $\text{SiH}_2$  is 8.16 eV, which also agrees with the mass spectroscopic value of 8.24 eV [25]. Our calculated bond lengths and second vibrational mode for  $\text{SiH}_2$  (1.485 Å and 893  $\text{cm}^{-1}$ ) match well with the literatures values of 1.487 Å and 860  $\text{cm}^{-1}$  [27]. The silyl radical  $\text{SiH}_3$  has a reported spectroscopic AIE of 8.01 eV [25], which is in good agreement with our calculated value of 8.08 eV. Our computed Si-H bond lengths of 1.483 Å and the second vibrational mode of 940  $\text{cm}^{-1}$  for  $\text{SiH}_3$  also match the values of 1.480 Å and 925  $\text{cm}^{-1}$  [27], respectively.  $\text{SiH}_4$  has a reported AIE of 11.02 eV [25], which matches perfectly with our calculated value of 11.01 eV. Bond lengths of 1.481 Å and the second vibrational mode of 926  $\text{cm}^{-1}$  are also in good agreement with the literature values of 1.480 Å and 960  $\text{cm}^{-1}$  [27],

respectively. Gong and coworkers [28] were successful in calculating SiH<sub>5</sub> with the D<sub>3h</sub> symmetry using MP2 and UHF levels of theory. Unfortunately, we were unable to reproduce their results. Attempts to optimize SiH<sub>5</sub> using CBS-QB3, B3LYP, CCSD, and MP2 methodologies were unsuccessful because SiH<sub>5</sub> results to be unbound dissociating into SiH<sub>4</sub> + H. The compound SiH<sub>6</sub> was not previously studied. Calculations performed on SiH<sub>6</sub> at the CBS-QB3, CBSB7, B3LYP, CCSD, and MP2 levels of theory yield SiH<sub>4</sub> + H<sub>2</sub>. The computational methodology is additionally evaluated on the diatomic molecule SiLi (Fig. 1) with a ground state as a quartet and an AIE of 6.29 eV, which also agrees with the literature value of 6.44 eV (PMP4) [29]. SiLi bond distance and vibrational frequency have not been experimentally determined, but our calculated values of 2.367 Å and 444.4 cm<sup>-1</sup> are in good agreement with the calculated literature values of 2.355 Å and 472 cm<sup>-1</sup> at the MP2 level of theory [29].

**Table 1.** Energy quantities for SiH<sub>x</sub>Li<sub>n</sub> and SiLi<sub>n</sub> neutral clusters.  $\Delta_{\text{at}}\text{H}_0^\circ$ ,  $\Delta_{\text{f}}\text{H}_0^\circ$ ,  $\Delta_{\text{frag}}\text{H}_0^\circ$ , and BE are reported in kJ mol<sup>-1</sup>. AIE are in eV.

Species	Symmetry	$\Delta_{\text{at}}\text{H}_0^\circ$	$\Delta_{\text{f}}\text{H}_0^\circ$	$\Delta_{\text{frag}}\text{H}_0^\circ$	BE	AIE
SiH	C <sub>∞v</sub>	299	363	-	-	7.83
SiLi	C <sub>∞v</sub>	177	478	-	-	6.29
SiHLi	C <sub>s</sub>	440	379	-	-	5.99
SiLi <sub>2</sub>	D <sub>∞h</sub>	289	472	148	145	4.81
SiH <sub>2</sub> Li	C <sub>2v</sub>	785	251	-	-	6.06
SiHLi <sub>2</sub>	C <sub>2v</sub>	618	359	-	-	4.94
SiLi <sub>3</sub>	C <sub>2v</sub>	492	427	167	164	4.69
SiH <sub>3</sub> Li	C <sub>1</sub>	1118	134	-	-	6.96
SiH <sub>2</sub> Li <sub>2</sub>	C <sub>2v</sub>	929	264	-	-	5.24
SiHLi <sub>3</sub>	C <sub>1</sub>	802	333	-	-	4.64
SiLi <sub>4</sub>	C <sub>2v</sub>	692	385	200	173	4.47
SiH <sub>4</sub> Li	C <sub>1</sub>	1227	241	-	-	4.11
SiH <sub>3</sub> Li <sub>2</sub>	C <sub>1</sub>	1194	212	-	-	4.01
SiH <sub>2</sub> Li <sub>3</sub>	C <sub>1</sub>	1039	312	-	-	3.87
SiHLi <sub>4</sub>	C <sub>1</sub>	914	379	-	-	3.53
SiLi <sub>5</sub>	C <sub>2v</sub>	837	397	145	164	3.73
SiH <sub>5</sub> Li	C <sub>1</sub>	1540	143	-	-	7.33
SiH <sub>4</sub> Li <sub>2</sub>	C <sub>1</sub>	1518	93	-	-	6.68
SiH <sub>3</sub> Li <sub>3</sub>	C <sub>1</sub>	1337	107	-	-	4.77
SiH <sub>2</sub> Li <sub>4</sub>	C <sub>1</sub>	1235	197	-	-	4.28

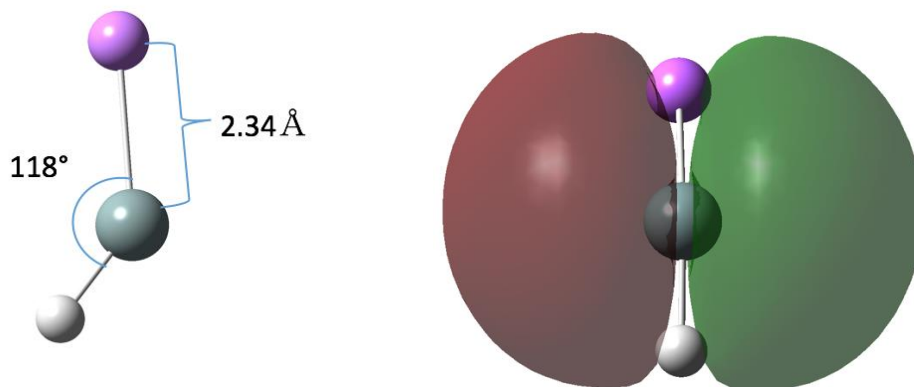
SiHLi <sub>5</sub>	C <sub>2v</sub>	1055	395	-	-	4.15
SiLi <sub>6</sub>	O <sub>h</sub>	984	408	146	153	3.88

In the following sections, the silicon clusters are grouped based on the total number of atoms bonded to Si. All the relevant energetics information, enthalpies of formation at 0 K, atomization enthalpies at 0 K, fragmentation energies, binding energies, and adiabatic ionization energies are presented on Table 1. Upon substitution of one H with one Li atom SiH<sub>2</sub> (C<sub>2v</sub>) loses its symmetry to yield SiHLi (C<sub>s</sub>) with an increased H-Si-Li bond angle of 139° (Fig. 1).

### SiLi



### SiHLi



## SiLi<sub>2</sub>

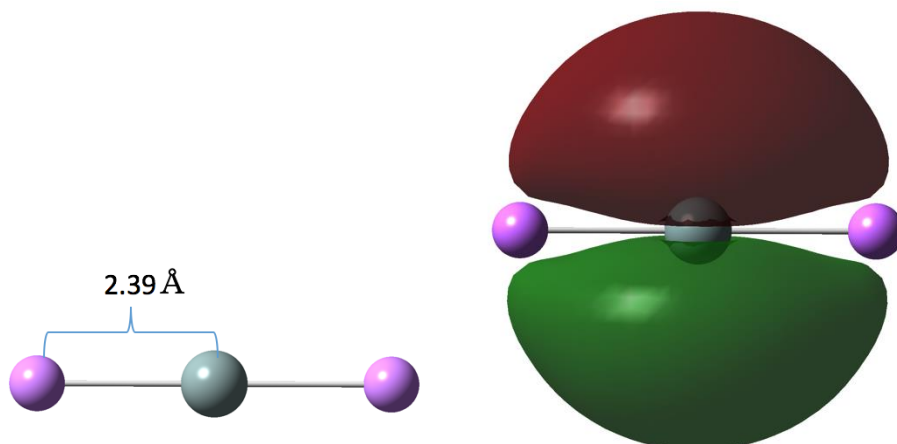
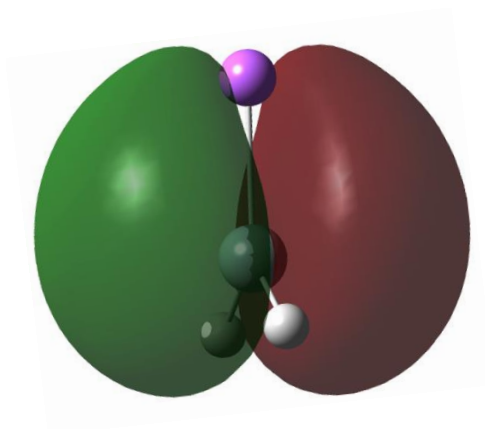
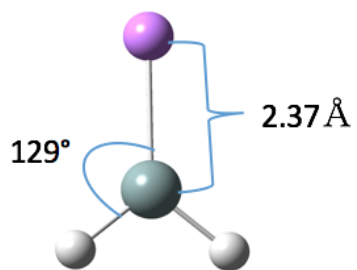


**Figure 1.** Optimized structures and highest-occupied molecular orbitals of SiLi, SiHLi, and SiLi<sub>2</sub>.

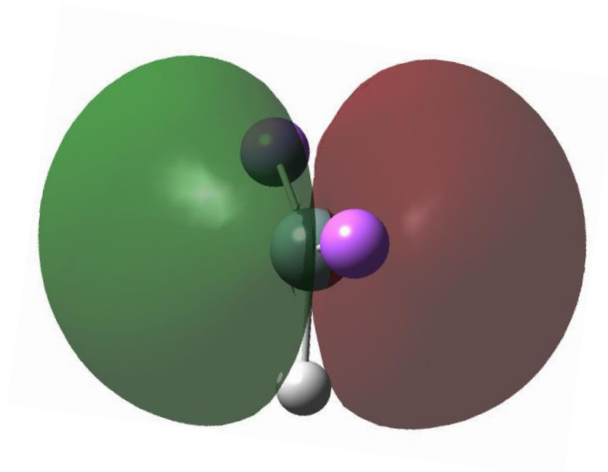
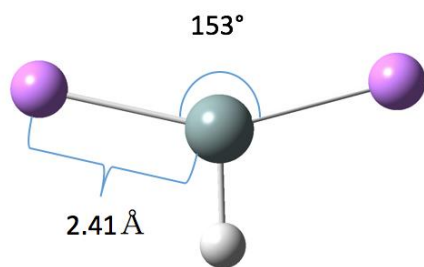
Upon the substitution of the second lithium, the molecule SiLi<sub>2</sub> (Fig. 1) exhibits a linear geometry ( $D_{\infty h}$ ) in the ground state as a triplet, which differs from bent singlet SiH<sub>2</sub>. SiLi<sub>2</sub> is the first superalkali species with an AIE of 4.81 eV. SiLi<sub>2</sub> becomes less energetically stable with respect to SiHLi. This is shown by a decrease of its atomization enthalpy by 151 kJ mol<sup>-1</sup> and an increase of its formation enthalpy by 93 kJ mol<sup>-1</sup>. SiLi<sub>2</sub> displays the least stability, since it has the lowest binding and fragmentation energies out of all the lithiated clusters.

When a H is substituted with one Li atom the SiH<sub>3</sub> ( $C_{3v}$ ) becomes SiH<sub>2</sub>Li ( $C_{2v}$ ) with the elongated Si-Li distance of 2.73 Å (Fig.2). With the next substitution yielding SiHLi<sub>2</sub> (Fig. 2), the compound still retains the  $C_{2v}$  symmetry with a Li-Si-Li bond angle of 153° and Si-Li bond lengths of 2.41 Å. The fully lithiated SiLi<sub>3</sub> assumes a “T-shaped- like” ( $C_{2v}$ ) planar structure (Fig. 2).

**SiH<sub>2</sub>Li**



**SiHLi<sub>2</sub>**



**SiLi<sub>3</sub>**

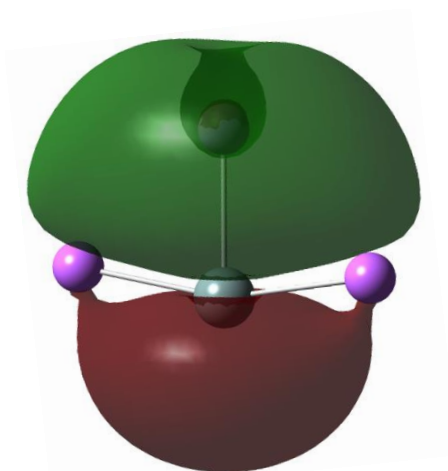
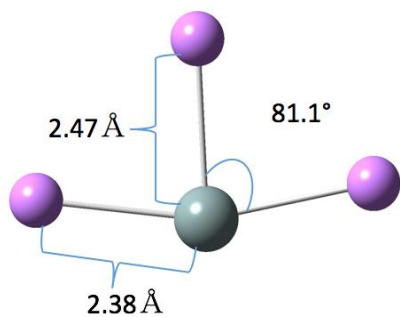
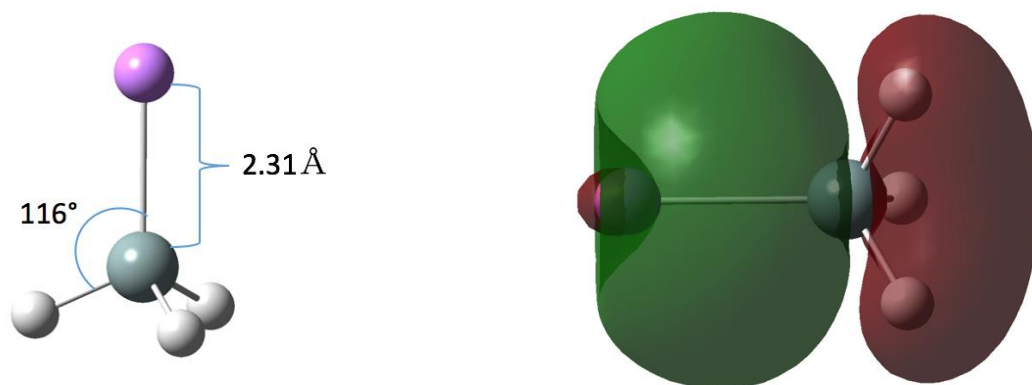


**Figure 2.** Optimized structures and HOMO's of SiH<sub>2</sub>Li, SiHLi<sub>2</sub>, and SiLi<sub>3</sub>.

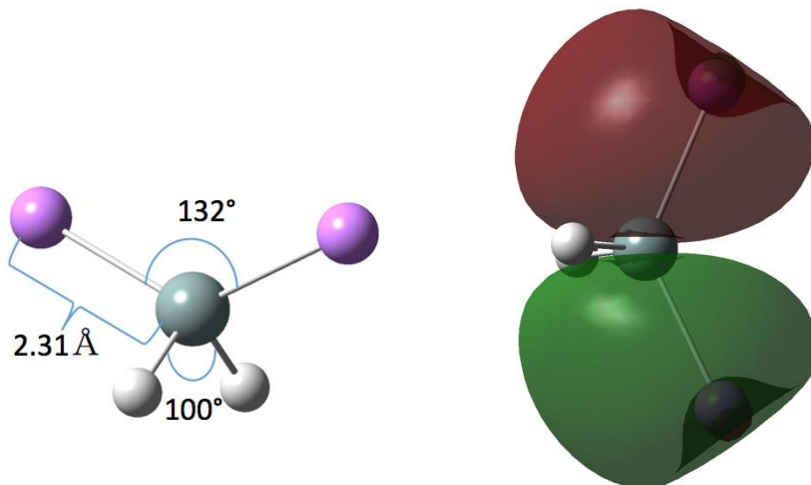
Two species in this group of clusters display superalkali character.  $\text{SiHLi}_2$  and  $\text{SiLi}_3$  have an AIE of 4.94 and 4.69 eV, respectively, much lower than atomic lithium AIE of 5.39 eV [30]. These structures become less energetically stable as H atoms are substituted, which is seen from the decrease of the atomization enthalpy and increase of the enthalpy of formation. There is an increase in binding and fragmentation energy from  $\text{SiLi}_2$  to  $\text{SiLi}_3$ , which suggests that  $\text{SiLi}_3$  is more thermodynamically stable.

In the fourth group of clusters shown in Fig. 3, there is a change in geometry on the first substitution from tetrahedral  $\text{SiH}_4$  ( $T_d$ ) to  $\text{SiH}_3\text{Li}$  ( $C_{3v}$ ) with the Si-Li bond length of 2.46 Å and the H-Si-Li bond angles of  $116^\circ$ . Upon the second substitution  $\text{SiH}_2\text{Li}_2$  ( $C_{2v}$ ) takes a tetrahedral-like geometry with the Si-Li distances of 2.45 Å, H-Si-H angle of  $100^\circ$ , and Li-Si-Li angle of  $132^\circ$ . With the third substitution  $\text{SiHLi}_3$  ( $C_1$ ) loses the main symmetry with a Si-Li bond distance of 2.41 Å and the other two Si-Li lengths of 2.44 Å.

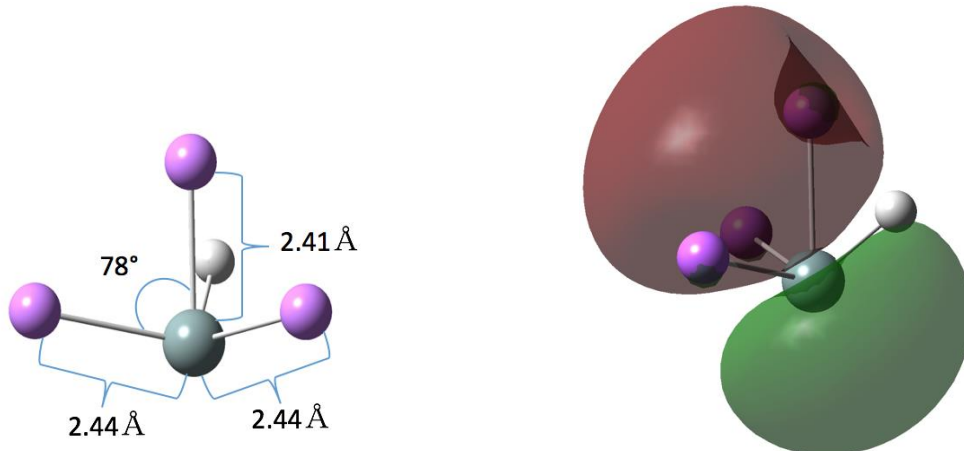
**$\text{SiH}_3\text{Li}$**



**$\text{SiH}_2\text{Li}_2$**



### SiHLi<sub>3</sub>



### SiLi<sub>4</sub>

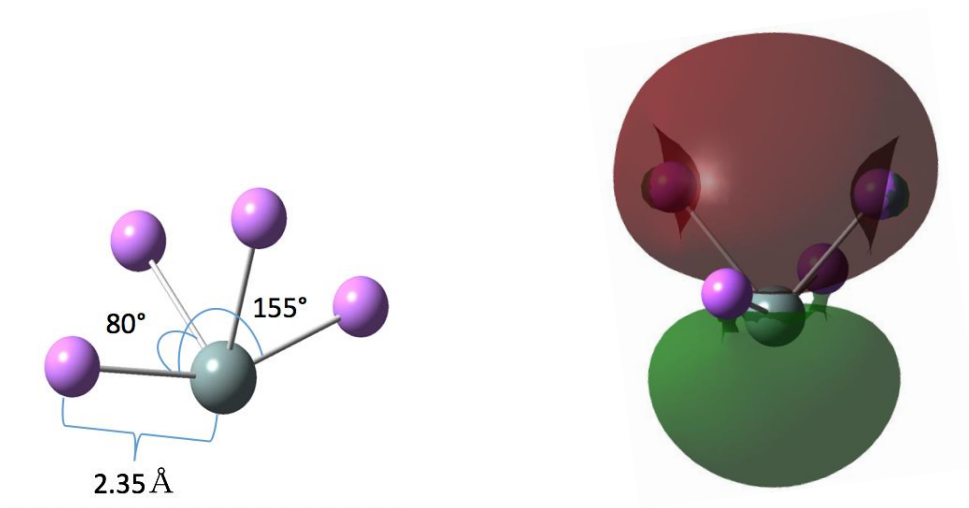
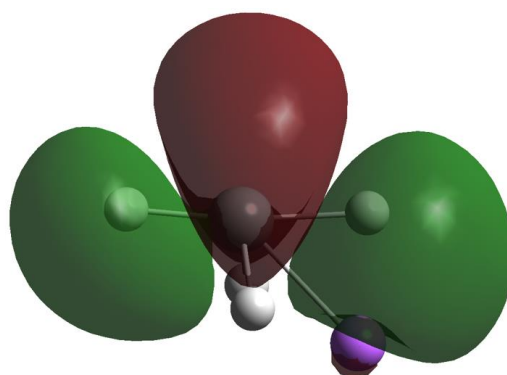
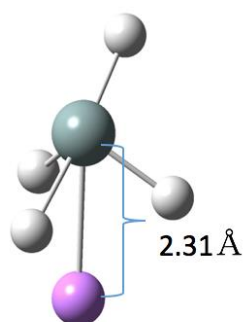


**Figure 3.** Optimized structures and HOMO's of SiH<sub>3</sub>Li, SiH<sub>2</sub>Li<sub>2</sub>, SiHLi<sub>3</sub>, and SiLi<sub>4</sub>.

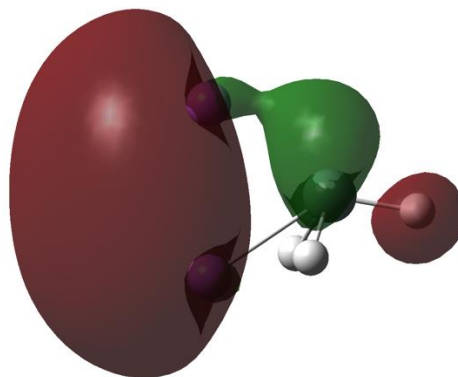
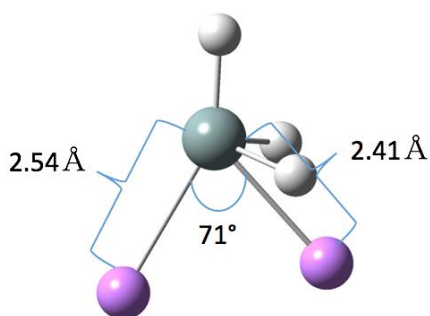
The last substitution yielding SiLi<sub>4</sub> creates a see-saw-like ( $C_{2v}$ ) structure with four identical Si-Li distances of 2.35 Å. Three species in this group display superalkali properties, with SiLi<sub>4</sub> having the lowest AIE of 4.47 eV. While SiLi<sub>4</sub> is more energetically stable than both SiLi<sub>2</sub> and SiLi<sub>3</sub> because of higher binding and fragmentation energy, we are still seeing a decrease in stability with each additional lithium substitution, with an overall atomization enthalpy decrease of 426 kJ mol<sup>-1</sup> and formation enthalpy increase of 251 kJ mol<sup>-1</sup> from SiH<sub>3</sub>Li to SiLi<sub>4</sub>.

$\text{SiH}_4\text{Li}$  (Fig. 4) takes an asymmetric structure ( $C_1$ ) with Si-Li bond distances of 2.31 Å. The second substitution to  $\text{SiH}_3\text{Li}_2$  creates a similar geometry as  $\text{SiH}_4\text{Li}$  with Si-Li bond lengths of 2.42 Å. Also  $\text{SiH}_2\text{Li}_3$  takes an asymmetric structure with Si-Li distances of 2.52 Å. The fourth substitution yields a structure with Si-Li lengths of 2.46 Å and Li-Si-Li angles of  $67^\circ$ ,  $80^\circ$ , and  $155^\circ$ . The final substitution to  $\text{SiLi}_5$  ( $C_{2v}$ ) displays an “umbrella-like” geometry with 4 equatorial lithium at  $88^\circ$  and  $92^\circ$  apart from each other and one lithium in the axial position, with Si-Li bond equatorial lengths of 2.39 Å and axial distance of 2.45 Å.

**$\text{SiH}_4\text{Li}$**

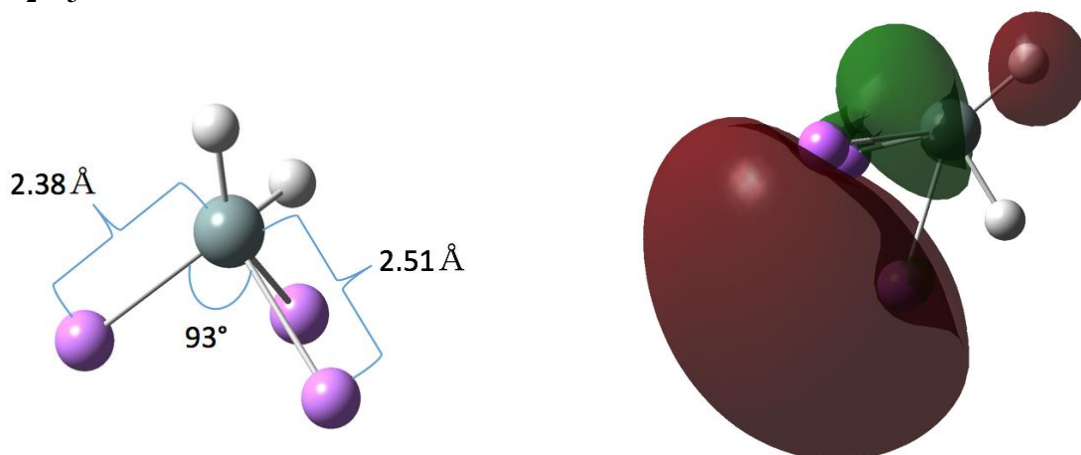


**$\text{SiH}_3\text{Li}_2$**

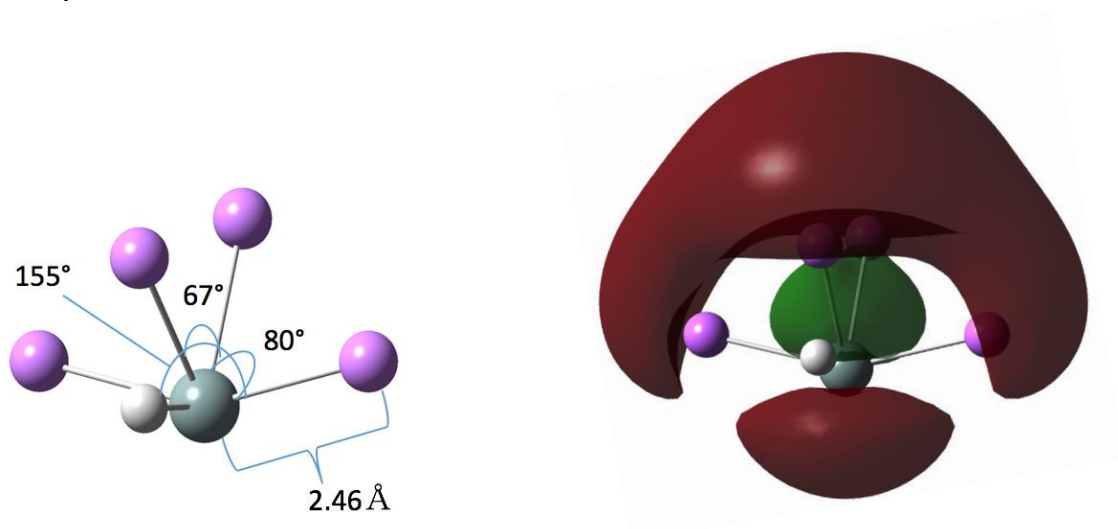




**SiH<sub>2</sub>Li<sub>3</sub>**



**SiHLi<sub>4</sub>**



**SiLi<sub>5</sub>**

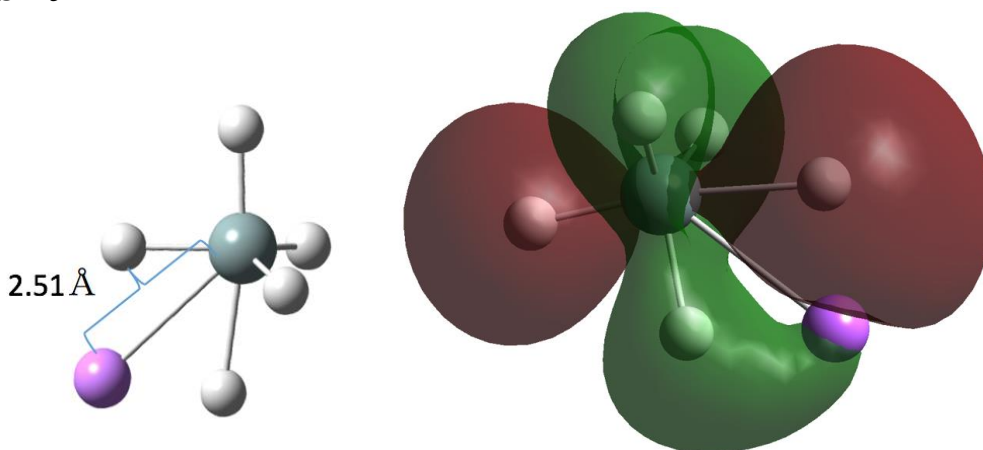


**Figure 4.** Optimized structures and HOMO's of SiH<sub>4</sub>Li, SiH<sub>3</sub>Li<sub>2</sub>, SiH<sub>2</sub>Li<sub>3</sub>, SiHLi<sub>4</sub>, and SiLi<sub>5</sub>.

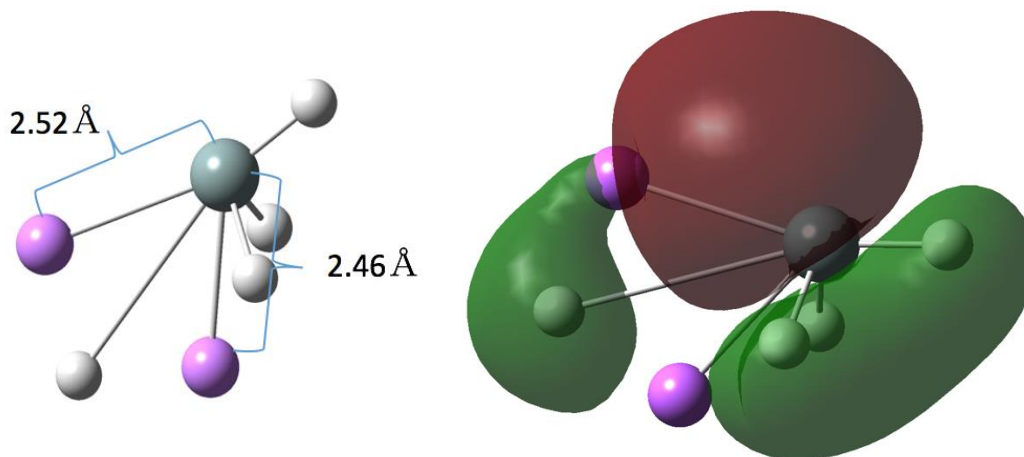
Each species in this fourth group of clusters demonstrates superalkali properties, with tri-, tetra-, and penta-substituted species displaying an ionization energy lower than atomic Cesium at 3.89 eV [30]. The AIE calculations for  $\text{SiLi}_5$  match well with He and coworkers [17] value of 3.72 eV.  $\text{SiLi}_5$  is less stable than  $\text{SiLi}_4$  because of its lower fragmentation and binding energy.

In this last group of clusters shown in Fig. 5, we do not see the appearance of a superalkali species until the third substitution yielding  $\text{SiH}_3\text{Li}_3$  with a kite-like geometry ( $C_1$ ). The fourth and fifth substitutions produce  $C_1$  and  $C_{2v}$  structures, respectively.

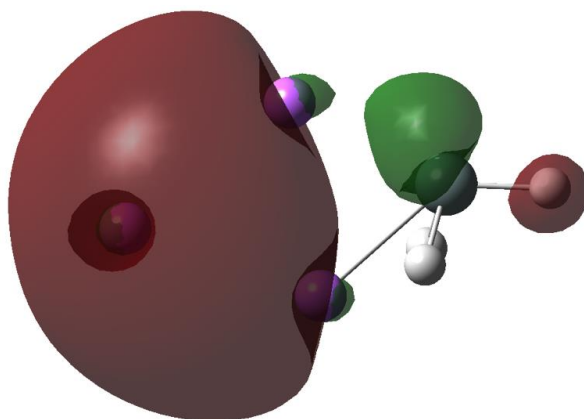
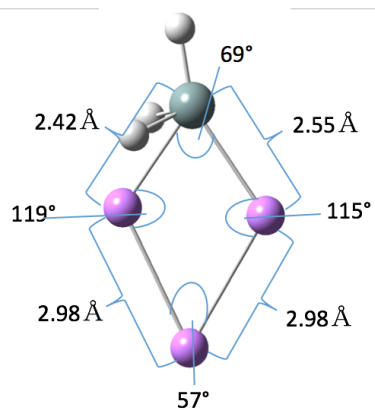
**$\text{SiH}_5\text{Li}$**



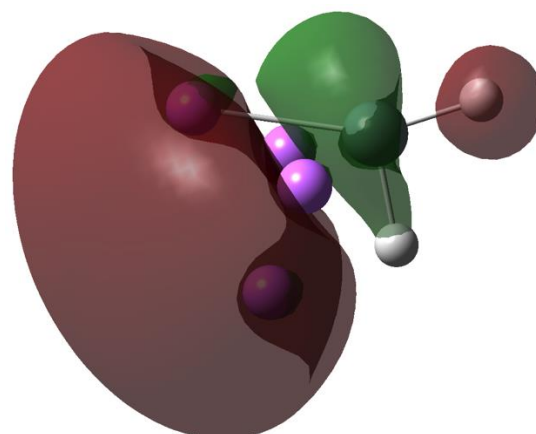
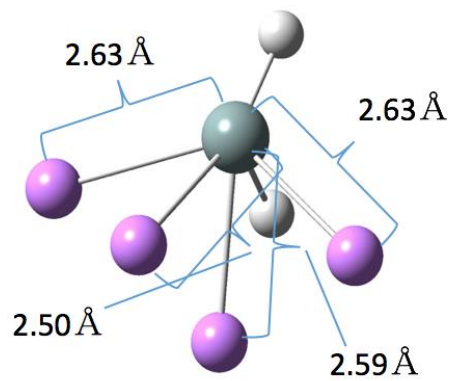
**$\text{SiH}_4\text{Li}_2$**



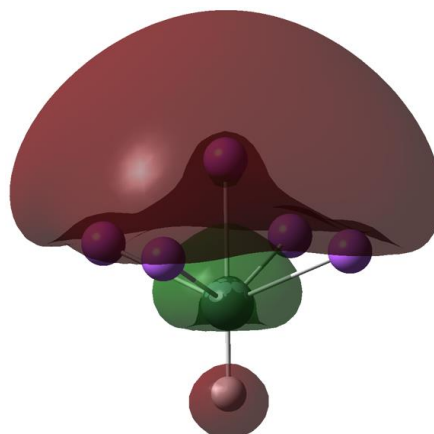
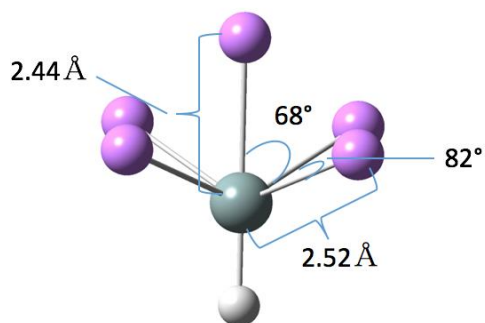
### SiH<sub>3</sub>Li<sub>3</sub>



### SiH<sub>2</sub>Li<sub>4</sub>



### SiHLi<sub>5</sub>



### SiLi<sub>6</sub>

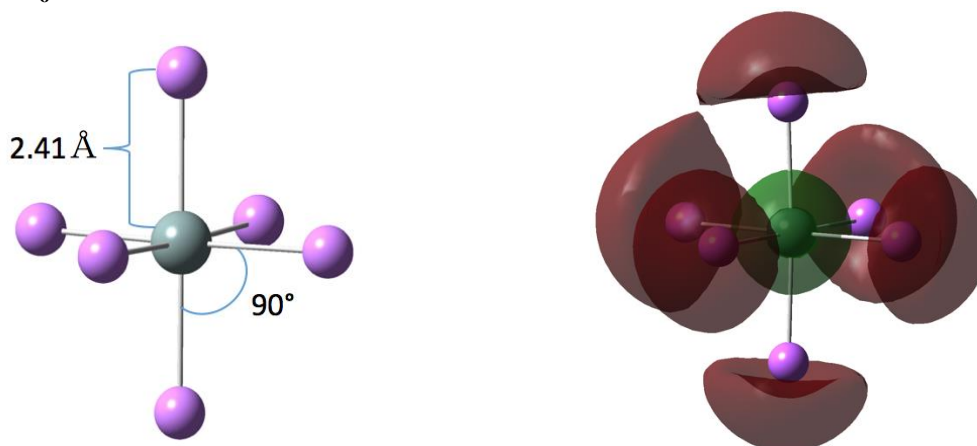


**Figure 5.** Optimized structures and HOMO's of SiH<sub>5</sub>Li, SiH<sub>4</sub>Li<sub>2</sub>, SiH<sub>3</sub>Li<sub>3</sub>, SiH<sub>2</sub>Li<sub>4</sub>, SiHLi<sub>5</sub>, and SiLi<sub>6</sub>.

The fully lithiated SiLi<sub>6</sub> species (O<sub>h</sub>) exhibits an octahedral geometry with Si-Li bond distances of 2.41 Å and an adiabatic ionization energy of 3.88 eV, which matches well with He and coworkers [17] calculation of 3.91 eV at the CCSD/B3LYP level of theory. Like the previous group, there is a decrease in binding energy and the fragmentation energy remains constant.

In Fig. 6 the AIE's of the lithiated clusters are plotted against the number of Li atoms.

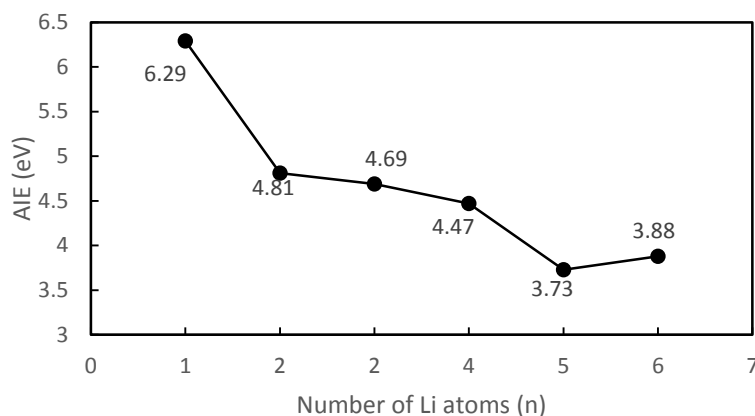


**Figure 6.** CBS-QB3 adiabatic ionization energies in eV of the fully lithiated SiLi<sub>n</sub> clusters vs. number of Li atoms (n).

The trend shows that upon sequential addition of Li the AIE's become smaller reaching the lowest value for SiLi<sub>5</sub>. A larger drop of the AIE value from the first four clusters, SiLi, SiLi<sub>2</sub>, SiLi<sub>3</sub>, SiLi<sub>4</sub>, to SiLi<sub>5</sub> and SiLi<sub>6</sub> can be explained observing the HOMO's of these species and their atomic

charges. Up to SiLi<sub>4</sub> the HOMO electron density is mainly localized on the central Si atom. For SiLi<sub>5</sub> and SiLi<sub>6</sub> the HOMO electron density starts shifting to the Li atoms. In SiLi<sub>5</sub>, approximately one third of the HOMO electron density is localized on the Li atoms and in SiLi<sub>6</sub> the HOMO electron density is localized on the six Li atoms.

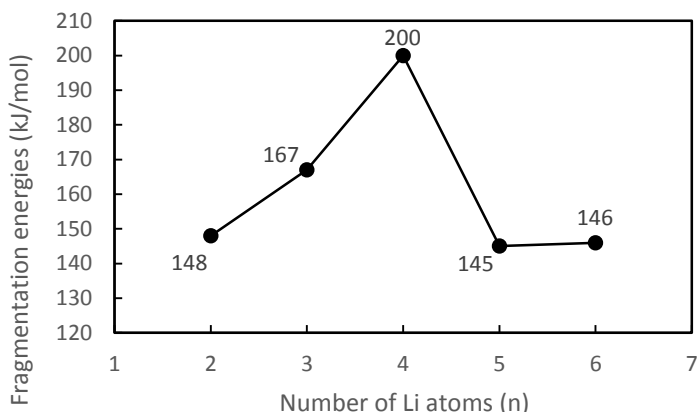


**Figure 7.** Fragmentation energies,  $\Delta_{\text{at}}\text{H}_0^\circ(\text{SiLi}_x) - \Delta_{\text{at}}\text{H}_0^\circ(\text{SiLi}_{x-1})$ , in  $\text{kJ mol}^{-1}$  of the SiLi<sub>n</sub> (n = 2 – 6) clusters vs. number of Li atoms (n).

The fragmentation and binding energies plotted against the number of Li atoms shown in Fig. 7 and 8, respectively, present a maximum corresponding to the most stable species within the investigated lithiated clusters, i.e., SiLi<sub>4</sub>. Tong *et al.* [31] attributed the magnitude of the HOMO-LUMO gap to the molecular stability and reactivity of the clusters, such that a larger energy gap implied decreased reactivity and, therefore, increased molecular stability.

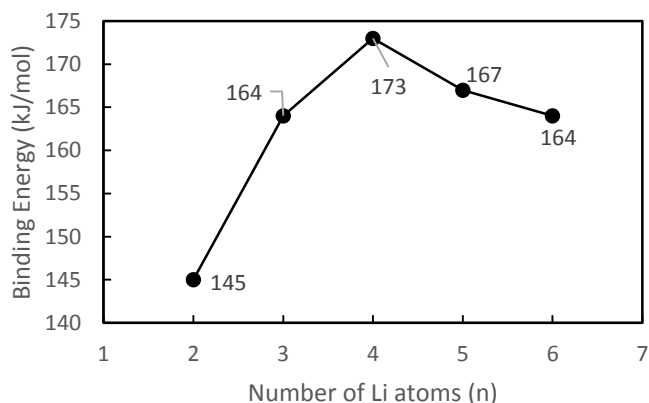


**Figure 8.** Binding energies,  $\Delta_{\text{at}}\text{H}_0^\circ(\text{SiLi}_n)/n$ , in  $\text{kJ mol}^{-1}$  of the SiLi<sub>n</sub> (n = 2 – 6) clusters vs. number of Li atoms (n).

The HOMO-LUMO gaps in Fig. 9 therefore show that the most stable species is again  $\text{SiLi}_4$  with the largest gap of 1.91 eV.

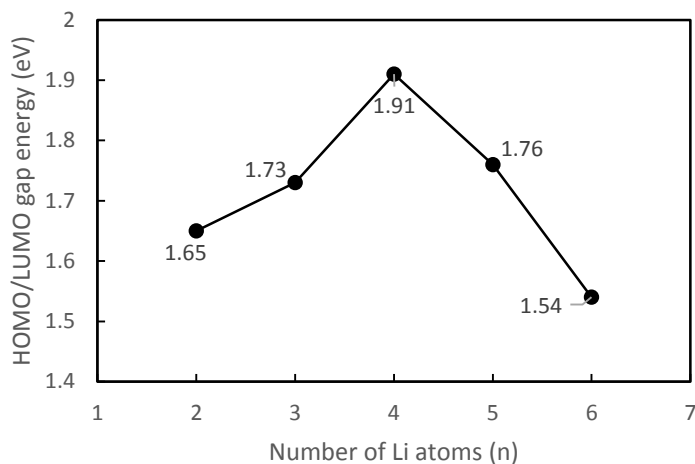


**Figure 9.** HOMO/LUMO gap energies in eV of the  $\text{SiLi}_n$  ( $n = 2 - 6$ ) clusters vs. number of Li atoms ( $n$ ).

#### 5.4 Conclusions:

Electronic energies and molecular structural parameters have been computed for fully lithiated  $\text{SiLi}_n$  ( $n = 1 - 6$ ) clusters using the CBS-QB3 composite method. Using the calculated atomization enthalpies, formation enthalpies, fragmentation energies, binding energies, adiabatic ionization energies, and HOMO/LUMO gap energies for neutral structures, the relative stability of these species has been investigated. It was found that the smallest superalkali is  $\text{SiLi}_2$  with an AIE of 4.81 eV. From the analysis of HOMO/LUMO gap energies we are able to qualitatively quantify the stability of the pure species, which are found to increase in stability upon each lithium substitution up until  $\text{SiLi}_4$ , then to decrease in stability from  $\text{SiLi}_4$  to  $\text{SiLi}_6$ , with  $\text{SiLi}_4$  being the most stable out of all the pure clusters. We are seeing this enhanced stability in  $\text{SiLi}_4$  over the other pure clusters because all valence electrons in  $\text{SiLi}_4$  are occupied in bonding, while the other pure clusters have unpaired electrons unused during bonding. The larger drop in the AIE values of  $\text{SiLi}_5$

and  $\text{SiLi}_6$  is explained in the shifting of the electron density from the central Si atom to the Li atoms.

### **Acknowledgments**

This work is supported by American Chemical Society – Petroleum Research Fund Grant # 56067-UR6 and the University of San Francisco via the Faculty Development Fund. The authors would also like to thank the Director of Scientific Computing, of the Department of Computer Science, Mr. A. Fedosov, at the University of San Francisco for providing the space and general upkeep of the computer cluster used to perform the calculations.

## 5.5 References:

1. Jena, P., *Materials for Hydrogen Storage: Past, Present, and Future*. J. Phys. Chem. Lett., 2011. **2**(3): p. 206-211.
2. Schlapbach, L. and A. Züttel, *Hydrogen-storage materials for mobile applications*. Nature, 2001. **414**(6861): p. 353-8.
3. Hamilton, C.W., et al., *B-N compounds for chemical hydrogen storage*. Chem. Soc. Rev., 2009. **38**(1): p. 279-293.
4. Mohtadi, R., A. Remhof, and P. Jena, *Complex metal borohydrides: multifunctional materials for energy storage and conversion*. J Phys Condens Matter, 2016. **28**(35): p. 353001.
5. Giri, S., S. Behera, and P. Jena, *Superhalogens as building blocks of halogen-free electrolytes in lithium-ion batteries*. Angew Chem Int Ed Engl, 2014. **53**(50): p. 13916-9.
6. Gutsev, G.L. and A.I. Boldyrev, *DVM  $X\alpha$  calculations on the electronic structure of "superalkali" cations*. Chem. Phys. Lett., 1982. **92**(3): p. 262-6.
7. Gutsev, G.L. and A.I. Boldyrev, *Electronic structure of superhalides and superalkali compounds*. Usp. Khim., 1987. **56**(6): p. 889-910.
8. Giri, S., S. Behera, and P. Jena, *Superalkalis and superhalogens as building blocks of supersalts*. J Phys Chem A, 2014. **118**(3): p. 638-45.
9. Li, Y., D. Wu, and Z.R. Li, *Compounds of superatom clusters: preferred structures and significant nonlinear optical properties of the BLi<sub>6</sub>-X (X = F, LiF<sub>2</sub>, BeF<sub>3</sub>, BF<sub>4</sub>) motifs*. Inorg Chem, 2008. **47**(21): p. 9773-8.
10. Sun, K., et al., *Enabling Silicon for Solar-Fuel Production*. Chem. Rev. (Washington, DC, U. S.), 2014. **114**(17): p. 8662-8719.
11. Gold, S., et al., *Acid loaded porous silicon as a proton exchange membrane for micro-fuel cells*. J. Power Sources, 2004. **135**(1-2): p. 198-203.
12. Cochran, E. and G. Meloni, *Hypervalence in monoxides and dioxides of superalkali clusters*. J. Chem. Phys., 2014. **140**(20): p. 204319/1-204319/13.
13. Cochran, E., G. Muller, and G. Meloni, *Stability and bonding of new superalkali phosphide species*. Dalton Trans., 2015. **44**(33): p. 14753-14762.
14. Reber, A.C., S.N. Khanna, and A.W. Castleman, Jr., *Superatom Compounds, Clusters, and Assemblies: Ultra Alkali Motifs and Architectures*. J. Am. Chem. Soc., 2007. **129**(33): p. 10189-10194.
15. Giri, S., G.N. Reddy, and P. Jena, *Organo-Zintl Clusters [P<sub>7</sub>R<sub>4</sub>]: A New Class of Superalkalis*. J Phys Chem Lett, 2016. **7**(5): p. 800-5.
16. Patrick, A.D., A. Skene, and E. Blaisten-Barojas, *Energetics and bonding in small lithiated carbon clusters*. J. Mol. Struct.: THEOCHEM, 2007. **807**(1-3): p. 163-172.
17. He, N., H.-B. Xie, and Y.-H. Ding, *Structures and stability of lithium monosilicide clusters SiLin (n = 4-16): what is the maximum number, magic number, and core number for lithium coordination to silicon?* J. Comput. Chem., 2008. **29**(11): p. 1850-1858.
18. Meloni, G. and K.A. Gingerich, *Thermodynamic investigation of the Si<sub>7</sub> and Si<sub>8</sub> clusters by Knudsen cell mass spectrometry*. J. Chem. Phys., 2001. **115**(12): p. 5470-5476.
19. Meloni, G., et al., *Probing structural transitions of nanosize silicon clusters via anion photoelectron spectroscopy at 7.9 eV*. Chem. Phys. Lett., 2004. **399**(4-6): p. 389-391.
20. Zhao, L.-Z., et al., *Theoretical Prediction of Si<sub>2</sub>-Si<sub>33</sub> Absorption Spectra*. J. Phys. Chem. A, 2017. **121**(34): p. 6388-6397.



21. Montgomery, J.A., Jr., et al., *A complete basis set model chemistry. VI. Use of density functional geometries and frequencies*. J. Chem. Phys., 1999. **110**(6): p. 2822-2827.
22. Frisch, M.J.T., G. W.; Schlegel, H. B.; Scuseria, G. E.; Robb, M. A.; Cheeseman, J. R.; Scalmani, G.; Barone, V.; Mennucci, B.; Petersson, G. A.; Nakatsuji, H.; Caricato, M.; Li, X.; Hratchian, H. P.; Izmaylov, A. F.; Bloino, J.; Zheng, G.; Sonnenberg, J. L.; Hada, M.; Ehara, M.; Toyota, K.; Fukuda, R.; Hasegawa, J.; Ishida, M.; Nakajima, T.; Honda, Y.; Kitao, O.; Nakai, H.; Vreven, T.; Montgomery, J. A., Jr.; Peralta, J. E.; Ogliaro, F.; Bearpark, M.; Heyd, J. J.; Brothers, E.; Kudin, K. N.; Staroverov, V. N.; Kobayashi, R.; Normand, J.; Raghavachari, K.; Rendell, A.; Burant, J. C.; Iyengar, S. S.; Tomasi, J.; Cossi, M.; Rega, N.; Millam, N. J.; Klene, M.; Knox, J. E.; Cross, J. B.; Bakken, V.; Adamo, C.; Jaramillo, J.; Gomperts, R.; Stratmann, R. E.; Yazyev, O.; Austin, A. J.; Cammi, R.; Pomelli, C.; Ochterski, J. W.; Martin, R. L.; Morokuma, K.; Zakrzewski, V. G.; Voth, G. A.; Salvador, P.; Dannenberg, J. J.; Dapprich, S.; Daniels, A. D.; Farkas, Ö.; Foresman, J. B.; Ortiz, J. V.; Cioslowski, J.; Fox, D. J. , in *Gaussian 09*. 2010.
23. Dennington, R.K., T.; Millam, J, *GaussView*, 5. 2009, SemiChem Inc: Shawnee Mission KS.
24. Montgomery, J.A., Jr., et al., *A complete basis set model chemistry. VII. Use of the minimum population localization method*. J. Chem. Phys., 2000. **112**(15): p. 6532-6542.
25. Berkowitz, J., et al., *Photoionization mass spectrometric studies of silylidyne, silylene, silyl, and silane (SiH<sub>n</sub> (n = 1-4))*. J. Chem. Phys., 1987. **86**(3): p. 1235-48.
26. Brown, J.M. and D. Robinson, *Observation of the vibration-rotation spectrum of the silicon monohydride radical at 5 μ by laser magnetic resonance*. Mol. Phys., 1984. **51**(4): p. 883-6.
27. Allen, W.D. and H.F. Schaefer, III, *Geometrical structures, force constants, and vibrational spectra of the silicon hydrides (SiH, SiH<sub>2</sub>, SiH<sub>3</sub>, and SiH<sub>4</sub>)*. Chem. Phys., 1986. **108**(2): p. 243-74.
28. Gong, X.G., D. Guenzburger, and E.B. Saitovitch, *Structure and dynamic properties of neutral and ionized SiH<sub>5</sub> and Si<sub>2</sub>H<sub>3</sub>*. Chem. Phys. Lett., 1997. **275**(3,4): p. 392-398.
29. Boldyrev, A.I., J. Simons, and P.v.R. Schleyer, *Ab initio study of the electronic structures of lithium containing diatomic molecules and ions*. J. Chem. Phys., 1993. **99**(11): p. 8793-504.
30. Lide, D.R., *Ionization potentials of atoms and atomic ions*. Handbook of Chem. and Phys., 1992. **10**: p. 211.
31. Boldyrev, A.A. and I.A. Svinukhova, *Na<sup>+</sup>, K<sup>+</sup>-dependent adenosine triphosphate phosphohydrolase. Two types of kinetics*. Biochim Biophys Acta, 1982. **707**(1): p. 167-70.